國 立 交 通 大 學

電子工程學系電子研究所

博 士 論 文

自組式第一型量子環與第二型量子點之

磁場光學研究

Magneto-optical Studies of Self-assembled Type-I

Quantum Rings and Type-II Quantum Dots

研 究 生 ： 林大鈞

指 導 教 授 ： 李建平

中 華 民 國 一〇〇 年 六 月

自組式第一型量子環與第二型量子點之磁場光學研究

Magneto-optical Studies of Self-assembled Type-I Quantum Rings and Type-II Quantum Dots

研 究 生：林大鈞　　　　Student：Ta-Chun Lin

指導教授：李建平　　　　Advisor：Chien-Ping Lee

國 立 交 通 大 學

電 子 工 程 學 系 電 子 研 究 所

博 士 論 文

A Dissertation

Submitted to Department of Electronics Engineering & Institute of Electronics Engineering

College of Electrical Engineering and Computer Engineering

National Chiao Tung University

in partial Fulfillment of the Requirements

for the Degree of

Doctor of Philosophy

in

Electronics Engineering

June 2010

Hsinchu, Taiwan, Republic of China

中 華 民 國 一〇〇年六月

自組式第一型量子環與第二型量子點之磁場光學研究

研究生：林大鈞　　　　　　指導教授：李建平　博士

國 立 交 通 大 學 電子工程學系電子研究所 博士班

摘要

在這篇博士論文，我們研究了自組式的第一型量子環、第二型量子點的磁場光學特性，這些量子結構使用分子束磊晶成長，並且被預期具有環狀載子波函數，能展現新穎的磁場響應，例如 Aharnov-Bohm 效應，也就是載子磁場下波函數的量子干涉現象。利用磁場光譜技術量測磁場能量偏移，我們探知侷限在這些量子結構的載子波函數空間分布，他們展現與傳統第一型量子點截然不同的物理現象，我們建立數個計算模型，模擬結果跟我們的實驗發現相符合。

在單一銦化鎵/砷化鎵量子環，雙激子呈現了一個相較於中性激子更大許多的反磁位移，這暗示了量子環有較擴張的雙激子波函數，我們發現由於量子環結構的不完美造成了兩側的位能井，激子波函數被侷限於量子環一側的位能井。然而雙激子會由於電洞間的庫倫排斥而能夠散佈整個量子

環。我們的實驗結果可以推斷，預期的量子環中性激子的量子干涉現象將被如此的波函數侷限現象所破壞。

第二型銻化鎵/砷化鎵量子點的磁場光譜量測包含法拉第組態跟沃伊特組態，當磁場施加在法拉第組態，我們觀察到標準的反磁藍移。然而，當磁場施加在沃伊特組態，量子點展現了一個反常的磁場紅移伴隨著急遽增加的螢光強度。我們發現這是因為沃伊特組態的磁場提供一個額外的垂直侷限，改善了發光複合率，因此量子點內的穩態電洞濃度下降，導致了我們觀察到的反常磁場紅移。此外，既然電子波函數分布在量子點的上下，電子波函數並非環狀，這抹煞了觀察到 Aharnov-Bohm 震盪的機會。

第二型砷化鎵/銻化鎵量子點的製作是利用晶格不匹配產生的天然張應力，利用反磁位移的實驗結果，我們分析不同尺寸量子點的載子波函數空間分布。我們發現，隨著發光能量增加(量子點尺寸減小)，反磁係數會快速上升到一個飽和值。這個不尋常的趨勢是歸因於量子點侷限的電子波函數，會隨著量子點減小而逐漸外擴到沾濕層。這個去侷限化效應會在這個材料系統內被強化，因為量子點的張應力釋放會抬升傳導帶而超過沾濕層。

因此，要觀察到光性的 Aharnov-Bohm 震盪，可行的方法是在銻化鎵/砷化鎵量子點的上下各放置一層砷化鋁鎵侷限層，可以推擠電子到量子點側邊，因此形成環狀波函數。模擬結果顯示了 Aharnov-Bohm 震盪的發生。

Magneto-optical Studies of Self-assembled Type-I Quantum Rings and Type-II Quantum Dots

Student：Ta-Chun Lin   Advisor：Dr. Chien-Ping Lee

Department of Electronics Engineering & Institute of Electronics Enineering

National Chiao Tung University

Abstract

In this dissertation, the magneto-optical properties of self-assembled type-I quantum rings and type-II quantum dots are studied. These quantum structures grown using molecular beam epitaxy are expected to possess ring-like carrier wave functions and exhibit novel magnetic responses, such as Aharnov-Bohm effect, i.e. the quantum interference of the carrier wave function in magnetic fields. The magnetic energy shifts measured by magneto-photoluminescence technique were used to probe the spatial wave function extent of the carriers confined in these quantum structures. They revealed anomalous physical phenomena compared with the conventional type-I quantum dots. Several calculation models were carried out and agree well with our experimental finding.

In single InAs/GaAs quantum rings, the biexciton showed a considerably larger diamagnetic shift than the neutral exciton, implying the more extended biexciton wave functions in the ring. We found that the structural imperfections of the quantum ring induces two potential valleys inside the ring, and the exciton wave function tends to be localized in one of the valleys. However, the biexciton wave function is able to spread over the ring due to

the hole-hole Coulomb repulsion. Our results suggest that the expected novel quantum interference of neutral excitons in quantum rings will be destroyed by such wave function localizations.

The magneto-photoluminescence measurements were performed on type-II GaSb/GaAs quantum dots in both Faraday and Voigt configurations. When the magnetic field was applied in a Faraday configuration, a typical diamagnetic blue shift was observed. However, when the field was in a Voigt configuration, the QDs exhibited an anomalous magnetic red shift together with a rapid increase of the PL intensity. We found that the magnetic field in the Voigt configuration provides an additional vertical confinement and hence increases the radiative electron-hole recombination rate. The resulting decrease of the steady-state hole concentration in the QDs gives rise to the observed anomalous magnetic red shift. Furthermore, since the electron wave function was found to be distributed above and below the QD, the electron wave function is not ring-like. This eliminates the probability of the observation of the Aharnov-Bohm oscillation.

Type-II GaAs/GaSb quantum dots were fabricated by the natural tensile strain from lattice mismatch. We analyzed the carrier wave function extent of the dots with different sizes using the diamagnetic shift results. With the increase of the energy (the reduction of the dot size), the diamagnetic coefficient was found to rises quickly to a saturated value. This unusual tendency is attributed to the gradual spreading of the electron wave function from the quantum dots to the wetting layer as the dots get smaller. This delocalization effect is enhanced in this material system due to the tensile strain relaxation within the dots, which raises the conduction band edge over that in the wetting layer.

As a result, in order to observe optical Aharnov-Bohm oscillation, two AlGaAs confinement layers are placed above and below the GaSb/GaAs quantum dots. The electrons are therefore pushed to surround the dots with ring-like wave functions. The simulation results reveal the occurrence of the Aharnov-Bohm oscillation.

致謝

　　在我的求學生涯中，最感謝的就是李建平老師，在我最初還在摸索做研究的方法的時候，不斷地包容我緩慢的實驗進展，老師很尊重我的步調，讓我很自由的做自己喜歡的研究，不但提供充足的研究資源，也常常對我的研究提出一針見血的建議，最高興最後我也順利有很好的研究成果，沒有辜負老師。其次是林聖迪老師，總是在我迷惘的時候給我方向跟鼓勵，遇到瓶頸的時候，跟老師的討論總是給我許多收穫。孫允武老師、羅明城學長、凌鴻緒學長、林志昌學長、李良筬學姊，我基礎的實驗知識都來自於你們，感謝你們的栽培跟教導讓我有能力獨當一面，並且寬容我偶爾犯下的實驗上的過錯。感謝霍斯科老師、張文豪老師，給我學業上的幫助，尤其是張文豪老師的幫助，讓我順利發表我的首篇國際期刊，之後的研究進展才開始抓到訣竅。此外，感謝同學跟學弟們，潘建宏、蘇聖凱、鄭旭傑、宋育泰、林岳民、林建宏、傅英哲、巫朝陽、李依珊，族繁不及備載，在實驗上熱情相助，在學業上互相討論，跟你們相處玩樂冒險的日子很愉快。很高興我的青春能用在這樣一個風氣自由又溫馨的實驗室。最後，我必要感謝，我的家人，爺爺、奶奶、爸爸、媽媽、弟弟、阿姨，謝謝你們在人生的旅途中陪伴著我走過，我的人格來自你們的塑造，謝謝你們長久以來的悉心照顧，尤其是媽媽，我大學時您一肩扛起家計，之後也沒有給我經濟上奉養的壓力，讓我可以順利完成學業，而且在我失戀的時候總是第一個安慰我，在我低潮的時候總是能夠開導我，謝謝老媽。

CONTENTS

Chapter 3: Impacts of Structural Asymmetry on the Magnetic Response of Single Self-Assembled In(Ga)As Quantum Rings

Chapter 4: Anomalous Optical Magnetic Red Shift of Self-Assembled GaSb/GaAs Quantum Dots

Chapter 5: Delocalization of Tensily-Strained GaAs Quantum Dots in GaSb Matrix

Chapter 6: Aharonov-Bohm Oscillation of GaSb/GaAs QDs with Vertical Confinement

Chapter 7: Conclusions and Future Work

ix

TABLE CAPTIONS

CHAPTER 3:

CHAPTER 5:

FIGURE CAPTIONS

CHAPTER 3

CHAPTER 4

blue arrows indicate the direction of the magnetic force acted on electrons. 60

CHAPTER 5

CHAPTER 6

Chapter 1

Introduction

III-V semiconductor heterostructures have been widely used in the field of the optoelectronic devices and the high-speed devices due to the direct band gap structure and the small electron effective mass. Practical device applications includes the light emitting diodes (LEDs), laser diodes, photodetectors, heterojunction bipolar transistor (HBT), and high electron mobility transistor (HEMT) [1, 2]. In the past decade, owing to the mature growth techniques, the self-assembled zero-dimensional (0-D) quantum structures grown by Stranski-Krastanov (S-K) mode were well developed for the application of the optoelectronics, such as quantum dot (QD) lasers, QD infrared photodiodes (QDIP), and QD memory devices. Since the carriers confined in the 0-D quantum structures manifest the atom-like structures, they have been proven to be well suited for photonics-based quantum information processing, such as single photon emitters [3, 4] and quantum logic gates [5]. Besides, 0-D quantum structures provide the opportunity to exhibit several novel physical phenomena. For example, type-I quantum rings (QRs) and type-II QDs in magnetic fields are expected to exhibit the experimental evidence of Aharonov-Bohm effect due to the quantum interference [6-9]. The electronic structures and the magnetic responses of these novel 0-D quantum structures can be investigated using magneto-photoluminescence measurements, which are used to probe the exciton energy, the spatial excitonic wave function extent, the excitonic magnetic quantum number, and the excitonic spin quantum number. In this dissertation, the magnetic-optical properties of the self-assembled type-I InAs/GaAs single QRs, type-II GaSb/GaAs QDs, and type-II GaAs/GaSb QDs were studied. Several uncommon magnetic responses were observed. We built up several theoretical calculation models to explain these unusual experimental findings.

1.1 Self-assembled Zero-dimensional Quantum Structures

In the late 1980s, the fabrication of the 0-D quantum structures is via lithography and etching process [10] or the etched strained layer on the surface [11] on the quantum well (QW) structure. However, the interface defects induced by the etching process significantly degrade the quantum efficiency of the small nanostructures and eliminate the possibility of the electronic and optoelectronic device applications. In 1990s, the Stranski-Krastanov (S-K) mode grown QDs are found to be defect-free with great optical properties. They are formed spontaneously due to the natural compressive or tensile strain arising from the lattice mismatch between the dot material and the substrate material. [12]. Therefore, since the early 1990s, much effort has been put into the study of the QD growth and characterization, such as In(Ga)As/GaAs, InGaP/InP, and GaSb/GaAs QD system.

In the 0-D quantum structures, the carriers are constrained in all directions, and the density of states is hence δ-function like as shown in Fig. 1.1. The δ-function like density of states is the signature of the 0-D system. The electronic structure with discrete energy states is similar to that of an atom. The discrete states are expected to bring the better device performance, such as the reduction of the threshold current of laser devices. Besides, the temperature stability of the laser, i.e. the characteristic temperature T_0, can be improved as the energy difference between different states is larger than the thermal fluctuation (26 meV at room temperature). In order to achieve the 3-D quantization, the confinement length (dot size) for each direction should be smaller than the bulk exciton radius (~10 nm for GaAs and ~30 nm for InAs). In this situation, the quantum confinement effect, rather than the Coulomb-induced electron-hole correlations, becomes dominant. The quantum confinement decreases the exciton radius (electron-hole spatial separation) and therefore enhances the oscillator strength as well as the optical properties.
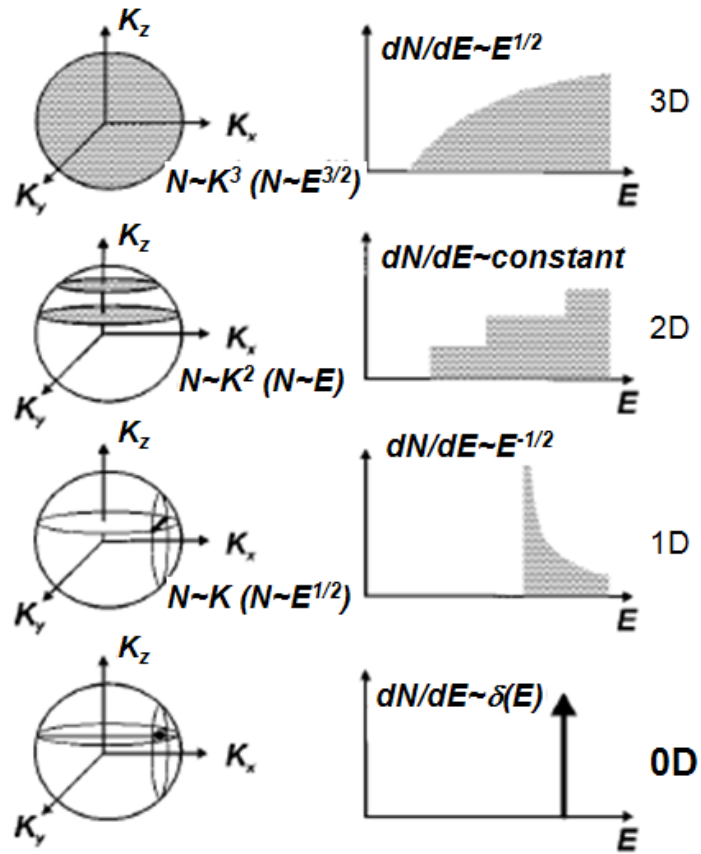
FIG. 1.1. Density of states for carriers in quantum structures with different dimensionalities [1.14].

The other advantage of the quantum structures is the flexibility. Via controlling the size, shape, and material composition of these self-assembled QDs, their electronic and optical properties can be well designed for various optoelectronic applications. In recent years, a growth process involving partially capping and in-situ annealing has succeeded in transforming InAs QDs into QRs [13]. The topologies of the QDs and the QRs are shown in Fig 1.2. The QR structure is expected to show unique magnetic response, i.e., the well-known Aharonov-Bohm effect, due to the quantum interference of the carrier's wave function in the ring-shaped geometry [14, 15].
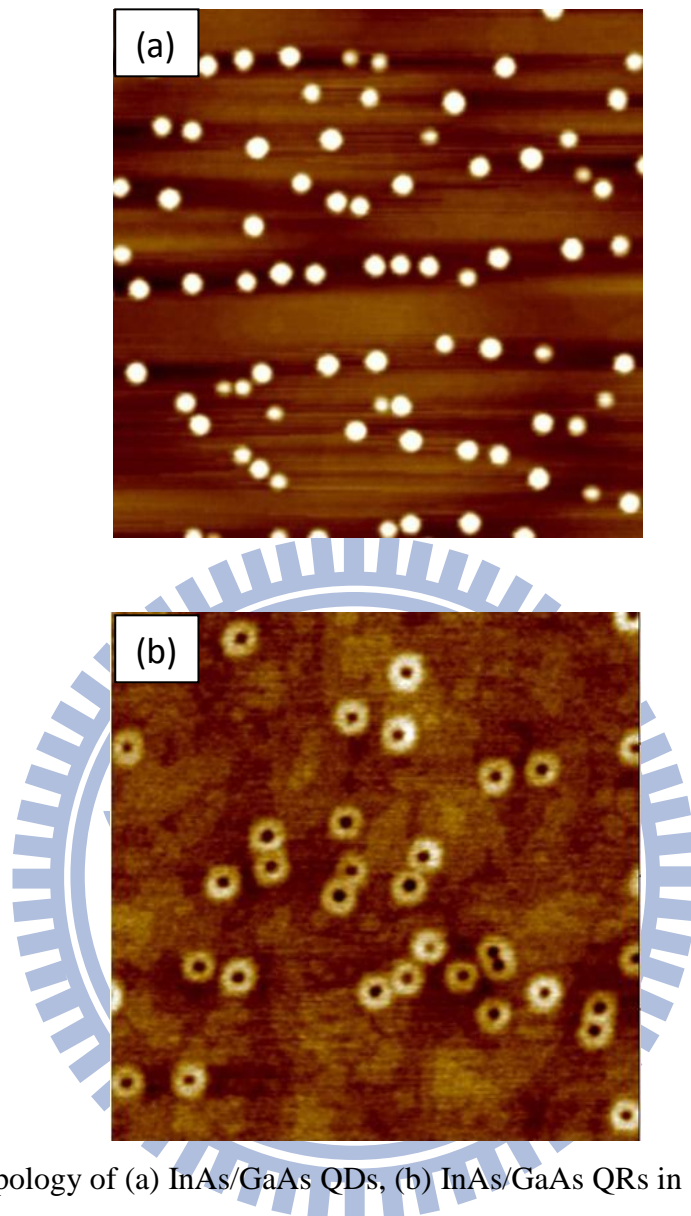
FIG. 1.2. The topology of (a) InAs/GaAs QDs, (b) InAs/GaAs QRs in 1 µm square image area
observed by atomic force microscope technique.

1.2 Heterostructures and Type-II Quantum Dots

A heterostructure contains two different semiconductor materials. Ideally, the band alignment near the heterojunction is only determined by the bandgap energy, the Fermi level, and the electron affinity difference between the two materials. Three kinds of heterojunctions are type-I, type-II and type-III as shown in Fig. 1.3. However, the difference of the lattice constant, i.e. the lattice mismatch, leads to the position-dependent strain distribution, and the unexpected material segregation and the atomic intermixing near the interface causes the composition variation. Both effects strongly influence the real band structure [16, 17].
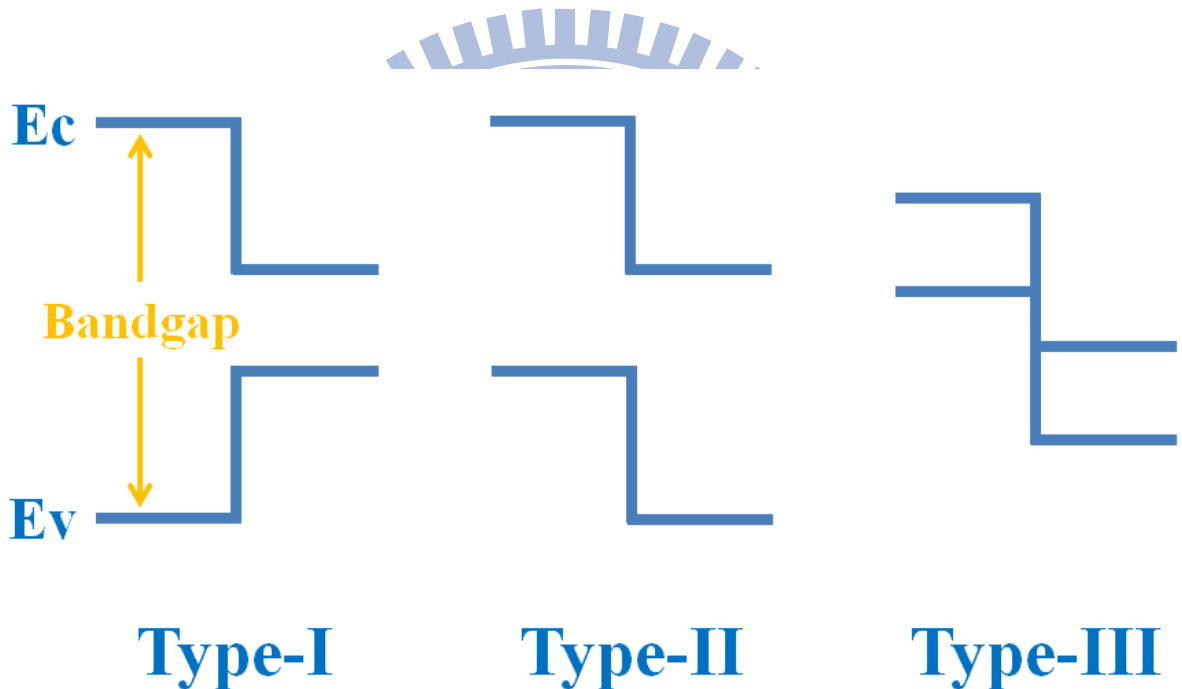
FIG. 1.3. The schematic drawing of the band alignment of the type-I, type-II and type-III heterojunction.

The 0-D quantum structures discussed in this dissertation includes type-I InAs/GaAs QDs and QRs, type-II GaSb/GaAs QDs, and type-II GaAs/GaSb QDs. Their band structures are drawn in Figure 1.4. For InAs/GaAs QDs, electrons and holes are confined in the dots and contribute strong oscillator strength which is proportional to the wave function overlap of the electron-hole pair. For type-II GaSb/GaAs (GaAs/GaSb) QDs, holes (electrons) are strongly

localized in the dots, but electrons (holes) are confined to the matrix material next to the dot due to the Coulomb interaction. The oscillator strength of the electron-hole pairs confined in type-II structures is therefore much weaker than that in type-I structures due to the spatial separation between the electrons and the holes.

Recently, type-II self-assembled QDs have attracted considerable interest for the application of carrier storage [18], the spin storage device [19], and the wavelength-tunable LED [20] owing to the spatial separation between the electrons and the holes. Besides, they are also used for the exhibition of optical Aharonov-Bohm effect in magnetic fields [7, 8, 21] due to the ring-shaped wave function of the carrier which surrounds the dot. Since type-I QR and type-II QD are expected to exhibit the experimental evidence of the novel optical Aharonov-Bohm effect, we studied the optical magnetic properties of these quantum structures.
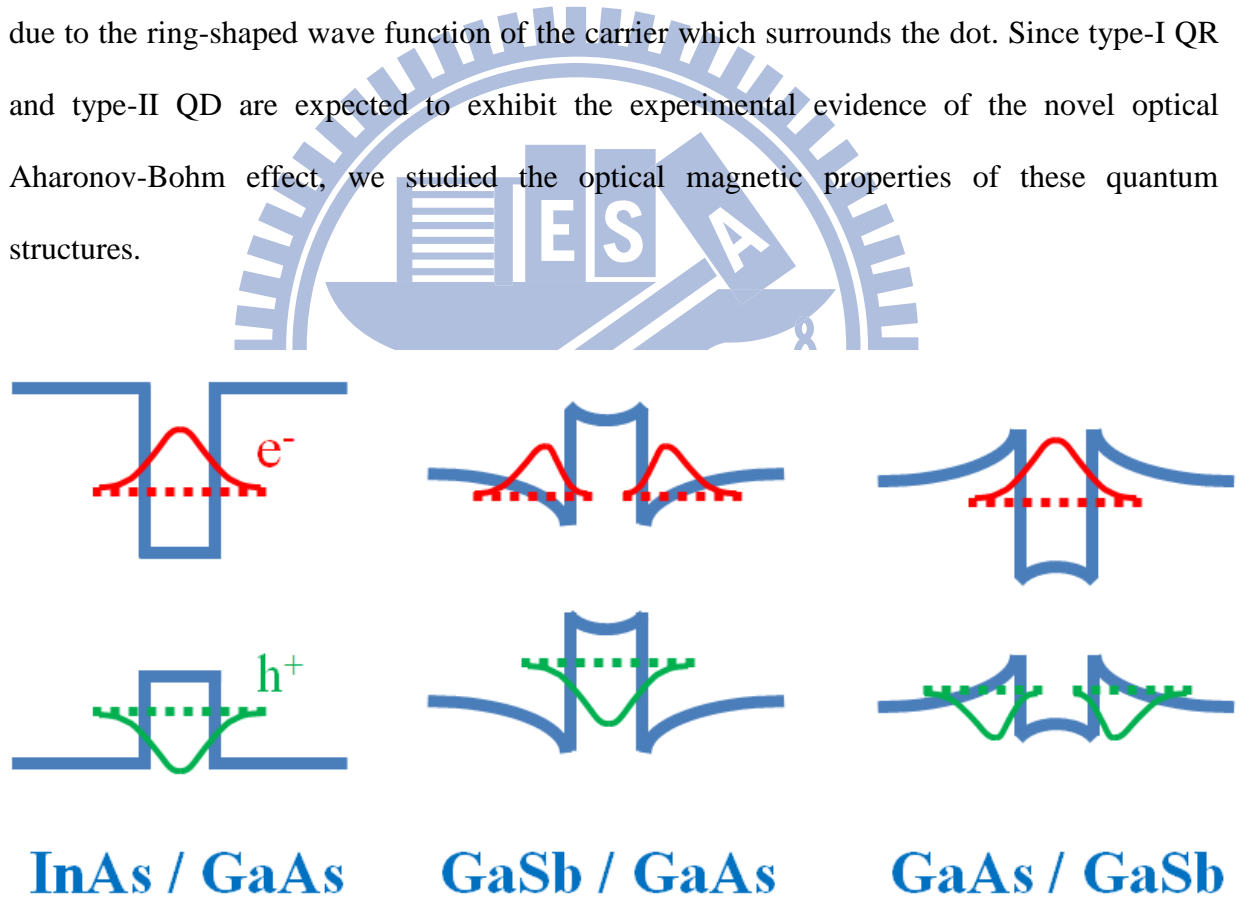
FIG. 1.4. The band alignment of InAs in GaAs matrix, GaSb in GaAs, and GaAs in GaSb.

1.3 Magnetic responses of Semiconductor Quantum Structures

1.3-1 Hamiltonian in magnetic fields

The Hamilton of a single electron confined in a quantum structure in the presence of an uniform magnetic field $\vec{B}$ applied in z-direction is given by

$$H = \frac{1}{2m}\left[\hat{p} - e\vec{A}(\vec{r})\right]^2 + V(\vec{r}) \tag{1.1}$$

, where $V(\vec{r})$ is the confining potential from band discontinuity, $\vec{A}$ is the magnetic vector potential, m is the electron effective mass. The magnetic field is given by $\vec{B} = \nabla \times \vec{A}(\vec{r})$. By adopting the symmetric gauge, i.e. $\vec{A} = \frac{1}{2}B(-y, x, 0)$, the Hamilton can be expanded as $H = H_0 + H_Z + H_D$, and

$$H_0 = \frac{\hat{p}^2}{2m} + V(\vec{r}) \tag{1.2}$$

$$H_Z = -\frac{e\hbar B}{2m}\frac{i\partial}{\partial\varphi} = -\frac{e}{2m}\vec{L} \cdot \vec{B} \tag{1.3}$$

$$H_D = \frac{e^2 B^2}{8m}\hat{\rho}^2 \tag{1.4}$$

where $\vec{L}$ is the operator of the orbital angular momentum, and $\hat{\rho}$ is the operator of the vector projection of $\vec{r}$ onto the plane perpendicular to $\vec{B}$. H_0 is the Hamilton at a zero magnetic field. H_Z is the orbital Zeeman effect term. For a azimuthally symmetric quantum structure, such as a hydrogen atom, an ideal QD, and an ideal QRs, the electron wave function $\psi_{n,\ell}$ has a perfect angular quantum number ℓ. The energy shift due to this term is

$$\Delta E_{ZO} = -\frac{e\hbar}{2m}\ell B. \tag{1.5}$$

For the ground state with $\ell = 0$, this term is neglected. For the excited states with $\ell \neq 0$, this leads to the orbital Zeeman splitting.

H_D is the diamagnetic term. In classic physics, the change of the external magnetic flux of a circuit induces an opposing magnetic field. This is called Lenz's law. The opposing magnetic moment $\vec{m}$ is proportional to the area of the circuit and the change of the external $\vec{B}$. Therefore, the magnetic potential energy $U = -\vec{m} \cdot \vec{B}$ is proportional to the area of wave

function and show a quadratic dependence on the external $\vec{B}$. Since the direction of $\vec{m}$ and $\vec{B}$ is opposite, the contribution of U must be positive, which leads to the diamagnetic effect in most semiconductors.

For a weak magnetic field compared with the Coulomb interaction, H_D is considered as a small perturbation of the system, and the diamagnetic shift in the exciton energy is given by

$$\Delta E_D = \frac{e^2 B^2 \langle \rho^2 \rangle}{8m} \tag{1.6}$$

Therefore, the diamagnetic shift can be used to probe the wave function spatial extent in the plane normal to the magnetic field. When the magnetic field gets strong enough, the cyclotron energy dominates over the Coulomb energy and the confining energy from the band discontinuity. The electron wave function is strongly altered by the magnetic field, and the energy shift turns to be linearly dependent on the field. The linear dependence is well-known as Landau quantization and is described as

$$\frac{dE}{dB} = \frac{e\hbar}{2m} \tag{1.7}$$

In addition, spin angular momentum also causes an energy splitting in magnetic fields, i.e. spin Zeeman splitting, even for the ground-state electrons with orbital magnetic quantum number of 0. With assumption of weak spin orbital coupling, another term H_{ZS} is added to the Hamilton:

$$H_{ZS} = -\mathrm{g}\frac{e}{2m_0}\vec{S}\cdot\vec{B} \tag{1.8}$$

, where $\vec{S}$ is the operator of the spin angular momentum, g is the g factor. The energy shift due to this term is

$$\Delta E_{ZS} = -\mathrm{g}\frac{e\hbar}{2m_0}sB \tag{1.9}$$

Since m_0 is much larger than the effective mass in semiconductors, the spin Zeeman splitting is much smaller than the orbital one if $\ell \neq 0$. For InAs/GaAs quantum dots, the g factor is about 2, and the spin Zeeman splitting is only around 0.8 meV at 14 Tesla. Since the

full width half maximum (FWHM) of the PL emission from QD ensemble is usually larger than 20 meV, the spin Zeeman splitting is usually smeared out. However, this splitting is very essential for single dot spectroscopy, where the QD PL lines have the FWHM of 50 μeV, which is limited by the system resolution.

1.3-2 Ideal magnetic responses of QDs and QRs

Now, we turn to the energy spectrum of the QDs and the QRs in varied magnetic fields. Since the spin Zeeman term of the Hamilton is much smaller and is not able to reflect the geometry and the dimension of the quantum structures, it is neglected in these calculations. Considering a QD with a simplified 2-D parabolic confining potential $V(x, y) = \frac{1}{2} m_e \omega_0^2 (x^2 + y^2)$ as shown in Fig 1.5(a) and 1.5(b), the eigen energy of a single confined electron subject to this potential is given by

$$E_{n,\ell} = \hbar \omega_h (2n + |\ell| + 1) + \frac{1}{2} \ell \hbar \omega_c \tag{1.10}$$

where $\omega_c = \frac{eB}{m_e}$ is the cyclotron frequency and $\omega_h = \sqrt{\omega_0^2 + \left(\frac{\omega_c}{2}\right)^2}$ is the hybridized frequency. The energy spectrum of the electron confined in a QD is plotted in Fig. 1.5(c), and this theoretical spectrum was observed experimentally using the InGaAs/GaAs QD ensemble induced by strain field [22]. In a zero magnetic field, the ground state has no degeneracy, the first excited state has two degenerate states, the second excited state has three degenerate states, and so on. The ground state (0,0) does not cross any other energy states in any magnetic field.

(a) $\vec{B}$

(b) V

x

(c)

Energy

(0,2)

(1,0)

(0,-2)

(0,1)

(0,-1)

(0,0)

(0,-5)
(0,-4)
(0,-3)
(0,-2)
(0,-1)

(0,0)
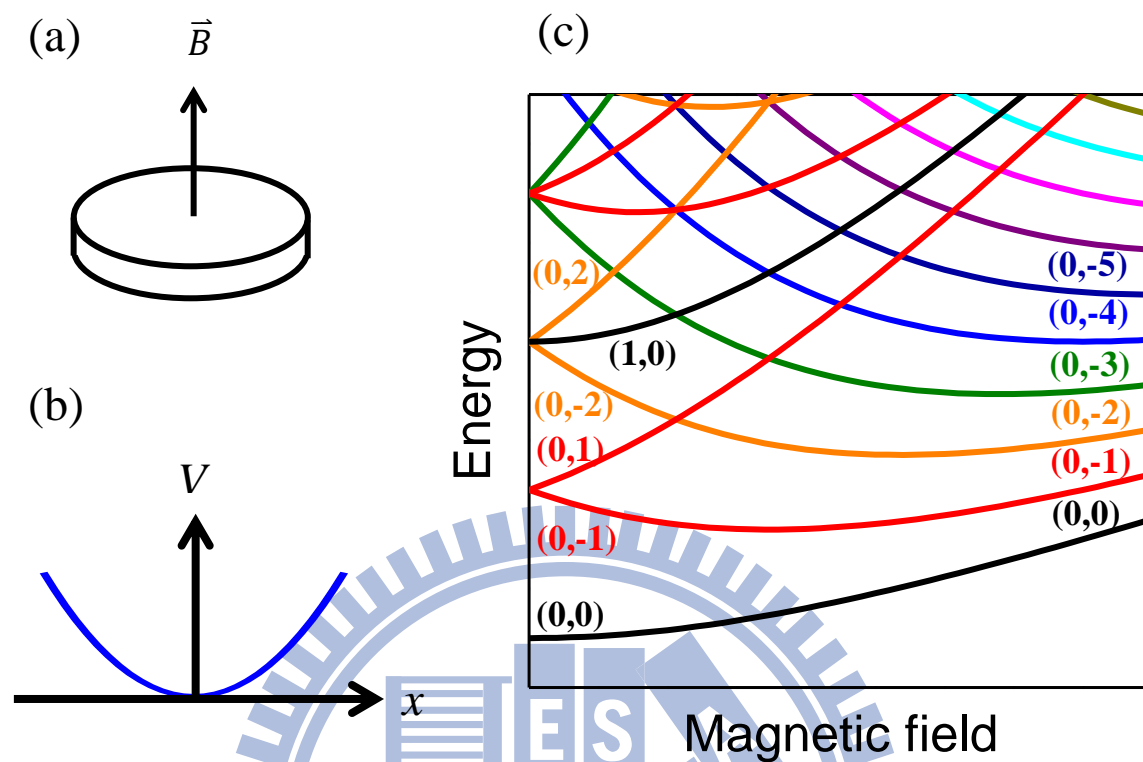
Magnetic field

FIG. 1.5. (a) A QD with magnetic field applied along the growth direction. (b) The parabolic confining potential of the QD. (c) The energy spectra of the electron confined in the QD with a 2-D parabolic confining potential. The quantum numbers of (n, ℓ) is marked for the energy states.

For an ideal ring with the radius of R, infinitely narrow width and height, and infinitely large potential height as shown in Fig. 1.6(a), the electron are only allowed to move in the direction $\hat{\theta}$. Based on the fact of the azimuthal symmetry, the electron wave function can be expressed as $\psi_\ell = A\, e^{i\ell\theta}$, and the eigen energy is

$$E_\ell = \frac{\hbar}{2m_e R^2}\left(\ell - \frac{\Phi}{\Phi_0}\right)^2 \tag{1.11}$$

where $\Phi = 2\pi R^2$ is the magnetic flux and $\Phi_0 = h/e$ is the flux quantum. The energy spectrum of the electron confined in an ideal ring is plotted in Fig. 1.6(b). In zero magnetic field, excepting the ground state, all excited states has two degenerate states. Most importantly, the angular quantum number of the ground state increases by one at the specific magnetic fields. This is because the wave function of a charged particle acquire a phase difference $\Delta\varphi$ determined by the magnetic flux Φ through the area, which is given by

$$\Delta\varphi = \frac{e\Phi}{\hbar} \tag{1.12}$$

When the phase difference changes from 0 to 2π, the ground state energy rises first and then gets back to the lowest value of zero due to phase coherence, and the ground state angular momentum also changes from 0 to 1. As a result, the ground state reveals an energy oscillation with the magnetic field. This phenomenon is called Aharonov-Bohm oscillation. This oscillation presents the experimental evidence of quantum interference.

In fact, the realistic QR has a width about R as plotted in Fig. 1.6(c). Hence, the electron energy spectrum is modified and shown in Fig. 1.6(d) [14]. The energy oscillation becomes less pronounced. Therefore, in order to clearly observe this Aharonov-Bohm oscillation, the FWHM of the PL emission must be smaller than 1 meV. In other words, the magneto-PL measurements performed on single QRs or single type-II QDs is necessary.
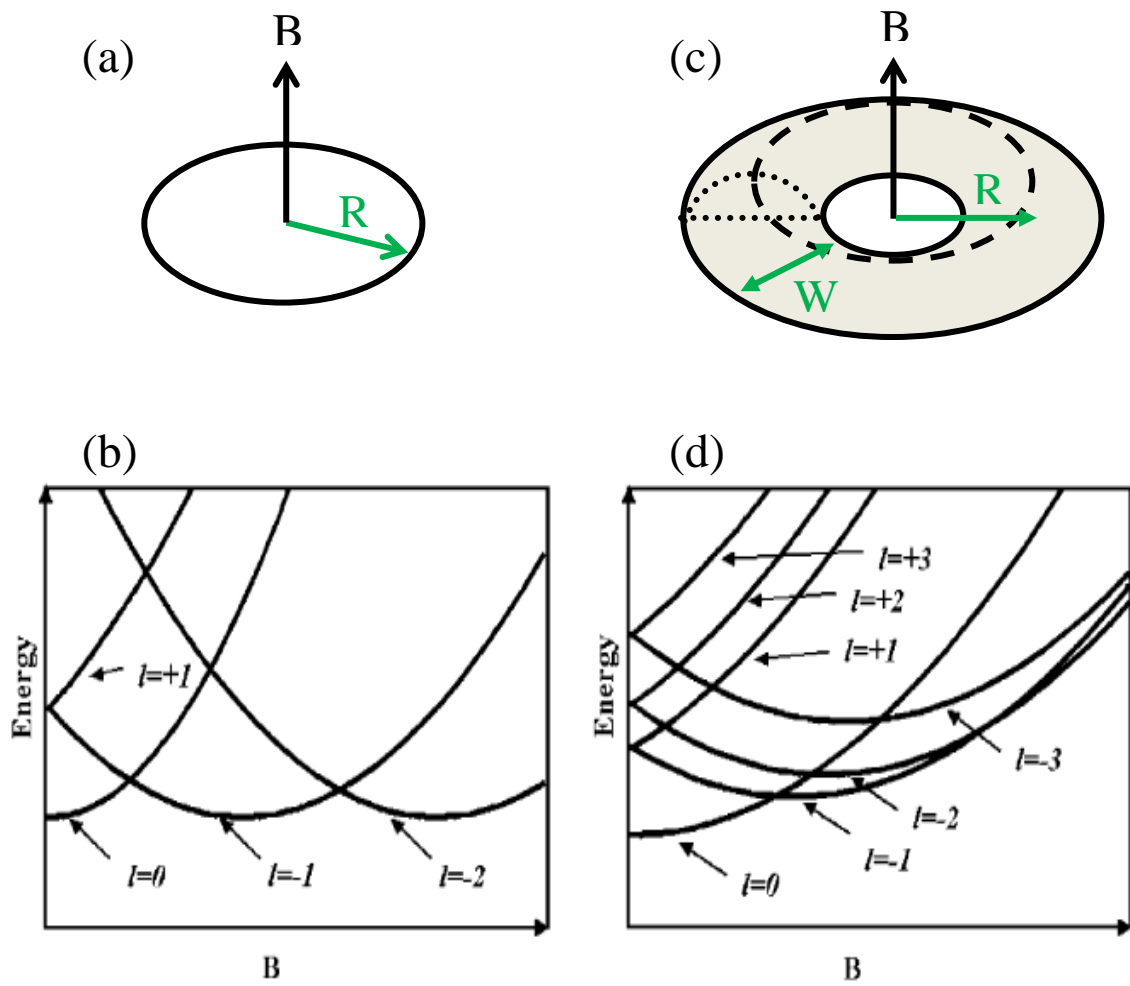
FIG. 1.6. (a) A ideal ring with the radius of R and infinitely narrow width and height. (b) The

energy spectra of the electron confined in the ideal ring. (c) A QR with the rim radius of R. (d)

The energy spectra of the electron confined in the QR.

1.3-3 Choices of gauge

In the calculation of the ground-state carrier wave functions, the orbital Zeeman term of the Hamilton is usually neglected since their angular momentum should be zero. Therefore, the magnetic shift of the ground state energy is only determined by the diamagnetic shift $\Delta E_D = \frac{e^2 B^2 \langle \rho^2 \rangle}{8m}$. However, since ρ is the distance between the carrier and the origin, the definition of the origin of the gauge play an important role on the results. As a result, we choose the center of the carrier wave function, i.e. the expected value of the position of the carrier, to be the origin. As shown in Fig. 1.7, for a QD, the origin is defined as the center of the dot. For an asymmetric QR, the origin is moved to the higher side of the ring. Note that the ground-state wave function in an asymmetric QR is not azimuthally symmetric. Therefore, the orbital Zeeman term $H_Z = -\frac{e\hbar B}{2m} \frac{i\partial}{\partial\varphi}$ must be taken into consideration.

In fact, when the orbital Zeeman term is considered, the results should become independent on the choices of the gauge. This is because the change of the diamagnetic term is cancelled out by the change of orbital Zeeman term. We compare the calculation results of the QD for different gauges as depicted in Fig. 1.8. In the figure, d represents the distance between the origin of the gauge and the center of the dot. The magnetic shift gets larger as d increases. This is because the calculation in this study is based on the finite element method. The error of the calculation result gets larger when d increases. Besides, when the orbital Zeeman term is not considered, the calculation result is plotted as the orange line in Fig. 1.8(b). The error is found to be considerably larger.
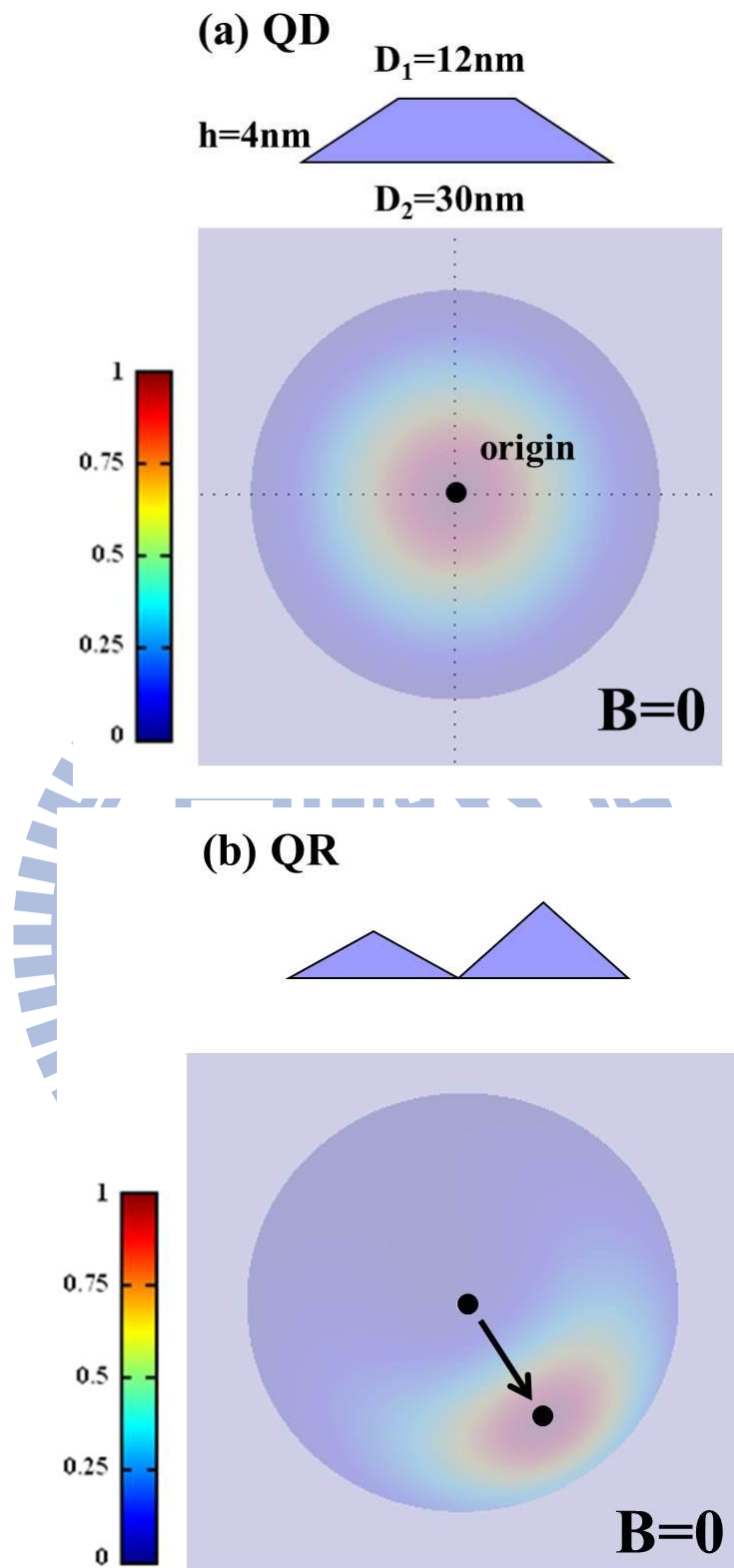
FIG. 1.7. (a) The electron wave function at a zero magnetic field in a QD. (d) The electron wave function at a zero magnetic field in an asymmetric QR.
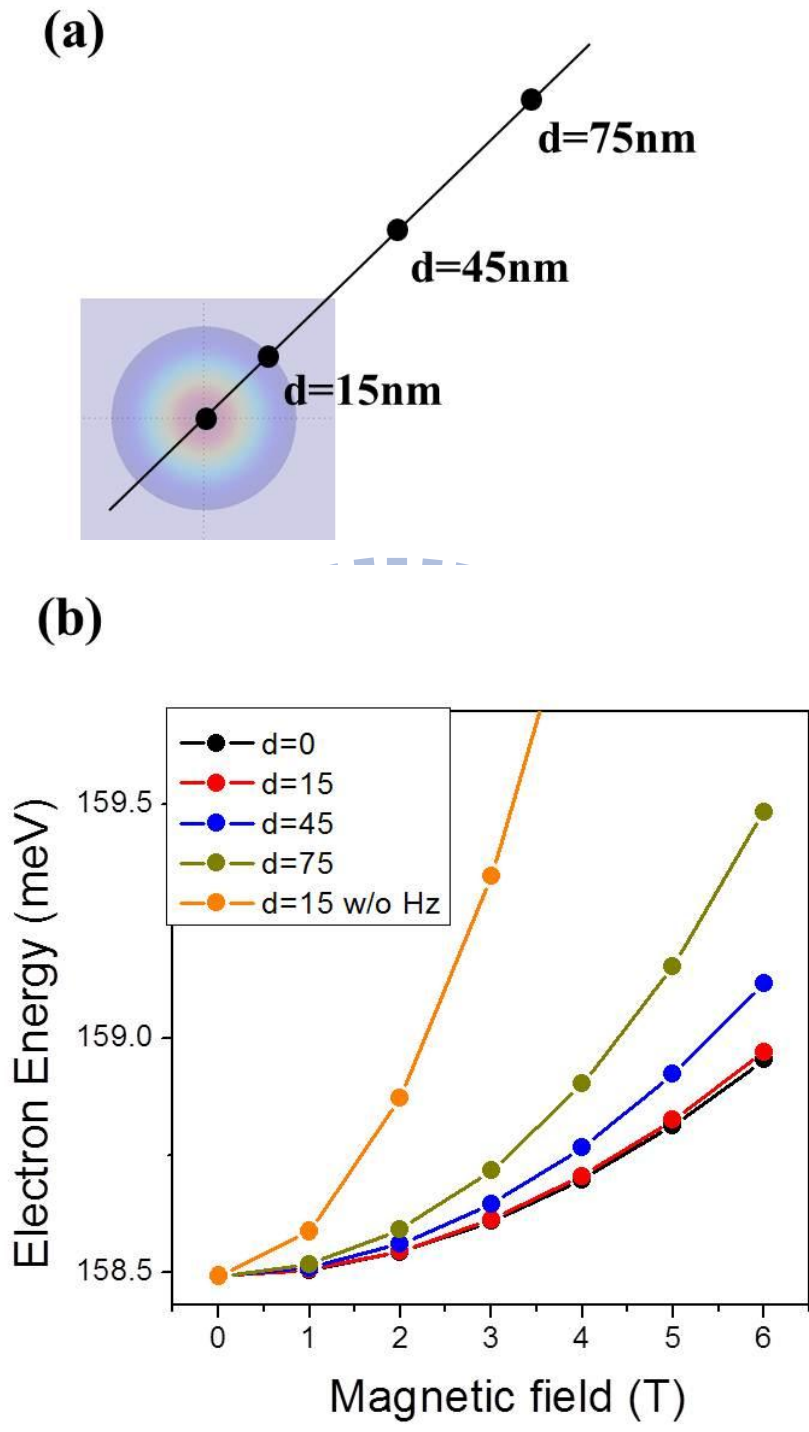
FIG. 1.8. (a) The defined origins of the gauge in the calculation. (b) The calculated electron energy in a QD for different gauges.

1.4 Organization of This Dissertation

In this dissertation, we study the magneto-optical properties of several quantum structures with ring-like carrier wave functions, such as the InAs/GaAs QRs, the GaSb/GaAs QDs, and the GaAs/GaSb QDs. The experimental techniques used are described in chapter 2, including MBE growth, material characterization methods, and magneto-photoluminescence measurement techniques.

In chapter 3, the diamagnetic response of the ground-state neutral excitons and biexcitons confined in single self-assembled QRs is investigated. The diamagnetic coefficient of the biexcitons is considerably larger than that of the excitons. We found that the inherent structural asymmetry and imperfection of the QR play a crucial role in the distribution of X and XX wave function. Our results suggest that the phase coherence of neutral excitons, i.e. the Aharonov-Bohm effect, in QRs is smeared out due to the structural asymmetry.

In chapter 4, we report the magneto-photoluminescence measurement results on type-II self-assembled GaSb/GaAs quantum dots with the magnetic field applied in Faraday and Voigt configurations. When the magnetic field was in the Voigt configuration, an unusual red shift in the emission peak accompanied with a rapid increase of the PL intensity was observed. This anomalous red shift is attributed to the reduction of the vertical e-h separation and the resulting increase of the radiative e-h recombination rate in the magnetic fields applied in the Voigt configuration.

In chapter 5, we study the magneto-optical properties of GaAs QDs in GaSb matrix. As the size of the QDs is changed, an unusual correlation was found between the diamagnetic coefficient and the emission energy. We attributed this phenomenon to the weak localization of electrons within the small-sized QDs in the tensily-strained system.

In chapter 6, we model the magnetic response of the GaSb/GaAs QDs with AlGaAs vertical confinement layers. Aharonov-Bohm oscillation is clearly observed in the calculation.

Finally, conclusions and a plan for future work are given in chapter 7.

Chapter 2

Experimental Techniques

In this chapter, the used experimental techniques in this study are briefly described. The samples studied in this dissertation were all grown by the molecular beam epitaxy (MBE) system. The structural properties of the semiconductor nanoscale objects in the samples were characterized by the atomic force microscopy (AFM) or transmission electron microscopy (TEM). The optical properties, the magnetic response, and the electronic structures were investigated by the photoluminescence (PL), magneto-PL, and micro-PL (μ-PL) techniques.

2.1 Molecular Beam Epitaxy

The molecular beam epitaxy (MBE) is a physical deposition process in an ultra-high vacuum (UHV) environment. The reactive molecules are able to directly strike the substrate without any scattering because the mean free path of the molecules is longer than the distance between the sources and the substrate. The deposition amount is therefore well controlled, and the layer structures with precise thickness and abrupt interfaces can be achieved. The UHV environment also minimizes the amount of the impurity and hence improves the epitaxy quality. As a consequence, the MBE growth offers precise deposition amount and excellent optical quality.

2.1-1 MBE system

The MBE system in our lab consists of two individual growth units: Varian and Veeco Gen II (solid-source based) system. Each system comprises three chambers: entry/exit chamber, buffer chamber, and growth chamber as drawn in Fig 2.1. Two gate valves are used to isolate these three chambers. In order to maintain UHV, all the pumping machines are oil

free to reduce the contamination. A turbo-molecular pump cascaded by a scroll pump is used for rough pumping. Besides, a cryo-pump, an ion-pump, and a titanium-sublimation pump (TSP) are used in the growth chamber, an ion-pump and a TSP are used in the buffer chamber, and a cryo-pump is used in the entry/exit chamber for UHV pumping. In addition, a liquid-nitrogen-cooled cryo-panel is installed within the growth chamber to improve the vacuum level during growth and eliminate the thermal cross-talk between different cells.
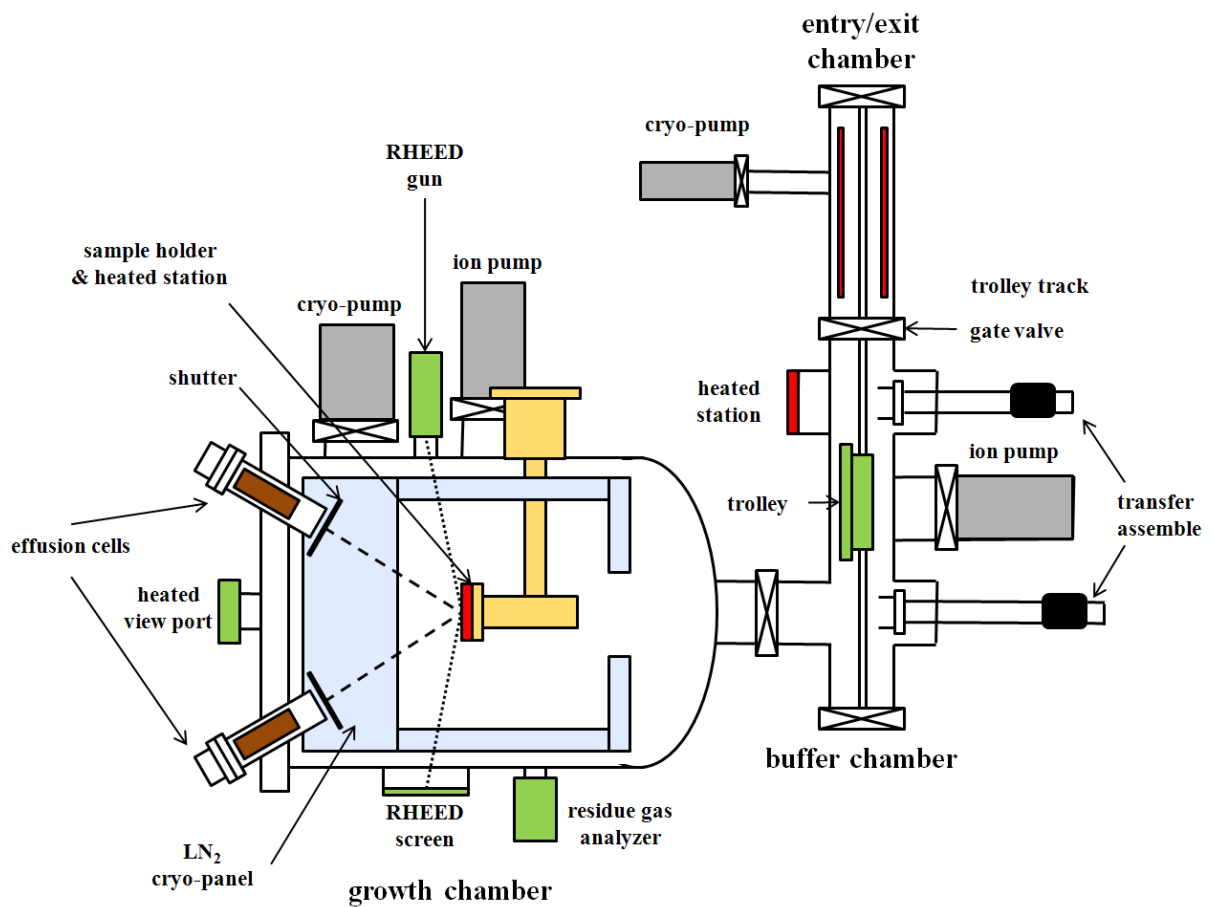
FIG. 2.1. Drawing of the Veeco Gen II MBE system in our lab.

The Varian Gen-II system is named as Lm-MBE and is used for arsenide-based III-V materials with high epitaxy quality. Eight effusion cells are equipped on the Lm growth chamber. Two gallium (Ga) cells, one indium (In) cell and one aluminum (Al) cell are used for group III sources. One arsenic (As) valved cracker cell and one arsenic Kunsden cell are used for group V sources. Besides, one silicon (Si) cell and one beryllium (Be) cell are used for n-type doping and p-type doping, respectively. The Veeco Gen-II system is named as Rn-MBE and provides the growth of antimony related III-V materials. In addition to the sources in Lm-MBE, one antimony (Sb) valve cracker cell for another group V source and one tellurium (Te) cell for n-type doping in GaSb material are added in Rn-MBE.

2.1-2 In-situ analysis instruments

Two analysis instruments, the residue gas analyzer (RGA) and the reflection high-energy electron diffraction (RHEED) monitor, are also equipped in each growth chamber. The RGA is used to analyze the residue gas in the chamber for understanding the cleanness in the chamber. The RGA also serves as a sensitive leakage detector by helium (He) gas leakage detecting. The RHEED allows us to in-situ monitor the sample surface condition during the epitaxy. The high energy electron beam with a very small angle strikes the surface of the sample, and the reflective beam builds a reconstruction structure on the screen. The reconstruction structure represents the diffraction patterns and indicates the surface morphology. For example, the clear streaky RHEED pattern indicates a clean oxide free surface with excellent flatness as depicted in Fig 2.2 (a), and a spotty RHEED pattern represents a 3-dimensional structure is formed, such as the quantum dots (QDs) as shown in Fig. 2.2(b).
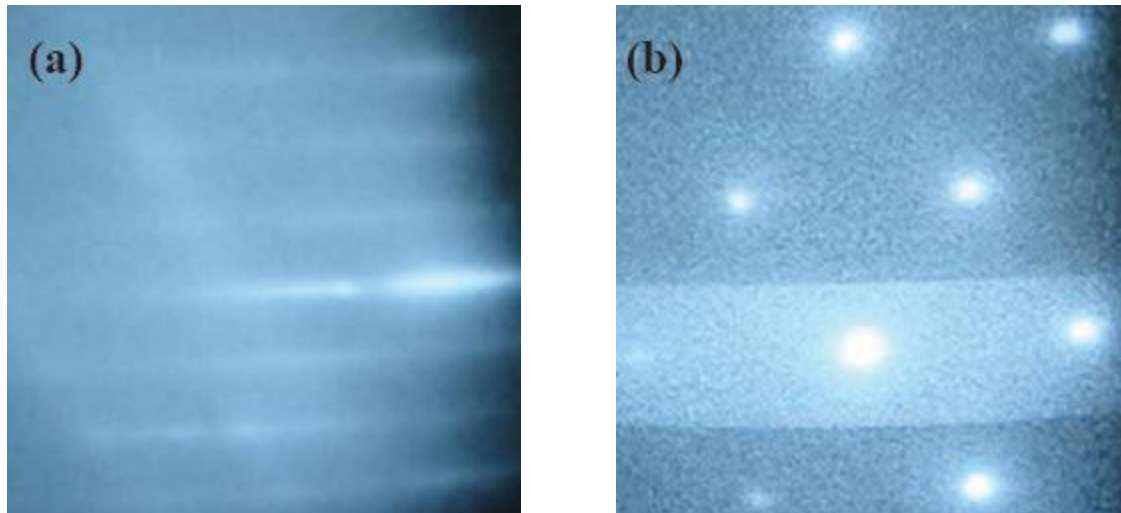
FIG. 2.2. RHEED patterns of (a) GaAs epi-layer and (b) GaSb QDs on GaAs substrate.

2.1-3 Growth condition

The structural properties and the crystal quality of the epitaxial material are determined by the growth temperature, the growth rate, and the V/III BEP ratio. The V/III BEP ratio is the beam equivalent flux pressure ratio of the group V beam flux to the group III one. Generally, the suitable growth temperature is around 580 ℃ for GaAs, 500 ℃ for InAs, and 500 ℃ for GaSb. The typical V/III ratio for Stranski-Krastanov mode quantum dot formation is 10~20 for III-arsenic and 1~5 for III-antimonide. To ensure the epitaxial quality and flatness of the epi-layers, the suitable growth parameters are necessary. Besides, for 3-D quantum structures, such as the InAs and GaSb self-assembled quantum dots (SAQDs), the size, the composition, the strain distribution, and the sheet density of the QDs are highly dependent on these parameters. In general, high growth temperature, low growth rate, and low V/III BEP ratio enhance the mobility of deposited atoms on the sample surface, which increases the QD size and reduces the QD density. The growth of the QDs with ultra-low dot density of $< 1\times10^{8}$ cm^{-2} for single dot spectroscopy can be achieved on this growth condition.

2.2 Structure Characterization

The geometry of the nanoscale objects is able to be analyzed by the atomic force microscopy (AFM) and transmission electron microscopy (TEM) techniques. AFM is a fast and non-destructive method for surface structure characterization due to the minimal sample preparation. TEM is a powerful tool to observe the quantum structures embedded inside the sample with extremely high resolution. Note that the dimension of the embedded structures is somewhat different from that of the surface structures due to the strain from the capping layer.

2.2-1 Atomic force microscope

The AFM system mainly consists of a cantilever with a sharp tip on the end. The cantilever is vibrated by a piezoelectric ceramic with the frequency close to its resonant frequency. The van der Waals force between the AFM tip and the sample surface will dump the oscillation of the cantilever. Since this force is sensitive to the distance between the AFM tip and the sample surface, the surface topography can be detected by scanning the sample and recording the oscillation amplitude.

The AFM is performed for QDs (and QRs) by a Veeco D3100 commercial system in tapping mode in our study. The QDs with the same growth condition as the embedded QDs is grown on the sample surface for AFM measurement. The sheet density, geometry, size, and the uniformity of the surface QDs can be obtained by the AFM. However, the size of the surface QDs is expected to be different from the embedded QDs. For the common compressively strained QD system, InAs QDs in GaAs matrix, the embedded QDs are expected to be smaller than the surface QDs due to the compressive strain from the capping layer. Besides, the AFM resolution is limited to around 2-10 nm by the AFM tip, which also makes the AFM overestimate the size of the QDs.

2.2-2 Transmission electron microscope

Unlike the AFM, the TEM technique needs complicated sample preparation procedure which takes much time. However, TEM images directly represent the geometry of the embedded quantum structures with high magnification. The resolution is determined by the matter wavelength of the high energy electrons and is able to reach 1-2 $\overset{\circ}{A}$. The image brightness is determined by the intensity of those electrons transmitted through the sample to the detector. Dislocation, strain field, and heavy elements in the crystalline specimen cause more electron scattering and lead to darker images in bright-field images. Therefore, the variation of the strain, element mass, and the thickness leads to the contrast of the TEM images.

In this study, the TEM images are taken by JEOL 2010F TEM system operated at 200 keV. The cross-sectional and plan-view specimens are prepared by mechanical polishing and further thinning in a Gatan 691 ion mill along the [010] and [001] zone axis, respectively. The thickness of the prepared samples should be a few tens to a few hundred nm to be transparent for the electrons. The cross-sectional images reveal the geometric shapes of the QDs, and the plan-view images are used to estimate the sheet density and the average diameter of the QDs. .

2.3 Photoluminescence Spectroscopy

The photoluminescence (PL) spectroscopy is used to investigate the electronic band structure and the crystal quality of our samples. Since all these III-V semiconductor quantum structures grown in our study are direct bandgap materials, the radiative recombination of electron-hole pairs is efficient enough for PL measurement. The samples are excited by an optical source with the photon energy h ν larger than the bandgap of the barrier materials. Electron-hole pairs (e-h pairs) are generated in the barriers. After a series of carrier thermalization process (including diffusion, capture, and relaxation), the spontaneous emission from the designed quantum structure occurs due to the radiative e-h recombination

and is analyzed by a set of detection system (including a monochromator and an optical detector).

In this study, three homemade PL systems are used for different aims. The conventional PL is used for the preliminary characterization of a mass of samples. The micro-PL is able to measure single QD or QR in magnetic fields up to 6 Tesla. The high-magnetic-field PL supplies the magnetic field up to 14 Tesla for the magneto-optical study at high field. For each system, the temperature of the measured samples can be cooled down to below 20 K in order to enhance emission intensity and reduce the thermal noise.

2.3-1 Conventional photoluminescence setup

The conventional PL is a convenient tool to investigate the fundamental optical properties of the semiconductor quantum structures, such as the emission energy, the PL intensity, the full width in half maximum (FWHM), the excitation power dependence, and the temperature dependence.

For conventional PL measurement, a mass of samples can be simultaneously mounted in a helium close-cycled cryostat, where the sample temperature can be controlled from 13K to room temperature. As depicted in Fig 2.3, the excitation source for conventional PL is an argon laser with wavelength of 514.5 nm. The luminescence of the sample is collected by a couple of plano-convex lenses, dispersed by a 550 mm monochromator, and detected by a thermal-electric cooled InGaAs (detection wavelength form 750 nm to 1750 nm) or an wavelength extended InGaAsSb (from 1750 nm to 2600 nm) photodiode. Via modulating the laser beams by a mechanical chopper, the emission signal is also modulated, and the lock-in amplifier is used to enhance the signal with the same modulation frequency and greatly improve the signal-to-noise ratio.
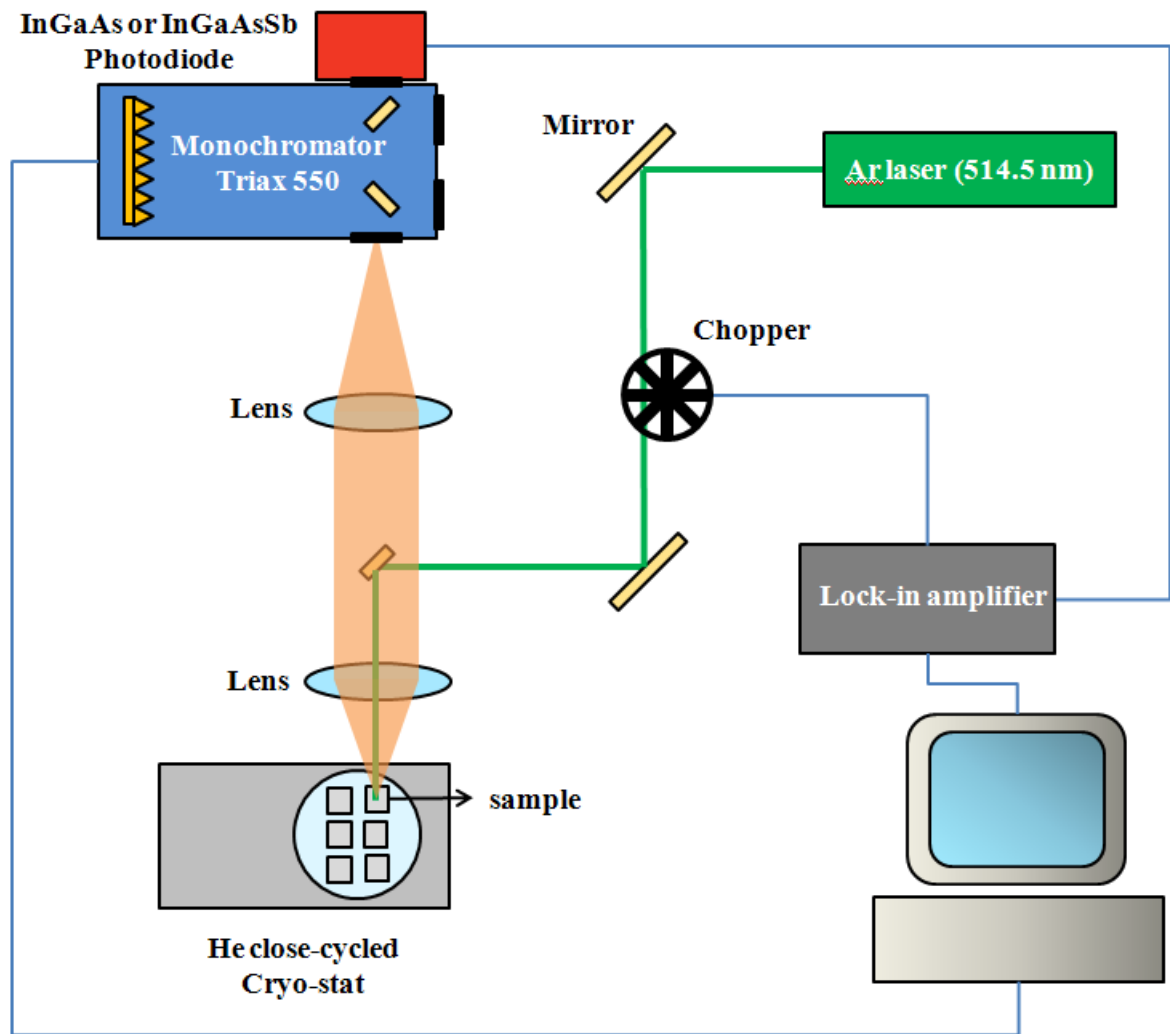
FIG. 2.3. The conventional PL system setup.

2.3-2 Micro-photoluminescence setup

By a 100 times long-working-distance objective lens, the spot size of the excitation beam can be focused down to only ~1.5 µm in this micro-PL system. The small spot size can provide ultra-high excitation power density to observe the emissions of the high-lying excited states in the QDs (or QRs). Besides, it allows the most important application, single QD spectroscopy. Sharp emission peaks from the single 3-D confined quantum system (QD and QR) can be observed in the single QD spectroscopy due to the delta-function-like density of states. The PL line width of single dot is limited by the system resolution (~50 µeV). By

eliminating the nonhomogeneous broadening, the fine structure of a single QD can be clearly distinguished and be further studied with magnetic fields applied parallel to the sample growth direction.

For micro-PL measurement, few samples are simultaneously mounted in a helium flow cryostat, where the sample temperature maintains at 10K. As depicted in Fig 2.4, the excitation source is a He-Ne laser with wavelength of 633 nm, and the excitation beam is focused by an objective lens. The luminescence of the sample is collimated by the same objective, dispersed by a 750 mm monochromator, and detected by a silicon charged coupled device camera (CCD) with the detection wavelength from 400 nm to 1000 nm. This silicon CCD contains 1024 x 256 pixels and is able to generate a spectrum without rotating the grating. The lock-in technique is unavailable for the CCD detection system.

In order to excite one QD only, an aluminum metal shadow mask with arrays of 300 nm diameter apertures is placed on the sample surface to isolate other QDs. Moreover, a very low dot areal density (about $1 \times 10^7 - 1 \times 10^9$ cm^{-2}) is also necessary to reduce the dot number inside the aperture. Since this dot density is less than 1/10 of the usual density (about 1×10^{10} cm^{-2}), the control of the growth condition (including the deposited amount of the dot material, the growth temperature, and the growth rate) is very critical for the kind of QD formation.
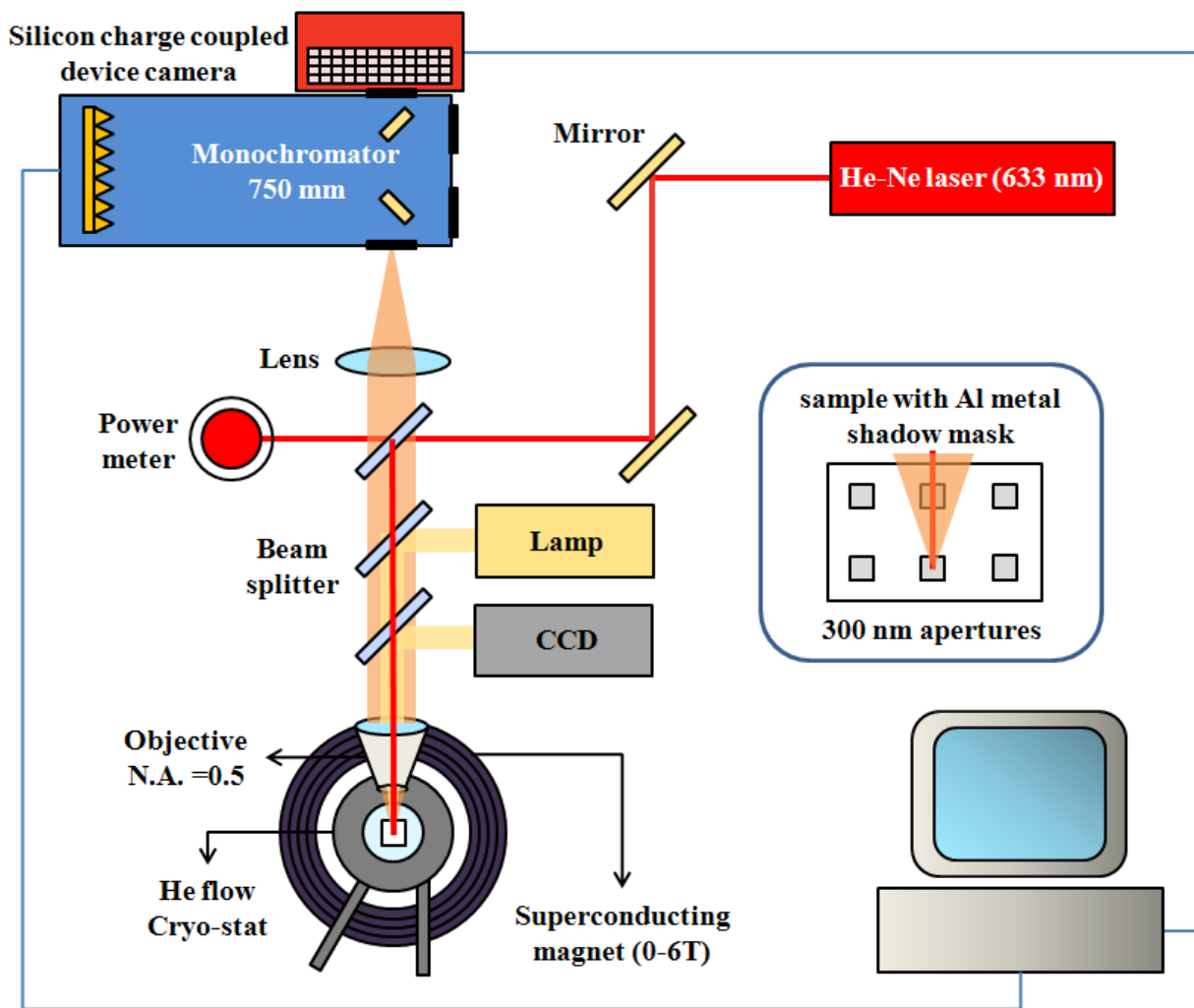
Fig. 2.4. The micro-PL system setup.

2.3-3 High-magnetic-field photoluminescence setup

In atomic physics, the magnetic field is usually applied to observe and analyze the splitting of the spectrum lines of atoms. The magnetic response reflects the orbital magnetic quantum number, the spin magnetic quantum number, and the spatial distribution of the excitonic wave function. Since the 0-D quantum dots and rings reveal the atom-like electronic structures, the magneto-PL can be used to study the excitonic fine structure states and the carrier wave function spatial extent of them.

For high-magnetic-field PL measurement, the sample is individually measured in an Oxford variable temperature insert (VTI) system with a base temperature about 1.4 K. A superconducting magnet provides a tunable and uniform magnetic field of up to 14 Tesla. The excitation source is a 532 nm Nd:yttrium aluminum garnet (YAG) laser or a wavelength-tunable Ti-sapphire laser ranging from 700 to 1000 nm. The latter is used for the photoluminescence excitation (PLE) measurement. A fiber bundle is used to couple the excitation source to excite the sample and collect the PL signal to the detection system.

Two designs of fiber bundles are shown as the inset in Fig 2.5. The simple one, design A, has a much larger laser spot size with diameter of around 4 mm and hence a much smaller excitation density. With a $45°$ Au-plated mirror, the magneto-PL can be performed in Voigt configuration (the magnetic field is applied perpendicular to the growth direction) as shown in the inset A-2. In order to improve the excitation power, another fiber bundle with a focusing lens, design B, reduces the laser spot size to 0.5 mm. The $30°$ tilted incident laser beam also minimizes the collection of laser beam to the detection system, which is important for the PLE measurement. However, due to the complicated and fixed design, the magneto-PL measurement in Voigt configuration is invalid for design B.
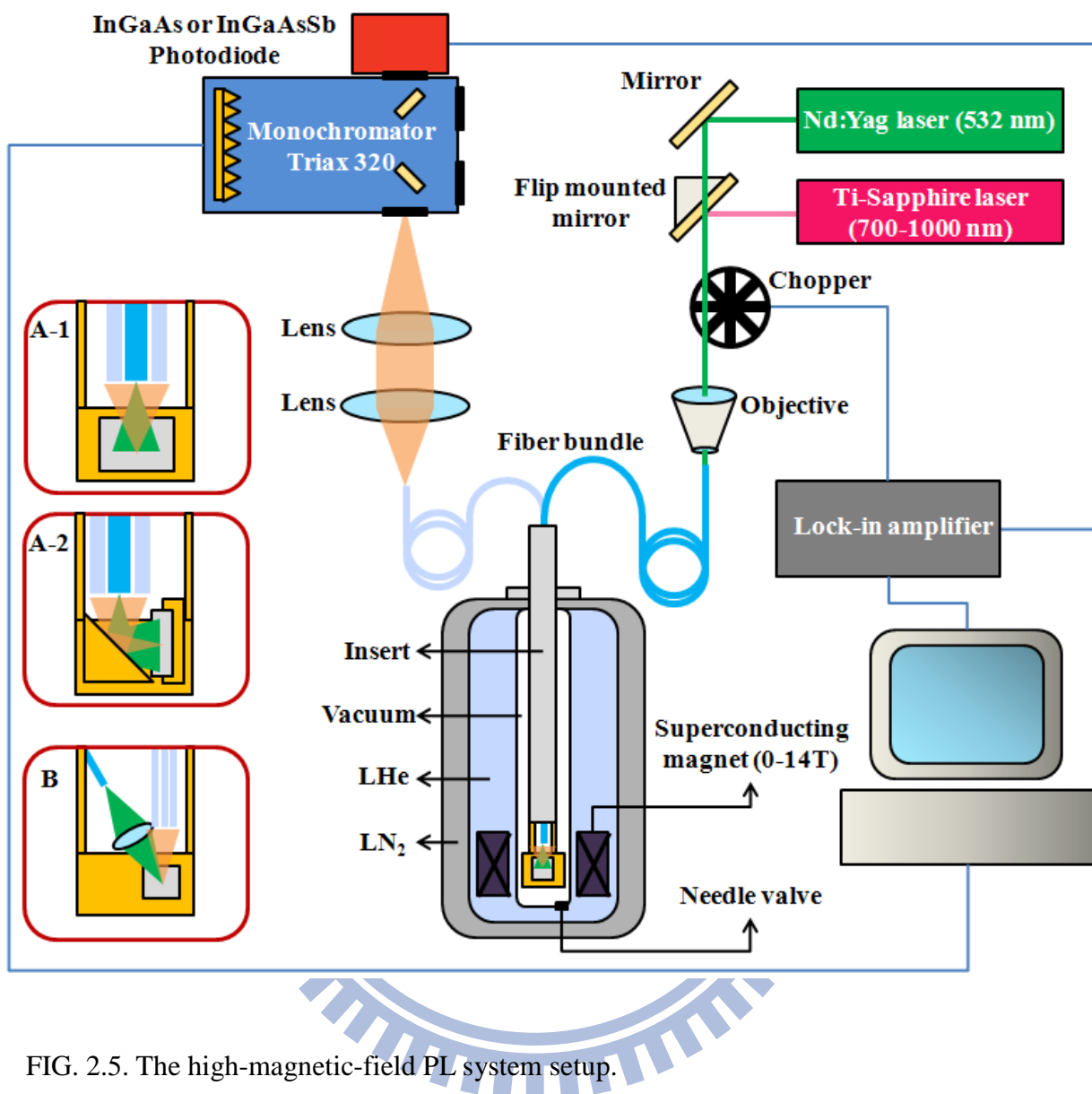
FIG. 2.5. The high-magnetic-field PL system setup.

Chapter 3

Impacts of Structural Asymmetry on the Magnetic Response of Single Self-Assembled In(Ga)As Quantum Rings

In this chapter, the diamagnetic shifts of neutral excitons and biexcitons confined in single self-assembled In(Ga)As/GaAs quantum rings are investigated. Unlike quantum dots, quantum rings reveal a considerably large biexciton diamagnetic shift, about two times larger than that of single excitons. Based on model calculations, we found that the inherent structural asymmetry and imperfection, combined with the inter-particle Coulomb interactions, is the fundamental cause of the more extended biexciton wave function in the quantum rings. The exciton wave function tends to be localized in one of the potential valleys induced by structural imperfections of the quantum ring due to the strong localization of hole and the electron-hole Coulomb attraction, resembling the behavior in single dots. Our results suggest that the phase coherence of neutral excitons in quantum rings will be smeared out by such wave function localizations.

3.1 Introduction

Charged particles confined to a nanoscopic quantum ring (QR) are expected to show unique magnetic responses, i.e., the well-known Aharonov-Bohm (AB) effect, due to the quantum interference of the carrier's wave function in the ring-shaped geometry. Experimental evidence of such a purely quantum mechanical effect has been observed in metallic and semiconductor mesoscopic rings [23-26] and recently in nanoscopic QRs [27-29]. On the other hand, the exciton properties in ring-like nanostructures also gained a lot of interest recently. Because an exciton is a charge-neutral composite, the AB effect is not expected to occur unless the electron and hole can propagate coherently in different

trajectories with a nonzero electric dipole moment [30]. Such a case appears naturally in type-II quantum dot (QD) systems [7, 8], where the electron and hole are spatially separated, resembling the behavior of single charges. However, for nanoscopic rings, such as InGaAs self-assembled QRs formed via partial capping of InAs QDs and subsequent annealing [13, 31], it is still an open question whether the excitonic AB effect can be observed when both the electron and hole are confined in the rings. In fact, this issue is further complicated by the inherent structural asymmetry and imperfections presented inevitably in self-assembled QRs. Although it has been demonstrated both experimentally and theoretical that the phase coherence of electron wave function in self-assembled QRs could survive [29], the impacts of inherent structural asymmetry and imperfection on the magnetic response of neutral excitonic species, such as excitons (X) and biexcitons (XX) with the presence of Coulomb interactions, have yet to be investigated.

In this work, we report the diamagnetic response of X and XX in single self-assembled QRs. Unlike single QDs, the XX confined in single QRs shows a considerably larger diamagnetic coefficient than the X. Guided by numerical model calculations, we found that the inherent structural asymmetry and imperfection, combined with the inter-particle Coulomb interactions, play a crucial role in the distribution of X and XX wave function in self-assembled QRs. Our results suggest that the phase coherence of neutral excitons in QRs will be smeared out by the wave function localization due to the structural asymmetry and imperfections.

3.2 Growth Condition

The InAs QRs were fabricated by Varian Gen-II molecular beam epitaxy (MBE) on a GaAs (001) substrate. Low density QDs were first grown by depositing two monolayers of InAs at 520 ^{o}C under As$_2$ atmosphere as QR precursors. The growth rate for InAs QDs is as low as 0.033μm/hr to reduce the number of the dots. The substrate temperature was then lowered to 500 ^{o}C. A thin GaAs layer of 1.7 nm was deposited to cover the QD sidewalls, and a 50-sec growth interruption under As$_2$ flux was performed for a dewetting process which expels the indium atoms from the center of the QDs to move outwards for the QR formation. Finally, the GaAs barrier layer with 1 μm/hr growth rate was grown to complete the growth process. Note that this high growth rate for GaAs barrier was needed to minimize the deformation of the morphology of the as grown structure. Figure 3.1 depicts the formation of the QRs Further details can be found in Ref. [13].
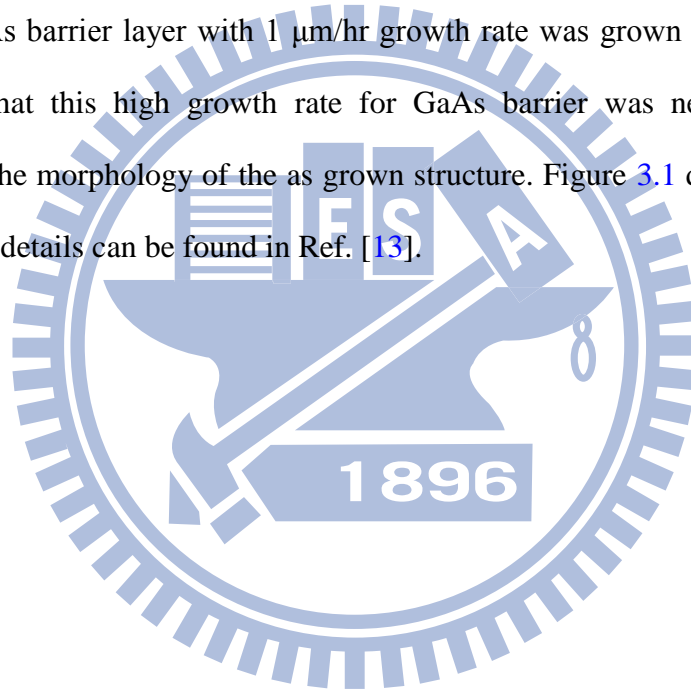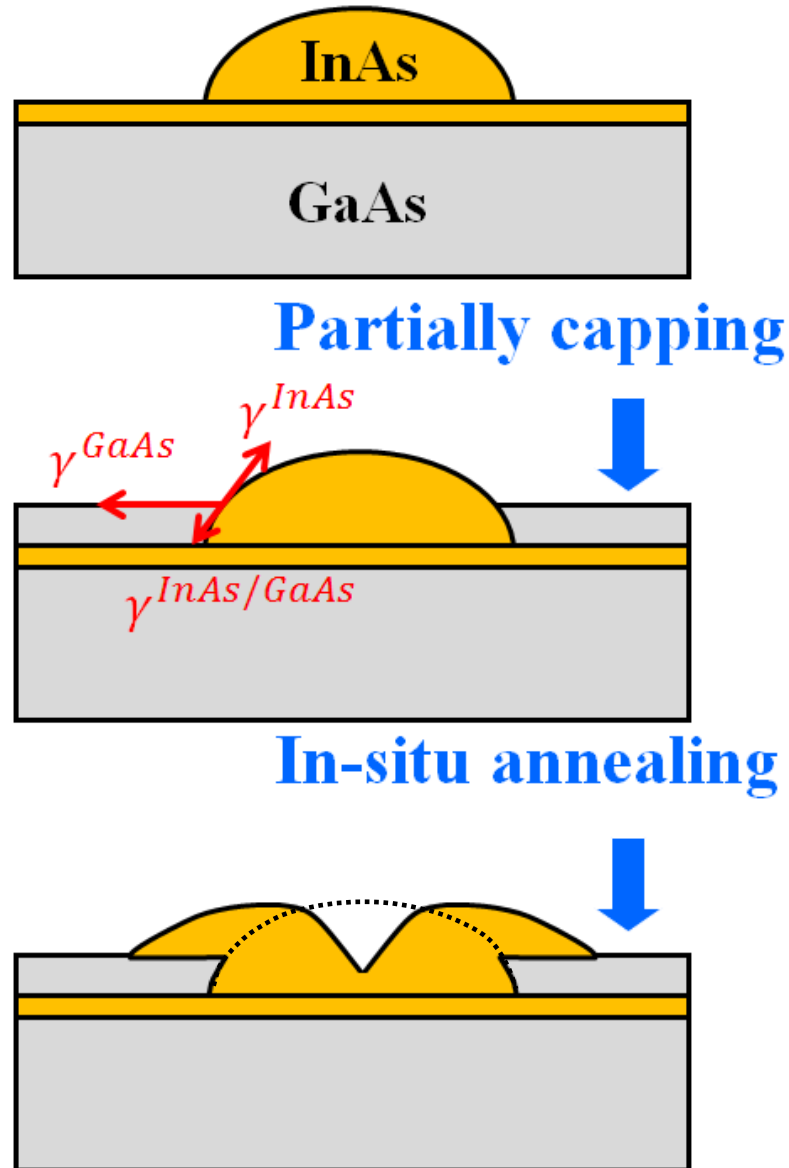
FIG. 3.1. The schematic diagram of the QR formation.

3.3 Structural Characterization

Surface topography of uncapped QRs has been investigated by atomic force microscopy. The area density of surface QRs is estimated to be about 1×10^7 cm^{-2}. As shown in Fig. 3.2, the surface QR has a rim diameter of 35 nm, a height of ~1.3 nm and a center dip of about 2 nm. The realistic dimension of the embedded QRs is expected to be much smaller [32]. We also found that the QR is anisotropic; the rim of the surface QR is higher along [1-10].
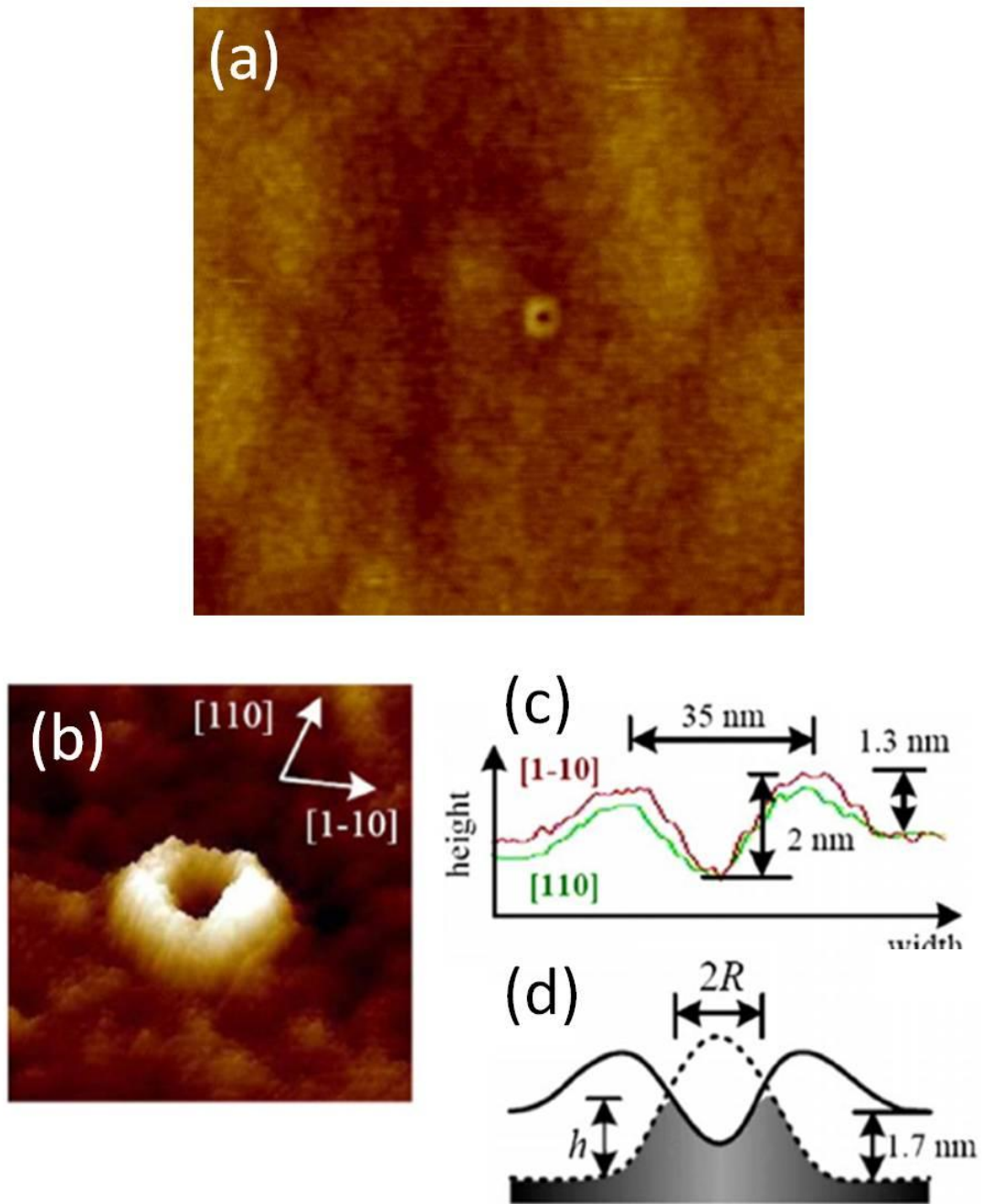
FIG. 3.2. (a) and (b) The AFM image of the surface QR. (c) Topographical line scans along the [110] and the [1-10] directions. (d) A schematic for the surface QR profile (solid line), the precursor QD (dash line), and the indium-rich part of the embedded QR (gray part).

3.4 Photoluminescence of QR Ensemble

The PL of QR ensemble was measured by a conventional PL system. The sample was mounted in a helium close-cycled cryostat at the measurement temperature of 20K. The PL was excited by a 514.5 nm argon laser, dispersed by a 550 mm monochromator and detected by a thermal-electric cooled InGaAs photodiode. Further details are described in section 2.3-1. The PL spectra of the QR ensemble and the precursor QD ensemble are plotted in Fig 3.3. The emission energy of the QRs is found to be much higher than that of the precursor QDs due to the reduction of the height and the intermixing between In and Ga atoms during annealing. Besides, the FWHM of the QRs of 30 meV is smaller than that of the QDs of 42 meV. This is attributed to the better uniformity in the height of the rings after annealing.
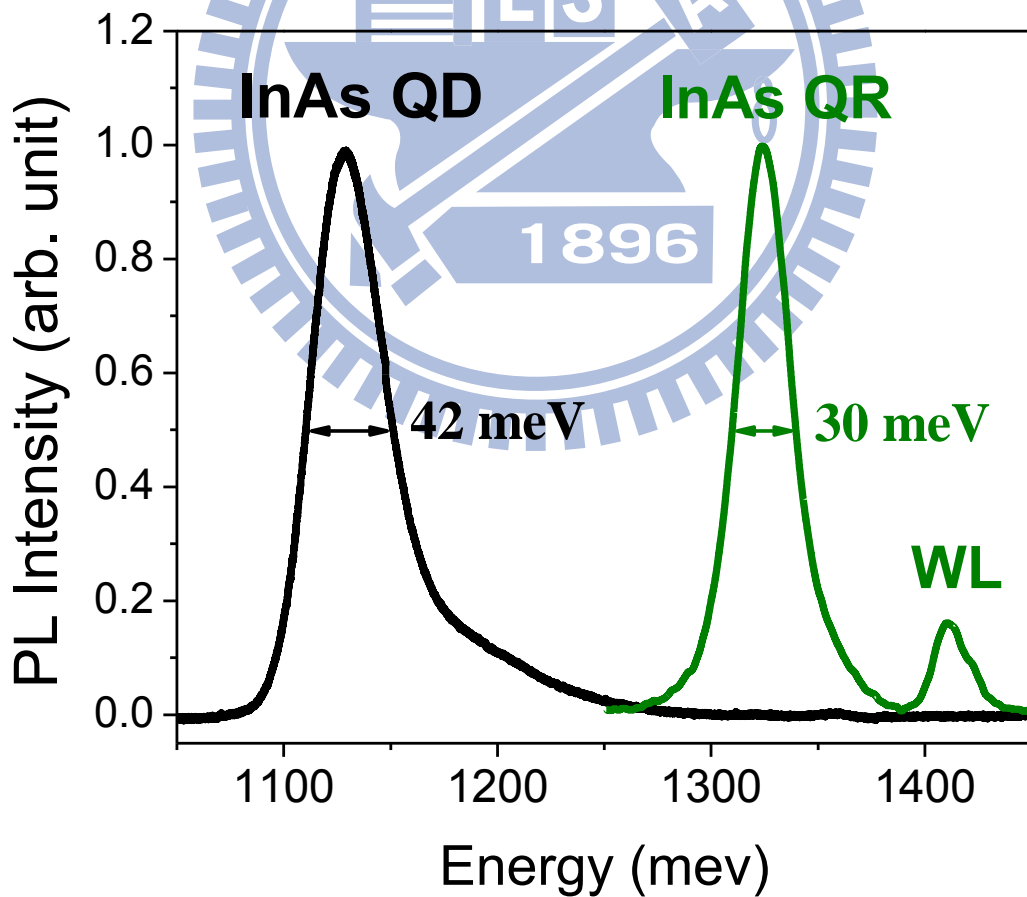
FIG. 3.3 PL spectra taken from the QR ensemble and from the QD ensemble.

3.5 Single Ring Spectrum and Excitation Power Dependence

The single QR emissions were measured by a low-temperature micro-photoluminescence (µ-PL) setup combined with a 6 T superconducting magnet. The sample was mounted in a helium flow cryostat at the measurement temperature of 10K. The PL was excited by a 633 nm He-Ne laser, dispersed by a 750 mm monochromator and detected by a silicon charge coupled device (CCD) camera. An aluminum metal shadow mask with arrays of 300 nm diameter apertures were used to isolate single QR emissions. Further details are described in section 2.3-2. A comparison between the PL spectra for the QR ensemble and a single QR is displayed in Fig. 3.4. The QR ensemble shows an emission peak at 1329 meV with a line width of 26 meV due to size fluctuations. For the single QR, the spectrum is dominated by a sharp emission line near 1320 meV with a resolution limited line width of ~ 50 µeV.
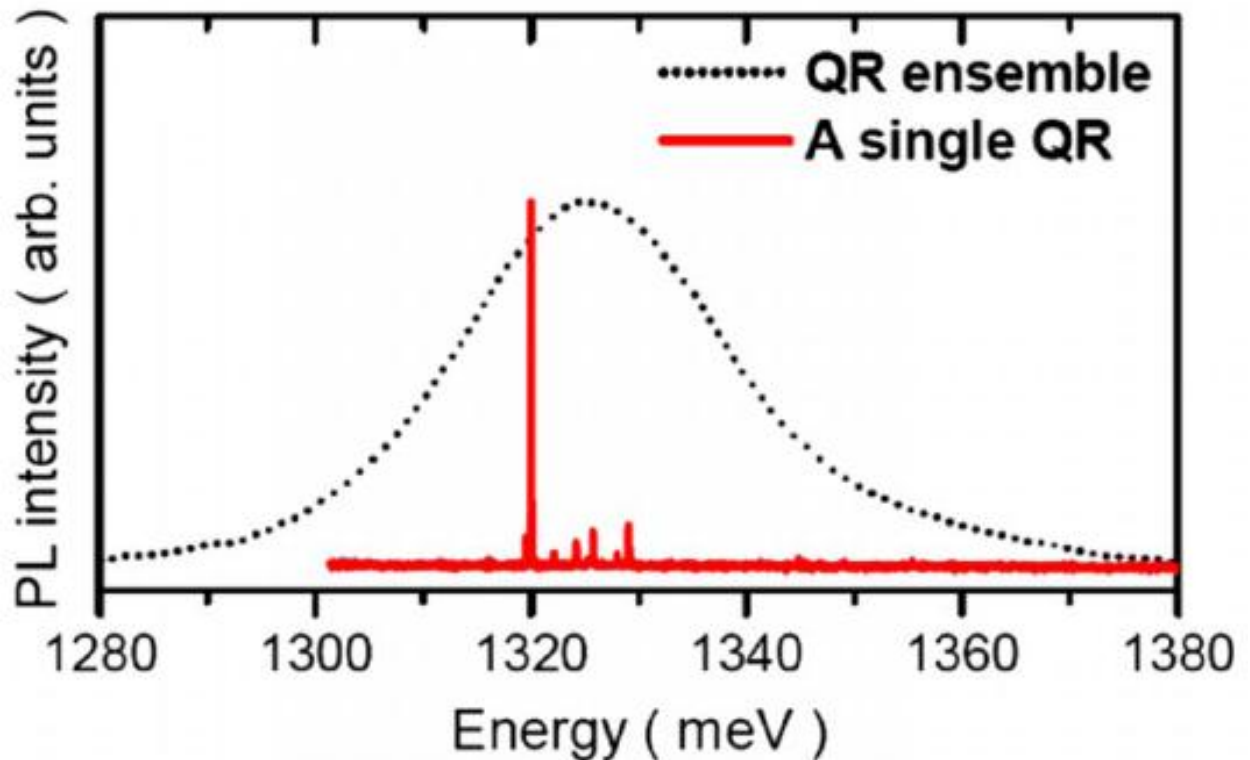
FIG. 3.4 PL spectra taken from the QR ensemble and from a representative single QR.

Figure 3.5(a) shows the PL spectra taken from a representative single QR under different excitation powers. Two ground-state emission lines associated with the recombination from exciton (X) and biexciton (XX) states can be observed, which have been identified according to linear and quadratic power dependence of intensity as shown in Fig. 3.5(b). The schematic diagram of the recombination process of the X and XX emissions are depicted in Fig. 3.5(c). The same measurement has been performed on a total of seven QRs. The emission energies of X are in the range of 1320-1328 meV, while the biexciton binding energies (defined as $E_X - E_{XX}$) are varying from 0.2 to 0.7 meV for different QRs.
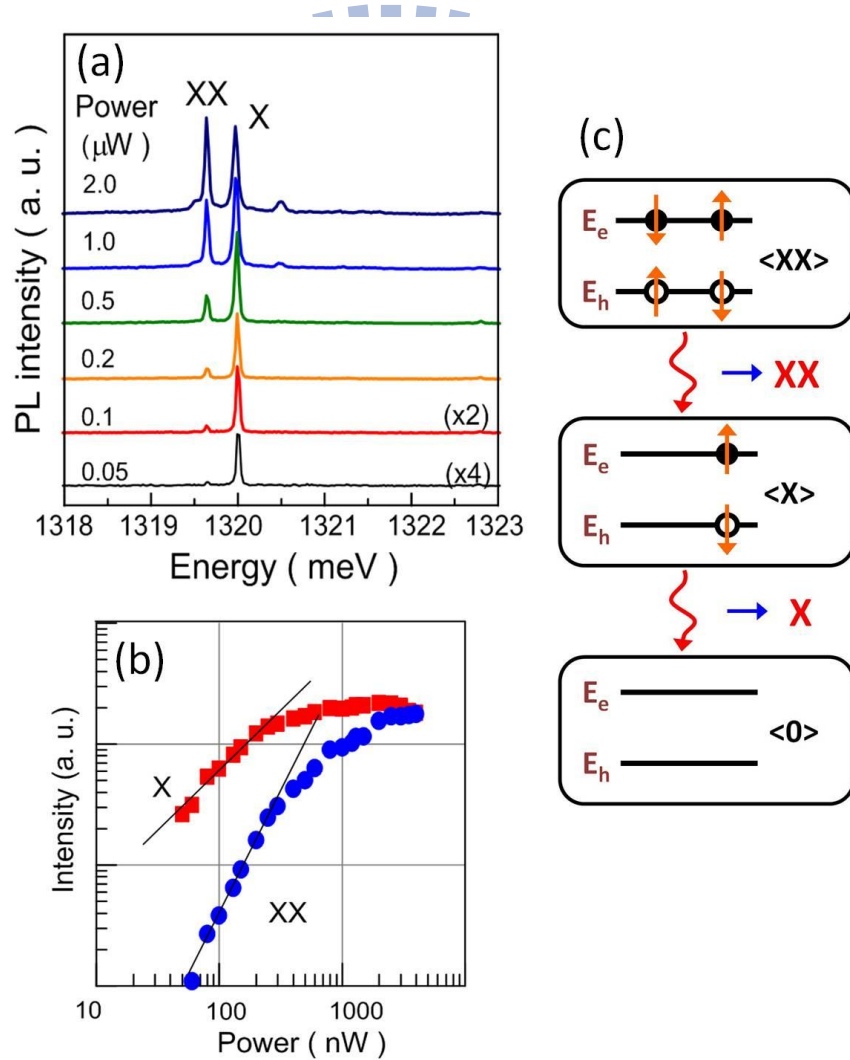
FIG. 3.5. (a) Power-dependent PL spectra of a single QR. (b) The integrated intensity of X and XX lines as a function of the excitation power. (c) The recombination process of X and XX emissions.

3.6 Level Splitting

We have investigated the exciton level splitting in those QRs. As shown in Fig. 3.6(a), for X and XX emissions, the energy difference between the emission peaks measured using horizontal and vertical linear-polarization filters are estimated to be smaller than 5 μeV. This is different from the case of the QDs, where a fine splitting of about 50μeV for the exciton and the biexciton levels is clearly observed as shown in the Fig. 3.6(b). This exciton splitting of QDs has been also reported in Ref. [33-36] and is attributed to the electron-hole exchange interaction arising from the in-plane confinement potential anisotropy. Therefore, the observed degeneracy of the exciton states in QRs suggests that the confinement potential of QRs is much more isotropic than that of QDs. Since the self-assembled QRs have a geometric azimuthal asymmetry [32], the more isotropic confinement potential probably results from the composition intermixing by the in-situ annealing, which weakens the variation of the confinement potential [36]. This characteristic means InAs quantum rings are suitable for the applications in quantum information which requires the emission of the entangled photon pairs with undistinguished emission energies.
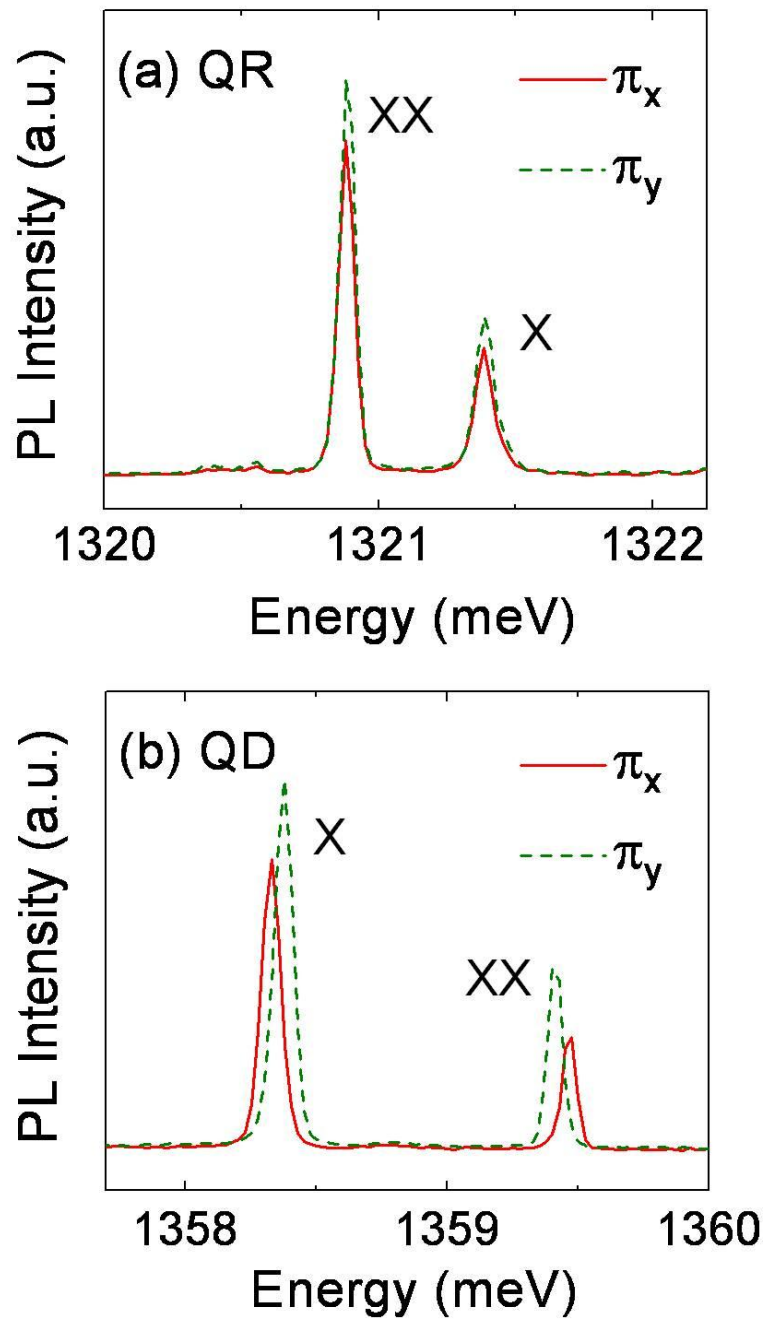
FIG. 3.6. PL spectra of (a) a single InAs quantum ring and (b) a single quantum dot. The solid line and the dash line stand for the orthogonal linear polarizations.

3.7 Magneto-photoluminescence

When an external magnetic field is applied along the growth direction, each of X and XX lines splits into a cross circularly polarized doublet due to the spin Zeeman effect, as presented in Fig. 3.7. Because the exciton state is the final state of the spin-singlet biexciton state, both X and XX show an identical energy splitting of 131 μeV/T, corresponding to an excitonic g-factor of $|g| = 2.3$, a reasonable value for the InAs nanostructures embedded in GaAs matrix. The average energy of each Zeeman doublet shows a quadratic dependence on B, i.e. the diamagnetic shift, which can be fitted to βB^2, where β is the diamagnetic coefficient. The average diamagnetic coefficient of X for all the investigated QRs is $\beta_X = 6.8$ μeV/T^2. Interestingly, we found that the XX shows a considerably larger diamagnetic coefficient with an average value of $\beta_{XX} = 14.8$ μeV/T^2, which is more than the double of the β_X value. Table 3.1 presents the exciton energy (Ex), the biexciton binding energy (Ex-Exx), the diamagnetic coefficient of X (β_x), the diamagnetic coefficient of XX (β_{xx}), and the excitonic g-factor (g_{ex}) of six single QRs.

The diamagnetic coefficient is proportional to the area of the excitonic wave function. Our results suggest that the XX wave function is more extended than that of X in a QR. This is different from the case of QDs [33, 34, 37, 38], where the diamagnetic response of XX is usually similar to, or somewhat smaller than, that of X due to the different spatial extents of the electron and hole wave functions and their responses to the applied B.
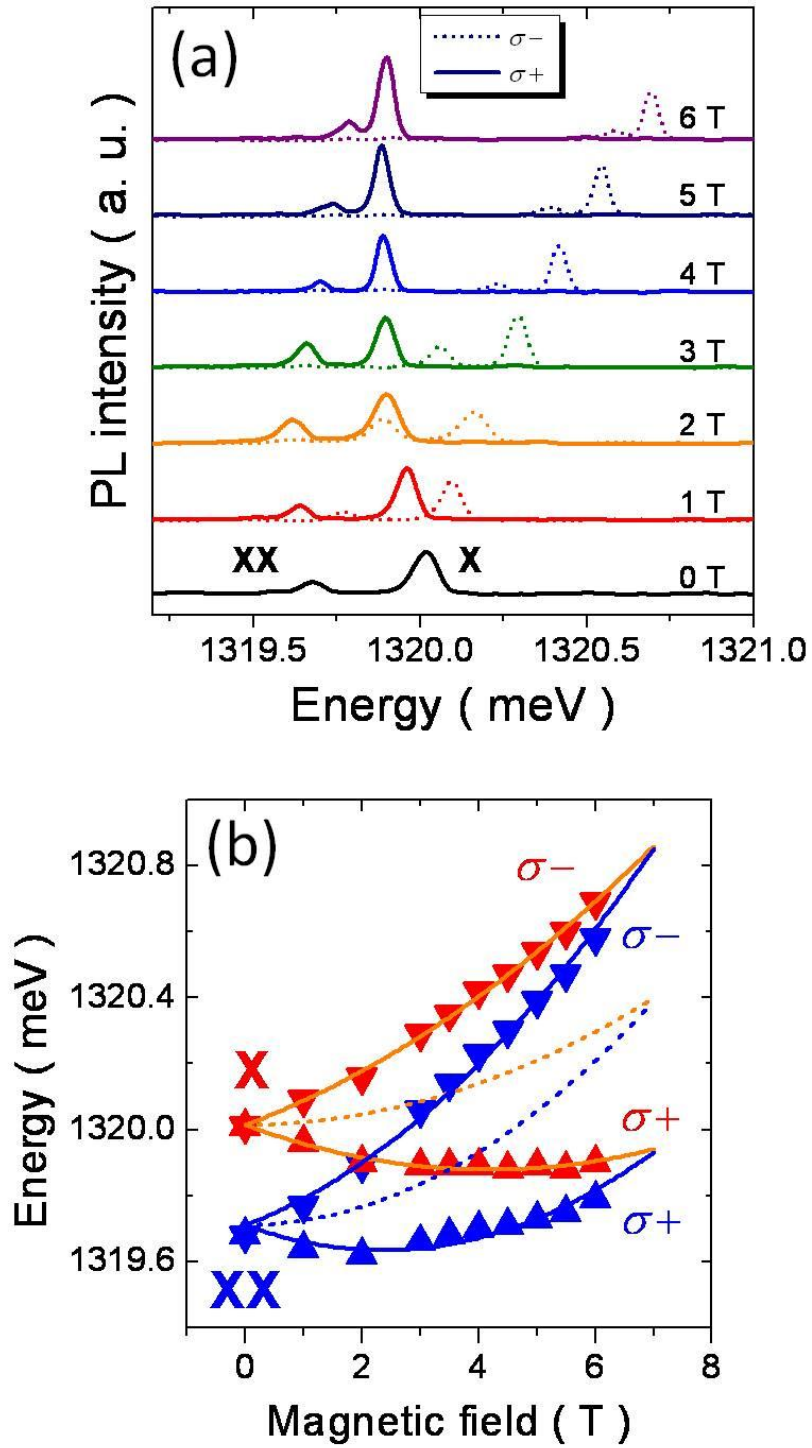
FIG. 3.7. (a) Magneto-PL spectra for X and XX lines in different magnetic fields. (b) Emission peak energies of the X and XX Zeeman doublets as a function of the magnetic field. Dash lines are quadratic fits to the averages of the Zeeman doublets.

40

	QR1 (A114)	QR2 (A144)	QR3 (A225)	QR4 (A245)	QR5 (A325)	QR6 (A634)
Ex (meV)	1325.57	1324.84	1327.65	1323.92	1325.85	1332.22
Ex–Exx (meV)	-0.33	-0.75	-0.34	-0.51	-0.30	-0.25
βx ($\mu eV/T^2$)	7.8	5.7	6.4	7.1	7.1	6.6
βxx ($\mu eV/T^2$)	13.8	15.7	13.3	14.6	14.1	17.3
g_{ex}	-2.26	-2.43	-2.16	-2.11	-1.98	-2.53

Table 3.1. The exciton energy (Ex), the biexciton binding energy (Ex-Exx), the diamagnetic coefficient of X (β_x), the diamagnetic coefficient of XX (β_{xx}), and the excitonic g-factor (g_{ex}) of six single QRs.

Here we argue that the more sensitive diamagnetic response of XX is a consequence of the fact that self-assembled QRs do not have perfect azimuthal symmetry. It has been reported that the structure of buried self-assembled QRs shows an asymmetric crater-like shape, with a diameter substantially smaller than the ring-shaped islands on the surface of uncapped QR structures. In addition, due to the preferential out diffusion of dot material along the [1-10] direction, the embedded rim height is higher along the [110] direction, resulting in two separate potential valleys along the [110] direction [39], resembling a pair of connected QDs. The lack of rotational symmetry in the potential of embedded QRs is expected to have significant impacts on the diamagnetic responses of X and XX. For a neutral X, the height variation strongly localizes the hole inside one of the potential valleys due to the large effective mass. Consequently, the electron will be bound to the same valley by the electron-hole Coulomb attraction. This means that the wave function extent of X is determined mainly by the confinement of the potential valley and the Coulomb interaction. Therefore, the diamagnetic response of X is similar to an elliptic QD.

For a neutral XX confined in the QR, the two holes may be separately localized in different valleys due to the strong hole-hole Coulomb repulsion and the negligible coupling of hole states between the two valleys. Due to the Coulomb attractions of the two separately localized holes, the electron wave functions of XX are more likely to spread over the two valleys and become more extended than that of X. Unlike X, the wave function extent XX is determined mainly by the diameter of the embedded QRs.

3.8 Simulation

In order to further attest our assertions, we performed calculations of the X and XX states in our QRs based on structural information obtained from our AFM topography and the proposed shape of embedded QRs reported in Ref. [32]. A one-band effective mass Hamiltonian was used to calculate the single-particle states. The Coulomb interaction between the electron and hole was then treated self-consistently. According to Ref. [32, 39], we model the QR as a nanoscale crater with a rim radius of $R = 7$ nm and an average rim height of $h_M = 2.5$ nm. The height of the crater is expected to be as a function of the radial coordinate ρ.

$$h(\rho) = h_0 + \frac{(h_M - h_0) \cdot \left(1 - \left(\rho / R - 1\right)\right)^2}{\left[(\rho - R) / r_0\right]^2 + 1} , \quad \rho \leq R , \tag{3.1}$$

$$h(\rho) = h_\infty + \frac{h_M - h_\infty}{\left[(\rho - R) / r_\infty\right]^2 + 1} , \quad \rho > R , \tag{3.2}$$

where $r_0 = 2 \; nm$ and $r_\infty = 3.5 \; nm$. To simplify the calculations, the QR is modeled with an azimuthal symmetric geometry with an azimuthal asymmetric potential $V_H(\rho, \varphi)$ deduced from the z-axis quantization energy variation arising from the height anisotropy. The potential is therefore simplified to $V_H(\rho, \varphi) = V_0(\rho) \cos 2\varphi$, where $V_0(\rho)$ is proportional to the height anisotropy factor ξ_h. Figure 3.8(b) and 3.8(c) depict the QR height profile and the corresponding radial potential $V_0(\rho)$ for the electron for an anisotropy factor of $\xi_h = 0.15$. The corresponding maximum V_0 is 19.5 meV and 9.8 meV at the rim for the electron and hole, respectively. The band offset of conduction (valence) band is 300 meV (180 meV) from the strained $In_{0.7}Ga_{0.3}As/GaAs$ QDs [17]. The effective mass of electron (hole) is taken as 0.067 m_0 (0.5 m_0).

The calculated electron wave functions for the lowest energy states of X and XX are plotted in Fig. 3.8(d) and 3.8(e), respectively. It can be seen that X is well confined in one side of the QR with a less extended wave function. By contrast, the electron wave function of

XX spreads over both sides of the QR. For the two equivalent potential valleys in a QR, it may be expected that the exciton wave function is distributed symmetrically in both valleys. However, the calculation reveals that the lowest energy state is the localized exciton in one valley (i.e. either of the two) due to its stronger e-h Coulomb interaction. In other words, the exciton Bohr radius (about 11 nm for InAs QR) is slightly smaller than the ring diameter, which concentrates the exciton wave function into one side of the QR. The diamagnetic response of X and XX can be further calculated by superimposing a magnetic confining potential to the QR potential. By fitting the calculated energy shift to the quadratic energy dependence βB^2 as depicted in Fig. 3.8(f), the diamagnetic coefficients of X and XX are found to be β_X= 10.7 μeV/T^2 and β_{XX}= 23.0 μeV/T^2, respectively. Although the model QR shape may be different from the actual shape of our QRs, our simulations demonstrate unambiguously that the asymmetric potential indeed impacts the diamagnetic response of X and XX, which agrees very well with our experimental finding.
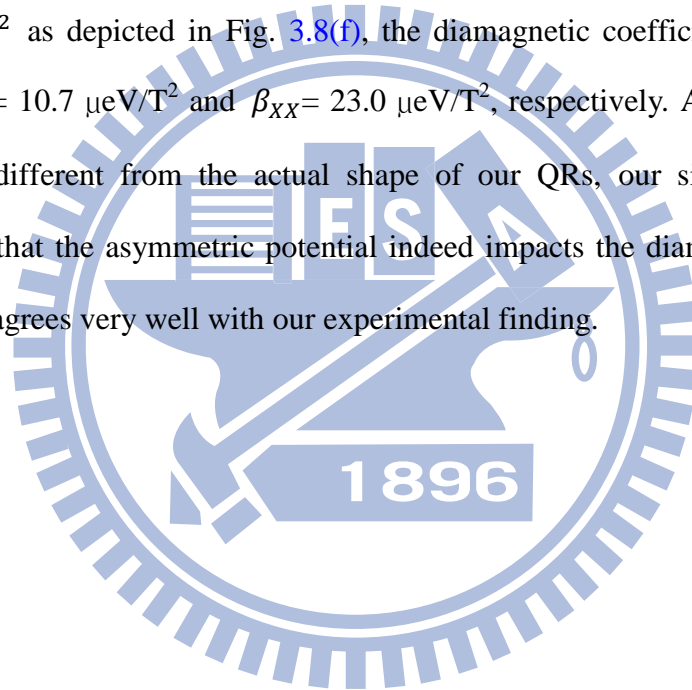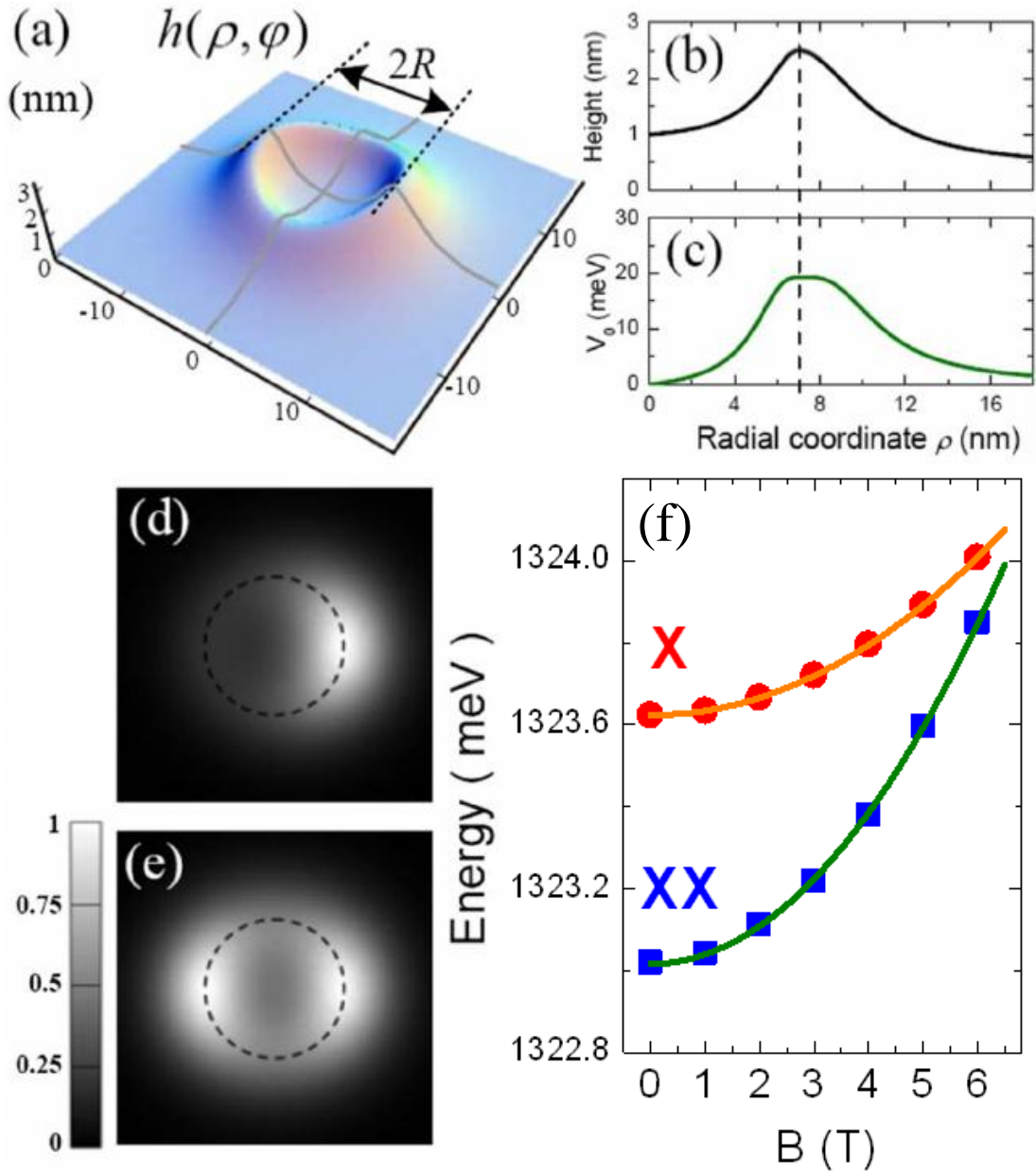
FIG. 3.8. (a) A schematic for the QR geometry with an anisotropy factor $\xi_h = 0.15$ used in our model calculations. (b) and (c) are the height profile $h(\rho)$ and the electron radial potential $V_0(\rho)$ of the model QR. (d) and (e) are the calculated electron wave functions of the lowest X and XX states. The dash circle represents the rim diameter of 14 nm. (f) The emission energies of X and XX as a function of B. β_X and β_{XX} are found to be 10.7 μeV/T^2 and 23.0 μeV/T^2 by fitting to $E = \beta B^2$.

3.9 Conclusion

In brief, the diamagnetic responses of excitons and biexcitons confined in single self-assembled QRs have been investigated. Unlike single QDs, the biexciton confined in single QRs shows a considerably larger diamagnetic coefficient than the exciton, implying the more extended biexciton wave functions in the ring. The lack of perfect rotational symmetry in the potential of embedded QRs due to the inherent structural asymmetry is the fundamental cause of the more extended biexciton wave function. The strongly localized holes in potential valleys of QRs leads to a localized exciton wave function due to the electron-hole Coulomb attraction, while makes the biexciton wave function being able to spread over the ring due to the hole-hole Coulomb repulsion. In other words, the Coulomb interactions combined with the reduced azimuthal symmetry caused by inherent structural imperfection could destroy any of the expected novel magnetic response that relies on the rotational symmetry of exciton and biexciton wave functions confined in self-assembled QRs.
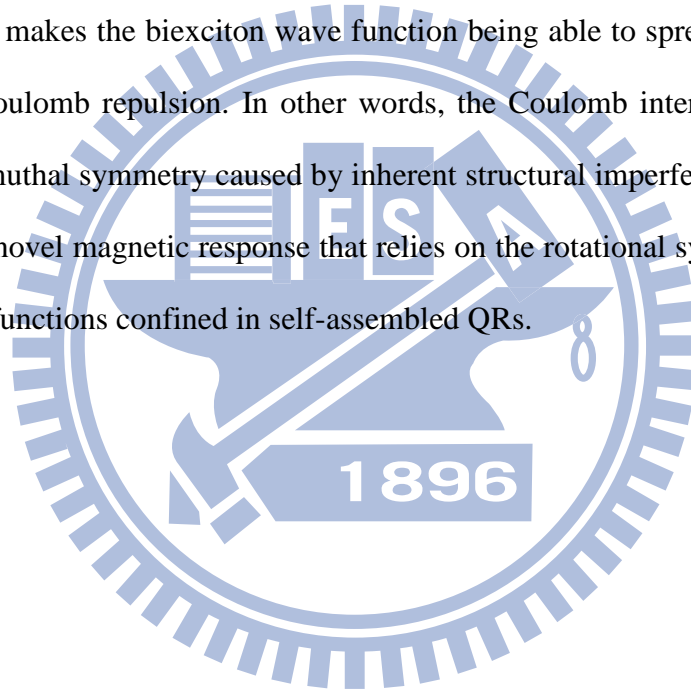
Chapter 4

Anomalous Optical Magnetic Red Shift of Self-Assembled

GaSb/GaAs Quantum Dots

In this chapter, we report the magneto-photoluminescence measurement results on type-II self-assembled GaSb/GaAs quantum dots with the magnetic field applied in Faraday and Voigt configurations. The emission of the quantum dots exhibited a typical diamagnetic blue shift when the magnetic field was applied in a Faraday configuration. However, when the magnetic field was in the Voigt configuration, an unusual red shift in the emission peak accompanied with a rapid increase of the PL intensity was observed. Guided by numerical calculations, the magnetic field applied in the Voigt configuration is found to provide an additional vertical confinement to electrons and therefore substantially enhance the radiative electron-hole recombination. The resulting decrease of the steady-state hole concentration gives rise to the observed anomalous magnetic red shift. Furthermore, the electron wave function was found to be distributed above and below the QD, and the wave function was not ring-like. This eliminates the probability of the observation of the Aharonov-Bohm oscillation.

4.1 Introduction

Type-II self-assembled quantum dots (QDs), where the staggered band lineup spatially separates the electrons and holes, have attracted considerable interests for the exhibition of novel physical phenomena, such as optical Aharonov-Bohm effect in magnetic fields [7, 8, 21], and the potential application for carrier storage devices [18]. In the self-assembled GaSb QDs embedded in GaAs matrix, holes are strongly localized inside the QDs with a large activation energy of about 450 meV [18], and the electrons are weakly bound in GaAs regions

next to the GaSb QDs by the Coulomb attraction. The magneto-photoluminescence (PL) measurements for this material system have been carried out in the past to investigate the extent of the electron wave function. However, it was usually done in a Faraday configuration, where only the lateral electron-hole (e-h) spatial separation was revealed [41-44]. Because of the shape of the QDs, where the height is much smaller than the width, electrons are mostly confined in GaAs regions above and below the QDs [21]. Therefore, the optical properties of the excitons in these QDs have stronger dependence on the vertical e-h separation. This separation, however, can only be studied with the magnetic field applied in the Voigt configuration.

In this work, we compared the magneto-PL results of type-II GaSb/GaAs QDs with the magnetic field applied in both the horizontal and the vertical directions. When the magnetic field was applied in a Faraday configuration, the QD emission revealed a typical diamagnetic blue shift along with a slightly decreased PL intensity. However, when the magnetic field was in a Voigt configuration, an unusual red shift in the emission peak accompanied with a rapidly increased intensity was observed. By means of numerical model calculations, this anomalous optical magnetic response is attributed to the reduction of the vertical e-h separation and the resulting increase of the radiative e-h recombination rate in the magnetic fields applied in the Voigt configuration.

4.2 Growth Condition

The GaSb QD sample (Rn283) was fabricated on a GaAs (001) substrate by a Veeco Gen-II molecular beam epitaxy (MBE) system equipped with valve crackers of Sb_2 and As_4 source. Nominal 3 monolayers (MLs) of GaSb were deposited at 500 ℃ to form self-assembled QDs. The V/III flux ratio was about 5, and the growth rate was 0.2 ML/s. Here, 1 ML of GaSb means the number of GaSb molecules that is needed to form a continuous GaSb layer pseudomorphically matched to GaAs. The GaSb QD layer was sandwiched

between a 150 nm GaAs buffer layer and a 150 nm GaAs capping layer. After the growth of the GaAs buffer layer, the As shutter was closed, the Sb shutter was opened, and the GaSb film was immediately deposited. Following that, a 1 min interruption under Sb_2 flux was performed. We used As_4 as the arsenic source instead of As_2 to avoid the intermixing between Sb and As atoms during the growth process [45].

4.3 Structural Characterization

The surface topography of the uncapped QDs was measured by an atomic force microscope (AFM) and is shown in Fig. 4.1. The areal density of QDs was estimated to be about 7×10^9 cm^{-2} with the average dot height of about 12 nm (±2 nm) and the base width of about 55 nm (±8 nm). However, the realistic dimensions of the embedded QDs are expected to be much smaller due to the overestimation of AFM [46].
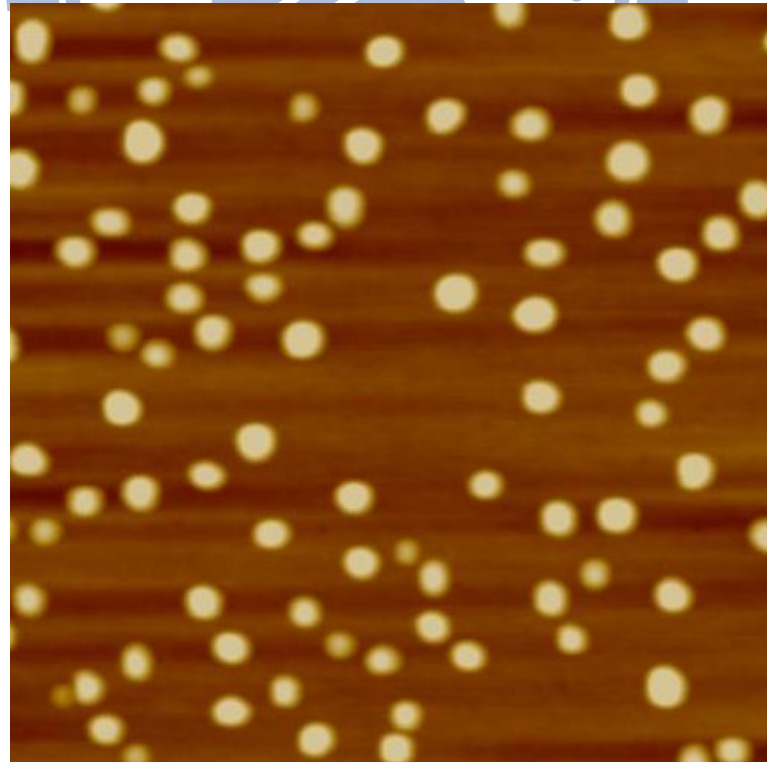
FIG. 4.1. AFM surface image of GaSb QD sample in 1 μm square image area.

4.4 Conventional PL and Excitation Power Dependence

Conventional PL and magneto-PL measurements were performed at 1.4 K with a 14 Tesla superconducting magnet. The sample was excited by Nd:yttrium aluminum garnet (YAG) laser at 532 nm via an optical fiber. The laser spot size on the sample is around 0.4 cm^2. The PL signal was collected by a fiber bundle, dispersed by a 320 mm monochromator, and detected by an InGaAs photodiode.

Figure 4.2 presents the zero-field PL spectra for the GaSb/GaAs QD sample taken at different pumping powers. The observed two prominent emission peaks are originated from the WL with a peak energy around 1.28 eV and from the QD ensemble with a peak around 1.0 eV. When the excitation power increases, both the emission peaks reveal energy blue shifts in proportion to the 1/3 power of excitation power density as seen in the inset. This blue shift is a signature of type-II structures and is attributed to the band bending, the capacitive Coulomb charging, and the excited state filling effects by the photoexcited holes as shown in Fig 4.3 [47, 48].
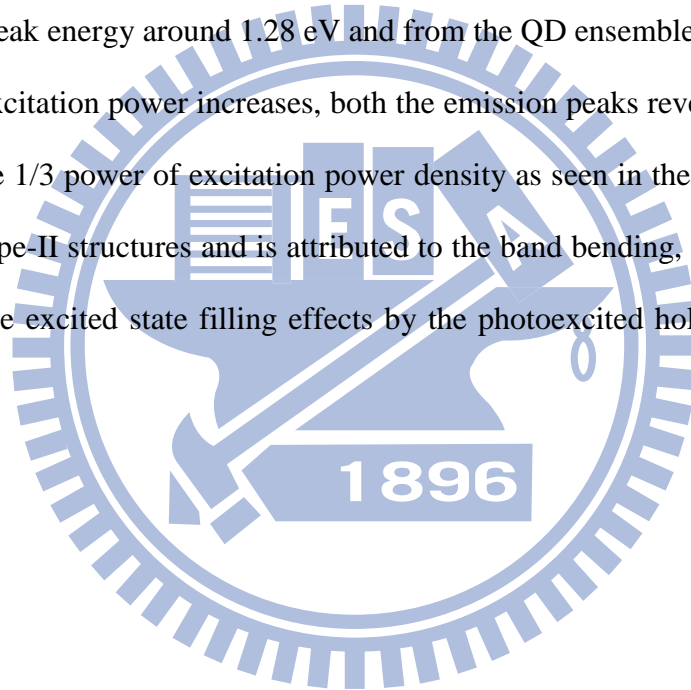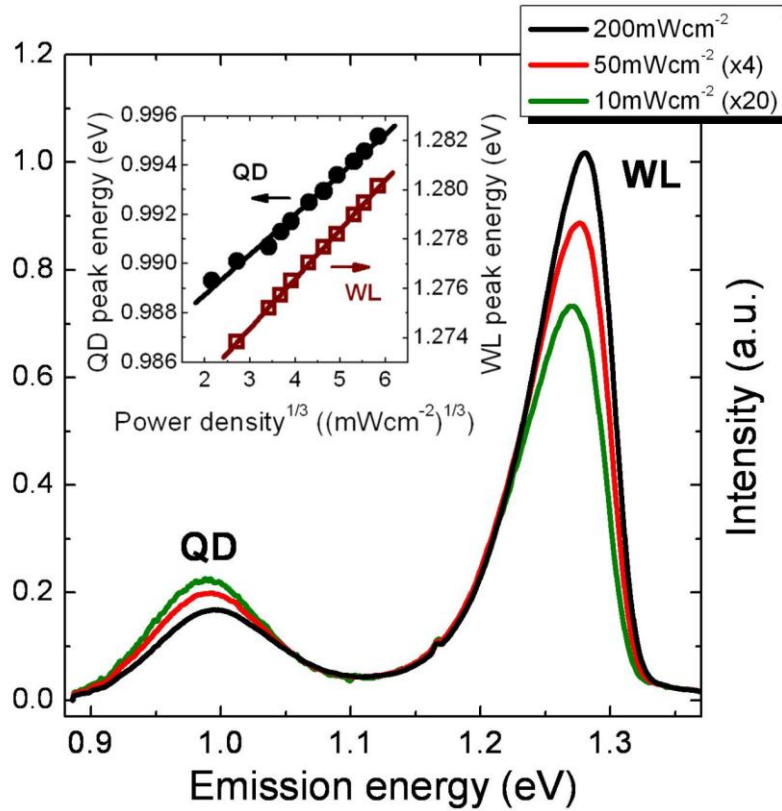
FIG. 4.2 The zero-field PL spectra taken at different excitation powers. The inset depicts the QD and the WL emission peak energies as a function of the 1/3 power of the excitation power density.
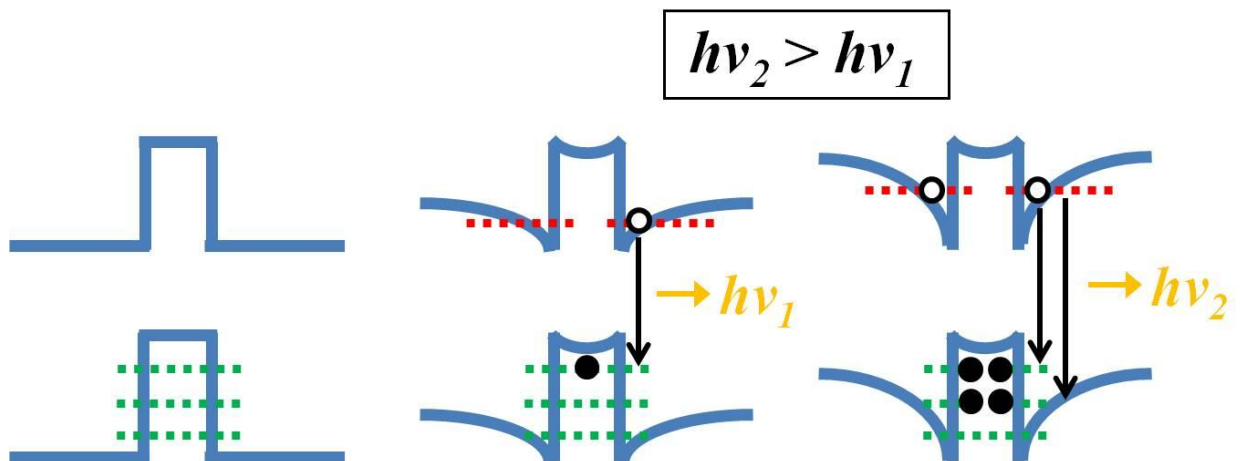
FIG. 4.3 The band lineups of the GaSb/GaAs QDs at different excitation powers. The higher excitation power induces more photoexcited holes and the resulting increase of the exciton energies.

4.5 Magneto-PL Measurements in a Faraday Configuration

The PL spectra have been measured with the magnetic field applied along the growth direction (in a Faraday configuration). Figure 4.4 displays the emission peak energy shifts of the QDs and the WL as a function of the magnetic field. At low fields, both QD and WL emissions reveal a typical diamagnetic blue shift, which has a quadratic dependence on the magnetic field. The diamagnetic coefficients of the WL emission measured at different excitation powers are almost the same and are about two times those of the QD emission. The much smaller diamagnetic coefficients of the QDs are associated to the increase of the effective mass of the electrons near the QDs due to the strained GaAs lattice by the GaSb QDs [40, 49]. At higher excitation power densities, the GaSb QDs show a somewhat larger diamagnetic shift. Similar results were also observed in Ref. 4.7. Besides, as shown in the inset, the integrated PL intensity of the WL increases with the magnetic field due to the additional magnetic confinement to the electrons and the holes. However, the intensity of the QD emission decreases with the field. The cause could be that the magnetic confinement also suppresses the hole relaxation from the WL to the QDs as shown in Fig. 4.5, and hence the carrier concentration in the QDs decreases with the magnetic field.
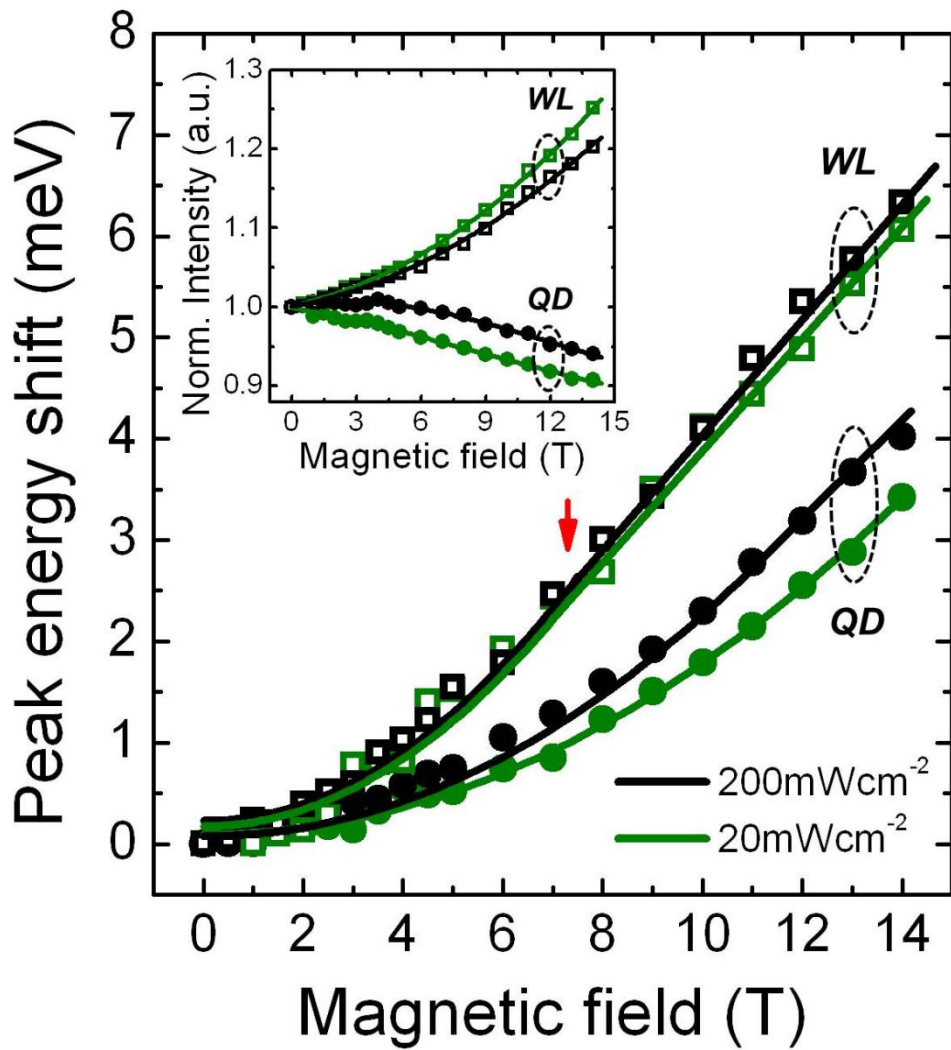
FIG. 4.4 The peak energy shifts of the GaSb QDs and the WL as a function of the magnetic field at different excitation powers in a Faraday configuration. The arrow indicates the low field region where the energy shift has a quadratic dependence on the magnetic field. The inset reveals the integrated PL intensity normalized to that at a zero field of the GaSb QDs and the WL versus the magnetic field.
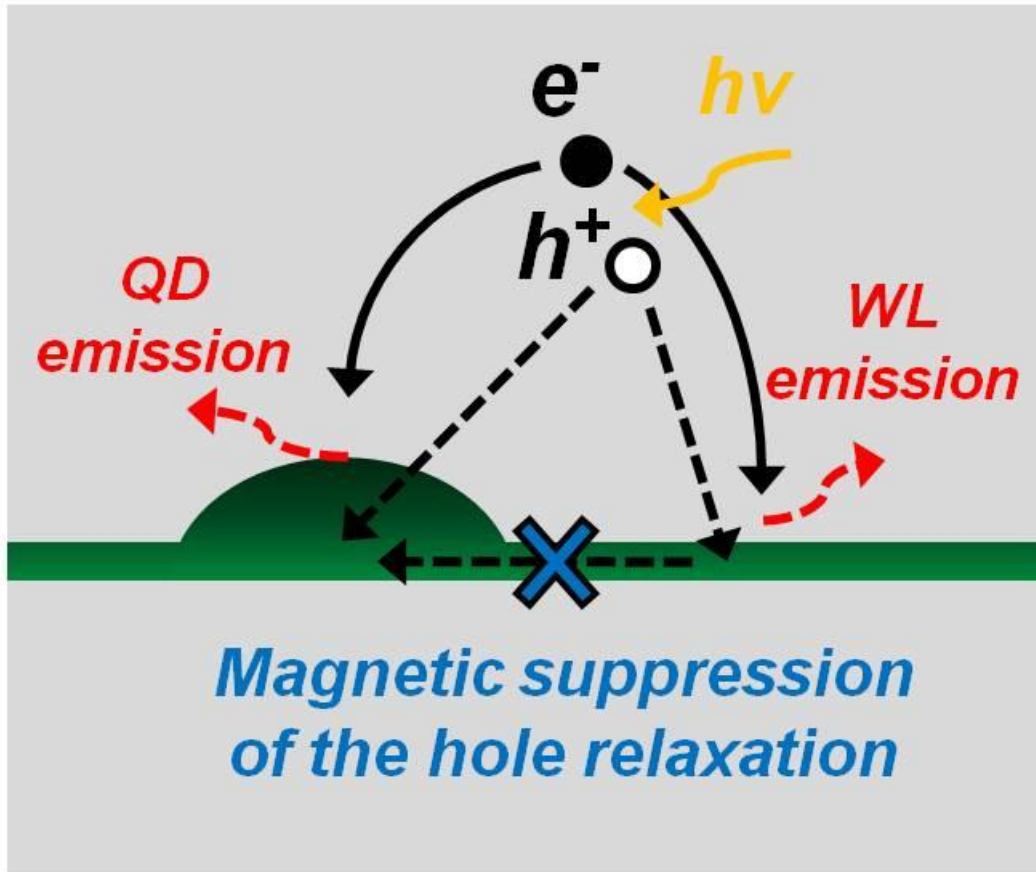
FIG. 4.5 The schematic diagram of carrier relaxation mechanism in GaSb QDs. The magnetic confinement to holes is expected to suppress the hole relaxation from WL to QDs.

4.6 Magneto-PL Measurements in a Voigt Configuration

Figure 4.6 presents the PL spectra of the GaSb QDs measured at a laser pumping power density of 20 mWcm^{-2} in various magnetic fields applied along the in-plane direction (Voigt configuration). An unusual PL red shift accompanied with a rapidly increased intensity is clearly seen. The peak energy shifts of the QDs and the WL measured at different pumping powers are plotted against the magnetic field in Fig. 4.7. Very different behaviors were observed between the energy shifts from the QDs and the WL. The QD luminescence exhibits a rapid red shift at low magnetic fields followed by a slow blue shift. The slow blue shift indicates that the diamagnetic increase of the PL energy overcomes this red shift effect at high

magnetic fields. On the other hand, the observed red shift of the WL is much smaller. This is due to a larger diamagnetic effect caused by a smaller exciton effective mass in the WL. This red shift effect gets stronger at lower pumping powers for both the QD and WL emissions. At the lowest power density of 10 mWcm^{-2}, the maximum of the energy red shift of the QD emission is found to be about -6.5 meV at a magnetic field of 7 Tesla. We marked this value with an arrow in Fig. 4.7 to be the upper limit of this red shift effect. The anomalous effect seems to have an onset point at low magnetic fields. Figure 4.8(a) shows the low field peak energy at different pumping powers. The onset of the red shift appears to be at 1 Tesla and is independent of the pumping power.

Figure 4.8(b) depicts the integrated intensity normalized to that at a zero field of the QD and the WL emissions. The intensities of both emissions increase rapidly at low magnetic fields and slow down at high fields. The intensity increase of the WL PL is larger than that of the QD PL, probably due to the same reason as that in the Faraday configuration, i.e. the suppression of the hole relaxation from the WL to the QDs by the magnetic field. Similar to the PL red shift effect, this intensity enhancement is stronger at lower pumping powers for both the QD and WL PL. For QDs, the onset point and the upper limit of the rapid intensity increase are estimated to be 1 Tesla and 7 Tesla respectively and marked with arrows in Fig. 4.8(b). Obviously, there is a correlation between the anomalous energy red shift and the intensity enhancement in the presence of a magnetic field applied in the Voigt configuration.
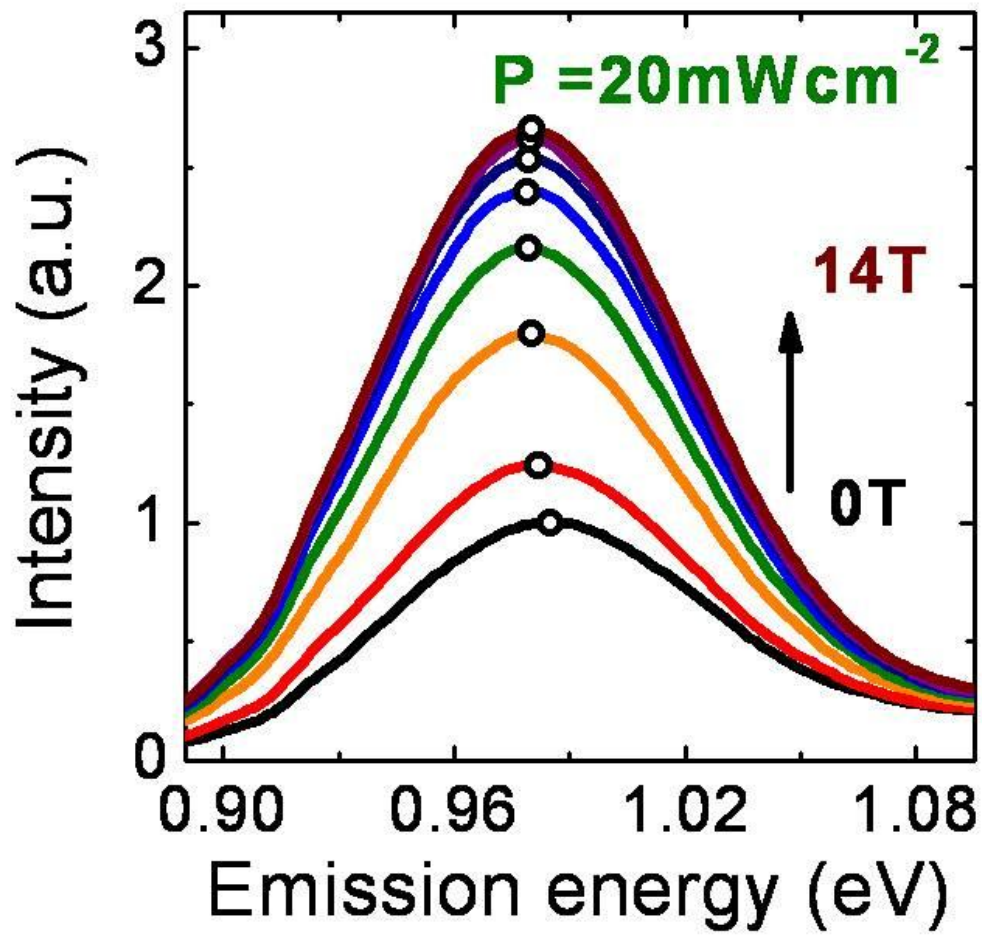
FIG. 4.6 The PL spectra of the GaSb QDs in magnetic fields.
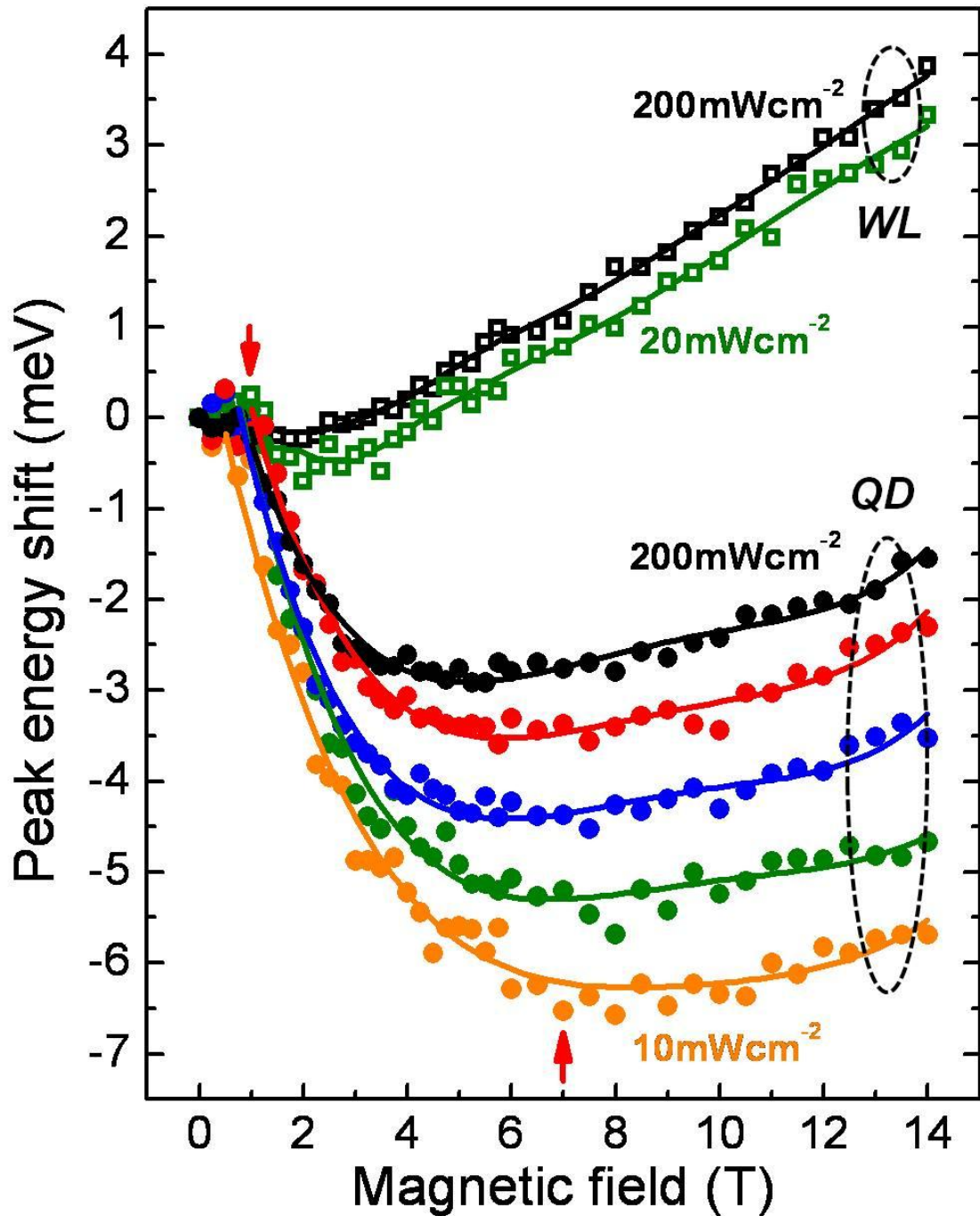
FIG. 4.7 The PL peak energy shifts of the QDs and the WL as a function of the magnetic field at different excitation powers in a Voigt configuration. The excitation power densities are 10, 20, 40, 100, and 200 mWcm[-2]. The arrows indicate the onset point and the upper limits of the energy red shift.
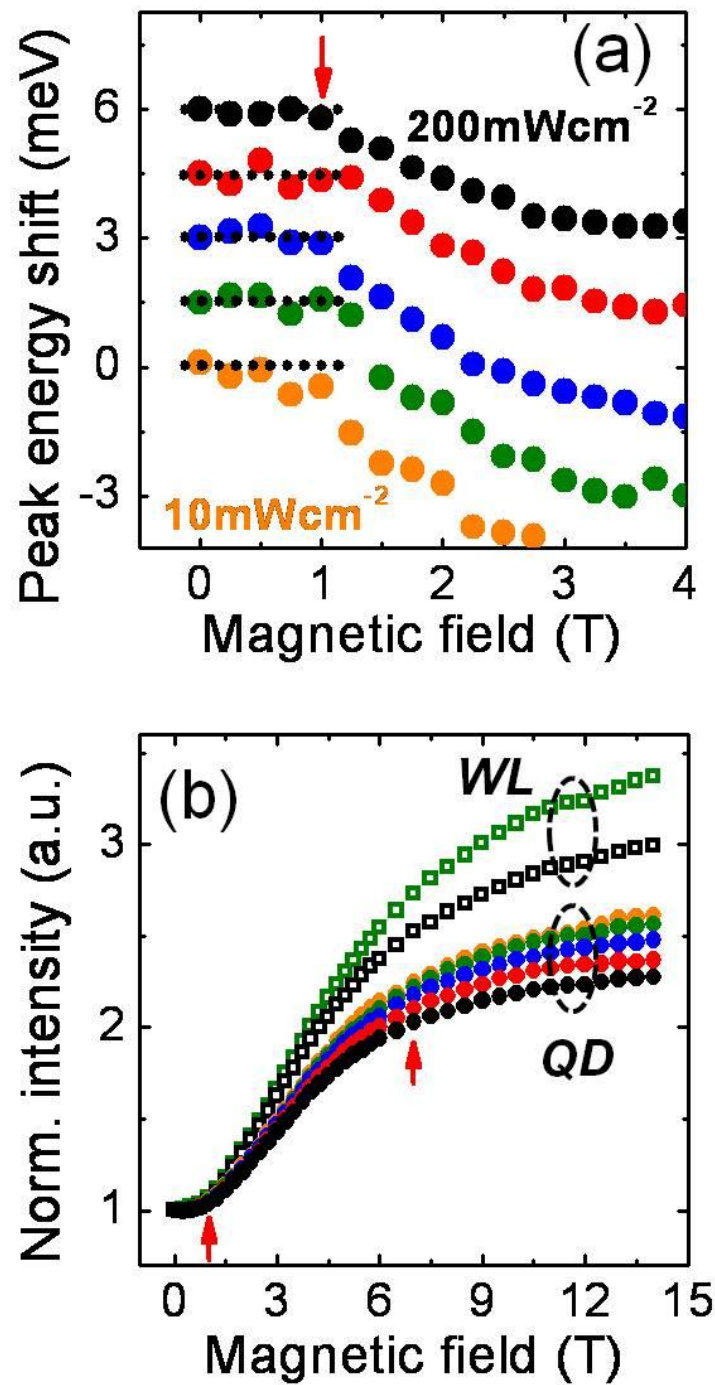
FIG. 4.8 (a) The PL shifts of the QDs versus the magnetic field in the low field region. (b) The integrated PL intensity normalized to that at a zero field of the GaSb QDs and the WL versus the magnetic field. The arrows indicate the onset point and the upper limits of the energy red shift and the rapid intensity increase effects.

4.7 Simulation

In order to interpret the different magneto-optical responses observed in the GaSb QDs in the Faraday and Voigt configurations, a theoretical analysis considering the electron-hole Coulomb interaction in the presence of a magnetic field was carried out. A disk-shaped QD with a layer of WL in a GaAs matrix was used in the calculation. The dot width was 40 nm, the dot height was 8 nm, and the thickness of the WL was 1 nm. The composition of the dot was assumed as $GaAs_{0.3}Sb_{0.7}$ to account for the partial intermixing of As and Sb atoms during growth [50]. The electron effective mass in the GaAs matrix was taken as 0.12 m_0 owing to the strain-induced enhancement [49]. Other parameters used in the calculation were taken from Ref. [16]. The magnetic response was calculated by superimposing a magnetic confining potential to the Hamiltonian. This confining potential energy can be written as

$$V_{B(e,h)} = \frac{e^2 R_{e,h}{}^2 B^2}{8 m_{e,h}},$$

(4.1)

where R is the projection of $\vec{R}$ onto the plane perpendicular to the magnetic field.

The calculated ground-state electron and hole wave functions at a zero magnetic field are illustrated in Fig. 4.9. Holes are found to be localized inside the QD, and electrons are weakly confined in GaAs regions above and below the QD by Coulomb attraction. When the magnetic field is applied, the electron wave function is strongly altered due to the large $V_{B(e)}$ arising from the small effective mass and the large wave function extent. The magnetic force acted on the electrons, which is the derivative of $V_{B(e)}$, is marked in Fig. 4.9. It is found that the magnetic field applied in a Voigt configuration can provide a vertical magnetic confinement to the electrons and hence pushes them to the localized holes.
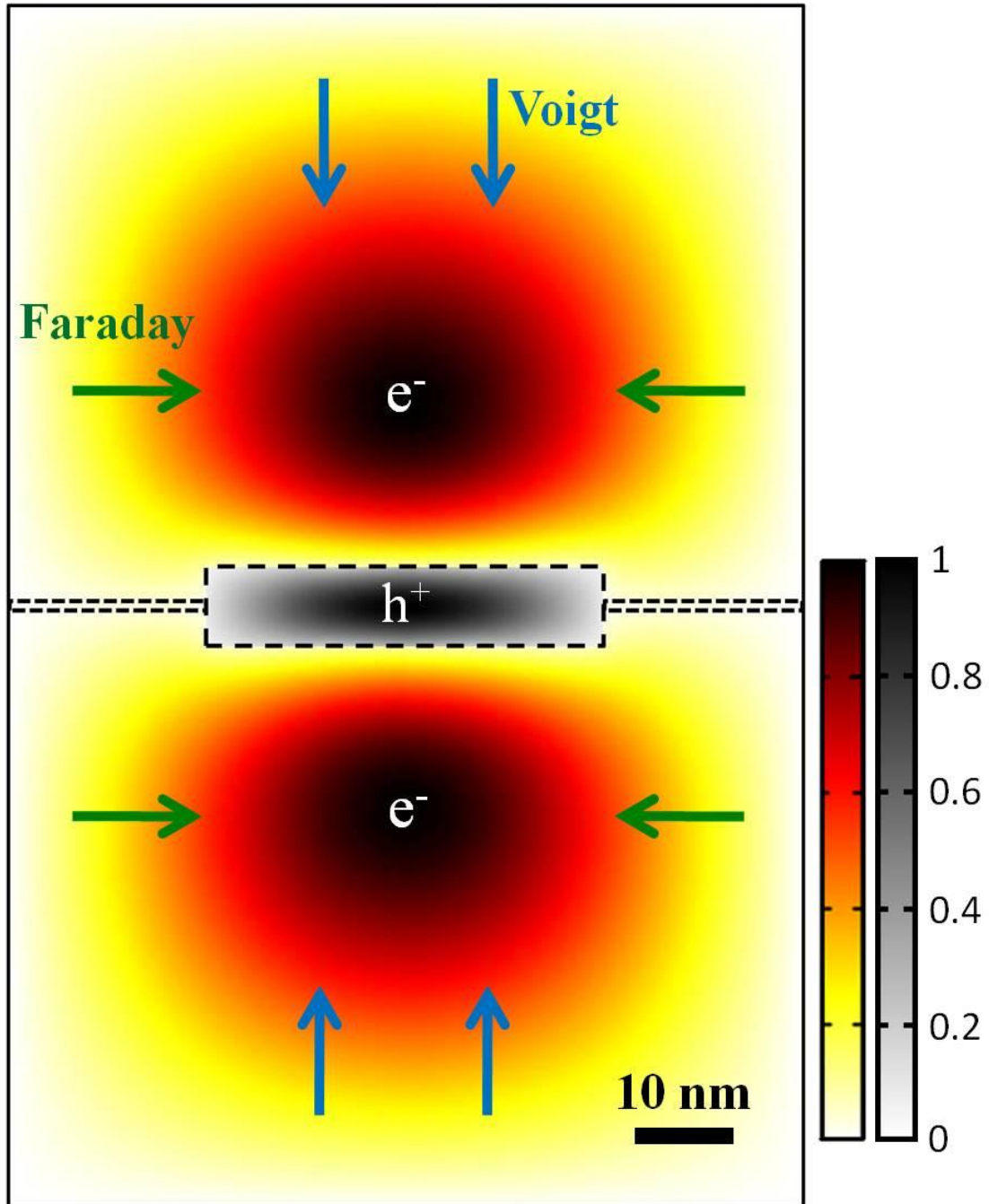
FIG. 4.9. The calculated electron and hole wave functions at zero magnetic field. The QD and the WL are placed in the center of the matrix to simplify the calculation. The green and blue arrows indicate the direction of the magnetic force acted on electrons.

The vertical e-h spatial separation is calculated as $\sqrt{\langle z_e{}^2 \rangle}$ (since the hole is localized in the center of the dot, the origin) and is plotted versus the magnetic field in Fig. 4.10(a). N_h is the hole occupancy of the dot, which determines the magnitude of the Coulomb potential to electrons. At a zero field, the increase of the holes leads to the stronger Coulomb attraction and the resulting decrease of the e-h separation. As the magnetic field is applied in a Voigt configuration, the electron is pushed to the holes by the vertical magnetic confinement, and the vertical e-h separation is hence dramatically reduced. Note that the separation for different N_h is almost the same at the high field of 14 Tesla. This is because the confinement from the magnetic potential for the electrons in high fields is much stronger than that from the Coulomb potential. However, in the Faraday configuration, the reduction of the e-h separation is much weaker.

Figure 4.10(b) presents the exciton binding energy against the magnetic field. The exciton energy is the Coulomb energy between an electron and a hole. However, the binding energy change of the exciton in a Voigt configuration is smaller than 2 meV even at 14 Tesla. Moreover, the difference between the binding energy in a Faraday configuration and that in a Voigt configuration is smaller than 1.2 meV at 14 Tesla. The increase of the binding energy in the magnetic field is much smaller than the observed red shift of -6.5 meV in the experimental finding.

The reduction of the e-h separation is expected to enhance the oscillator strength of the radiative e-h recombination, which is proportional to the square of the wave function overlap between electrons and holes. Figure 4.10(c) presents the oscillator strength normalized to that at a zero field as a function of the magnetic field. As the magnetic field is applied in a Faraday configuration, the oscillator strength is found to be slightly increased. On the other hand, as the magnetic field applied in a Voigt configuration is larger than 1 Tesla, the oscillator strength gets considerably enhanced. Now, we turn to the explanation of this anomalous magnetic red shift. The power-dependent PL spectra indicate that the exciton energy has a

strong dependence on the hole concentration. Since the magnetic field applied in the Voigt configuration enhances the radiative e-h recombination, the holes are depleted by the optical transition and the steady-state hole concentration is therefore decreased. The resulting decrease of the exciton energy of the QDs gives rise to the observed magnetic PL red shift. The calculated Coulomb charging energy for ground-state holes is about 9.3 meV (which is of the same order of the experimental data for the GaSb QDs grown by metal-organic chemical vapor deposition (MOCVD) of 13 meV [18]). Therefore, when the average hole number per dot is decreased by about 0.7, the average exciton energy will red shift by 6.5 meV, which is the maximum of the observed red shift. Besides, the calculated oscillator strength enhancement is much stronger for smaller N_h. This is because the higher hole occupancy of the QDs strengthens the Coulomb interaction and therefore weakens the effect of the additional magnetic confinement to electrons. The simulation results agree with the experimental finding shown in the Fig. 4.7 and 4.8(b), where the energy red shift and the PL intensity enhancement get stronger at lower pumping power.
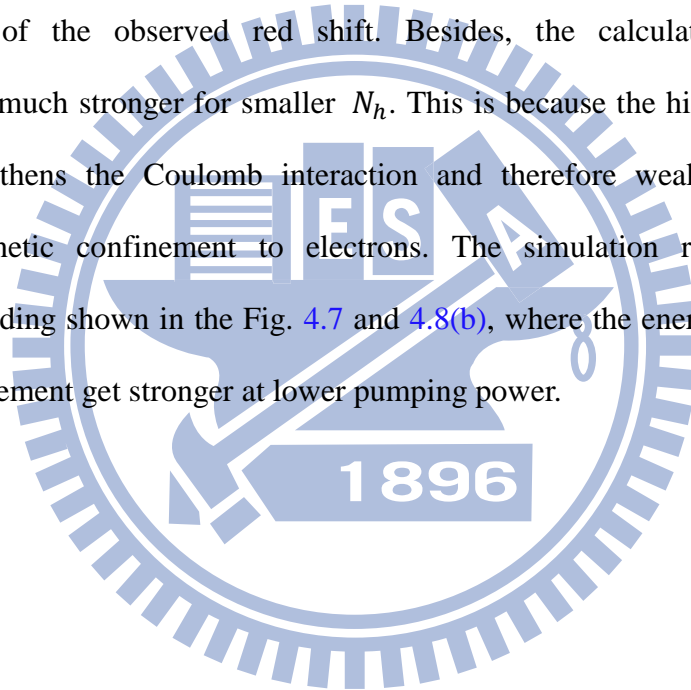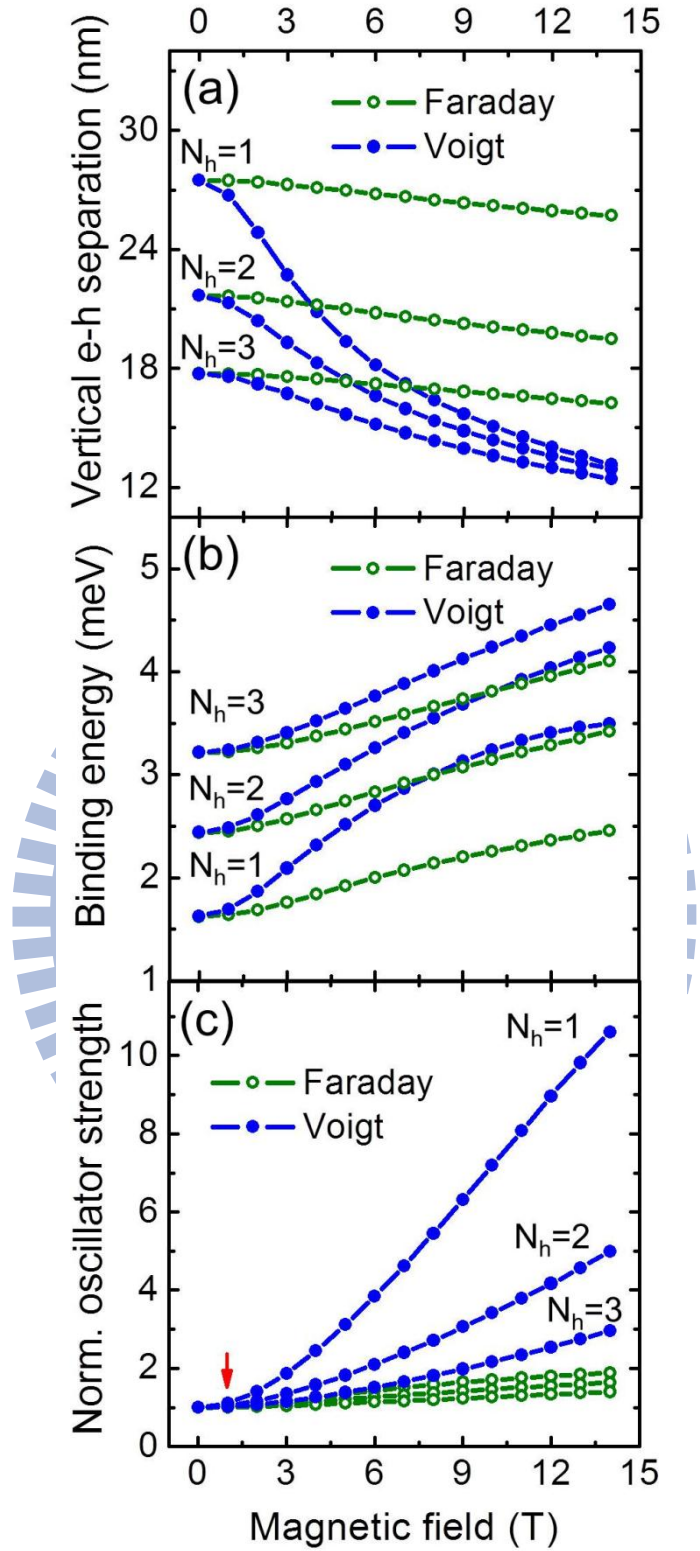
FIG. 4.10. (a) The vertical e-h spatial separation versus the magnetic field for different hole occupancy in the QD. (b) The exciton binding energy versus the magnetic field. (c) The oscillator strength normalized to that at zero field as a function of the magnetic field. The arrow represents the lower limit of the oscillator strength enhancement effect.

4.8 Comparison with type-I InAs QDs

The magneto-photoluminescence measurement in the Voigt configuration has been also performed on type-I InAs QDs, where both the electrons and the holes are confined inside the dots. We compared the emission peak energy shifts of the type-II GaSb QDs and the type-I InAs QDs in magnetic fields measured at the pumping power of 10 mWcm^{-2} as plotted in Fig 4.11(a). It is clearly seen that the InAs QDs show a typical diamagnetic shift. Besides, the integrated intensities normalized to that at a zero field of the GaSb QDs and the InAs QDs are depicted as a function of the field in Fig 4.11(b). The intensity of the InAs QDs is found to be almost constant with the magnetic field. These results are due to the strong confinement for the electrons from the conduction band offset in the InAs QDs, and hence the electron wave function is insensitive to the additional magnetic confinement. As a result, only the type-II QDs exhibit the anomalous red shift and the strong intensity enhancement in the Voigt configuration.
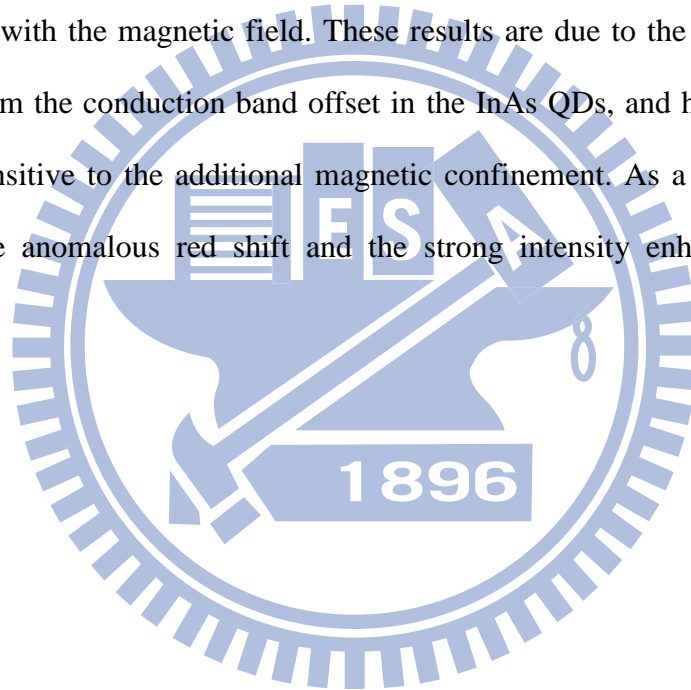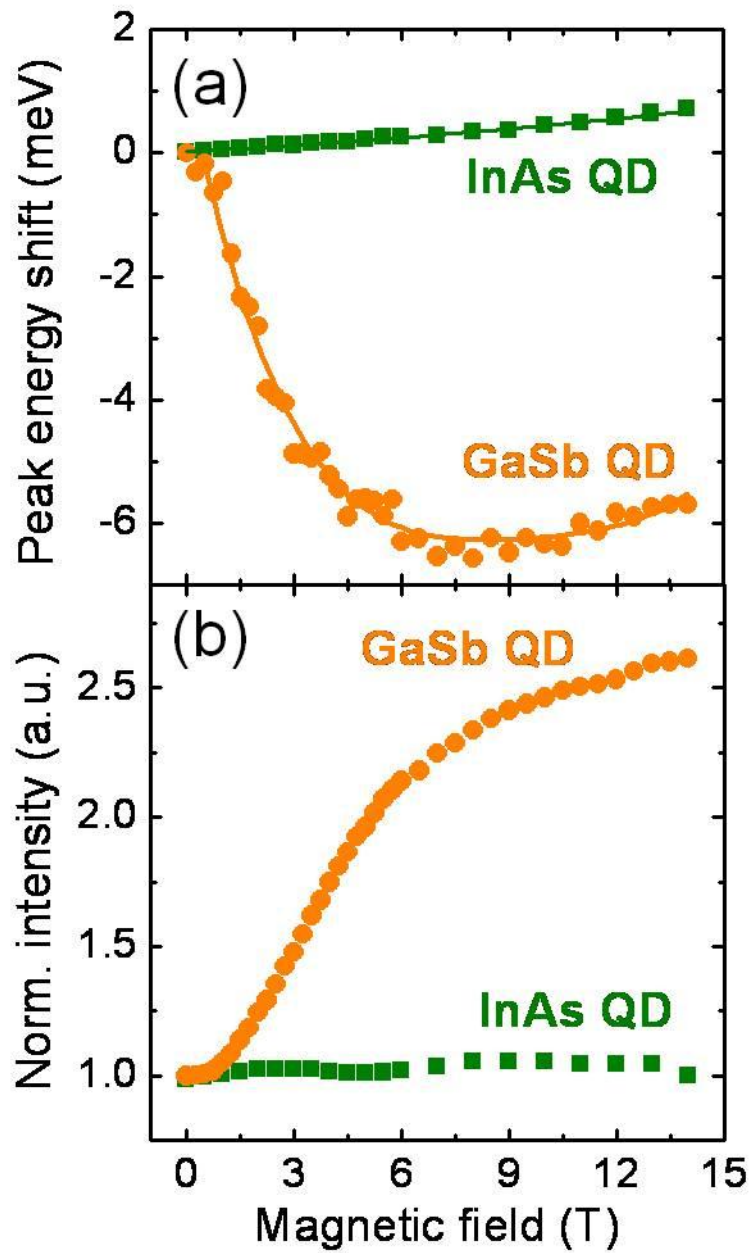
FIG. 4.11. (a) The emission peak energy shifts of the GaSb QDs and the InAs QDs versus the magnetic field. (b) The integrated intensities normalized to that at a zero field of the GaSb QDs and the InAs QDs as a function of the field. The laser pumping power is 10mWcm^{-2}.

4.9 Conclusion

In summary, we have studied the magneto-optical responses of type-II self-assembled GaSb/GaAs QDs in both Faraday and Voigt configurations. When the magnetic field is applied in a Faraday configuration, a typical diamagnetic response is observed. However, when the field is in a Voigt configuration, the QDs exhibit an anomalous magnetic red shift (with a maximum of the red-shift of -6.5 meV) together with a rapid increase of the PL intensity. Besides, both the red shift and the intensity enhancement are stronger at lower excitation power. Based on simulation results, the magnetic field in the Voigt configuration is found to provide an additional vertical confinement and push the weakly-bound electrons to the localized holes. The decrease of the e-h spatial separation leads to the considerable increase of the radiative e-h recombination rate. The resulting decrease of the steady-state hole concentration in the QDs gives rise to the decrease of the exciton energy and the observed anomalous magnetic red shift. Besides, the simulation results also indicate that a higher hole occupancy in the dots induces a stronger Coulomb interaction and therefore weakens the effect of the additional magnetic confinement, which explains the power-dependence of this anomalous red shift. Finally, since the electron wave function is distributed above and below the QD, the electron wave function is not ring-like. This eliminates the probability of the observation of the Aharonov-Bohm oscillation.

Chapter 5

Delocalization of Tensily-Strained GaAs Quantum Dots in GaSb Matrix

In this chapter, we report the fabrication and optical properties of type-II tensily-strained GaAs self-assembled quantum dots grown on GaSb substrate by molecular beam epitaxy. By depositing different GaAs amount, the dot sizes and the corresponding emission energies were varied. The magneto-optical response of the quantum dots with different sizes is investigated in magnetic fields up to 14 T. We analyzed the carrier wave function extent of different dots using the diamagnetic shift results. It was found that, with the increase of the energy (the reduction of the dot size), the diamagnetic coefficient first rises quickly and then saturates at around 21 $\mu eV/T^2$. Based on a simple calculation model, this unusual tendency is attributed to that the electrons gradually spill out of the quantum dot to the wetting layer as the dots get smaller. This delocalization effect is enhanced in this material system due to the tensile strain relaxation within the dots, which raises the conduction band edge over that in the wetting layer.

5.1 Introduction

Type-II self-assembled quantum dots (SAQDs) have attracted considerable interest for the application of carrier storage [18], spin storage device [19], and the exhibition of optical Aharonov-Bohm effect in magnetic fields [7, 8] owing to the spatial separation between the electrons and holes. To date, most SAQD structures are fabricated by the natural compressive strain due to the lattice mismatch between different materials, such as InAs/GaAs, GaSb/GaAs, and InP/InGaP QDs. Recently, the tensily-strained GaAs/GaSb type-II heterostructure with GaAs dots in GaSb matrix has been reported. Since the lattice constant of

the GaAs material is smaller than that of GaSb with 7.3% lattice mismatch, the QD formation is driven by the natural tensile strain. The mid-infrared optical response of the type-II transition is able to be extended to a longer wavelength because of the band gap shrinkage induced by tensile strain [51].

In this work, we studied the magneto-optical properties of GaAs QDs in GaSb matrix. Because of the type-II band alignment, electrons are localized in GaAs QDs while holes are confined to the GaSb region next to GaAs by the Coulomb interaction. As the size of the QDs is changed, an unusual correlation was found between the diamagnetic coefficient and the emission energy. We attributed this phenomenon to the weak localization of electrons within the small-sized QDs in the tensily-strained system. A theoretical model was proposed and the calculated results agree very well with the experimental findings.

5.2 Growth Condition

The GaAs QDs were grown on n+ GaSb (001) substrates by a Veeco Gen-II molecular beam epitaxy (MBE) system with valve cracker sources of Sb_2 and As_2 molecules. Three samples with different amount of deposited GaAs for QD formation were prepared. They were: (1) sample A with 2.0 monolayers (ML) of GaAs, (2) sample B with 2.3 MLs of GaAs, and (3) sample C with 2.5 ML of GaAs. The growth temperature was 500 ℃, the V/III beam equivalent pressure (BEP) ratio for GaAs was 3, and the growth rate was 0.1 ML/s. Note that the growth rate of 0.1 ML/s was taken from that of 0.086 ML/s for GaAs homoepitaxial growth calibrated using RHEED oscillation since the lattice constant of the GaSb substrate is larger than that of the homoepitaxial GaAs substrate used for growth rate calibration. To improve the GaAs QD uniformity, the migration enhanced epitaxy (MEE) technique was used for the QD growth. A 2 seconds growth interruption was used after every 0.5 ML of GaAs was deposited. The GaAs QD layer was embedded in a 100 nm GaSb matrix, which was sandwiched with two 20 nm $Al_{0.3}Ga_{0.7}Sb$ barriers. These barriers were used to confine carriers

and thus improve the PL intensity. Another GaAs QD layer with the same growth condition is grown on the surface of the sample for atomic force microscopy studies.

Other two samples with different V/III BEP ratio are also prepared to study the influence of the As BEP flux on the GaAs QD formation. They are sample D with V/III BEP ratio of 1.5 and sample E with V/III BEP ratio of 7 as shown in table 5.1.
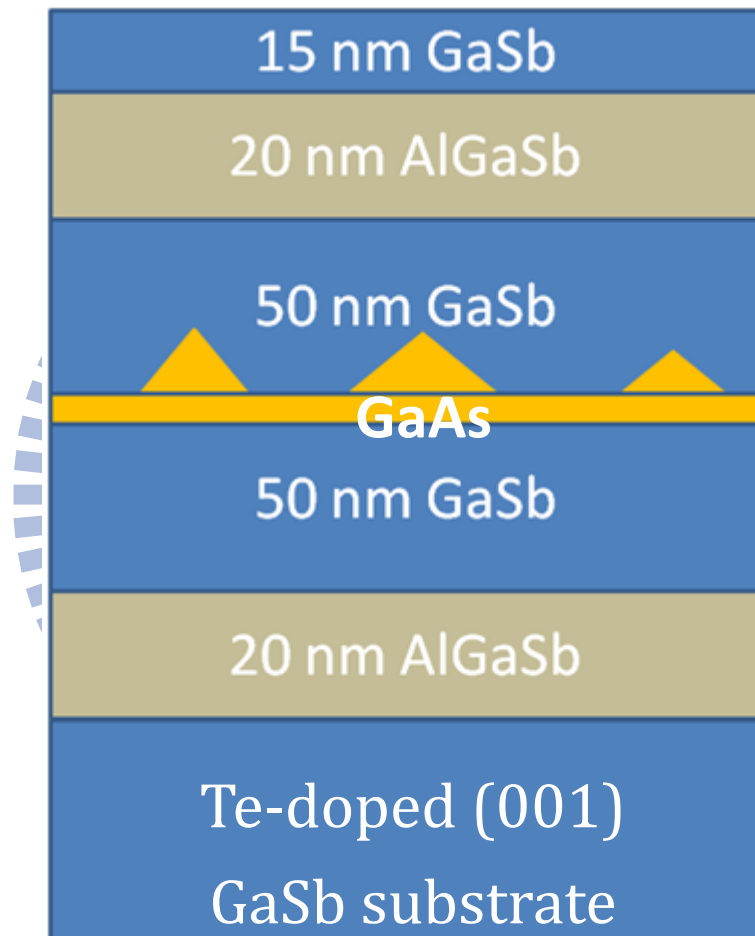
FIG. 5.1. The sample structure of the GaAs/GaSb QDs in our study.

Sample	deposition amount (MLs)	V/III BEP ratio	Growth rate (ML/s)
A	2	3	0.1
B	2.3	3	0.1
C	2.5	3	0.1
D	2	1.5	0.1
E	2.5	7	0.1

Table 5.1 Growth condition of the GaAs layer on GaSb matrix

5.3 Structural Characterization

The atomic force microscope (AFM) is performed for the surface QDs by a Veeco D3100 commercial system in tapping mode. As shown in Fig. 5.2, sample A, B, and C show similar surface topology with a large number of small islands. However, the size of these islands is too small to clearly observe their dimension due to the limitation of the resolution of AFM. Besides, the strong intermixing between As and Sb atoms is expected to change the morphology of the GaAs/GaSb QDs, especially for the surface QDs since there is no capping layer on the surface QD layer after QD growth to inhibit the movement of the adatoms. Therefore, geometry and the dimension of the embedded GaAs QDs are characterized using transmission electron microscope.

In Fig. 5.2 (d), the AFM image of sample D with low V/III BEP ratio of 1.5 reveals no GaAs QD formation. The insufficient As beam flux leads to the incompletion of the GaAs deposition. In Fig. 5.2 (e), the AFM image of sample E with high V/III BEP ratio of 7 shows several sub-micrometer scaled voids. The width of the voids is around 250 nm and the depth is around 15 nm. These voids result from the arsenic-induced etching on the GaSb surface during the GaAs growth [52] and the optical property of the QDs in this sample is hence significantly decreased.
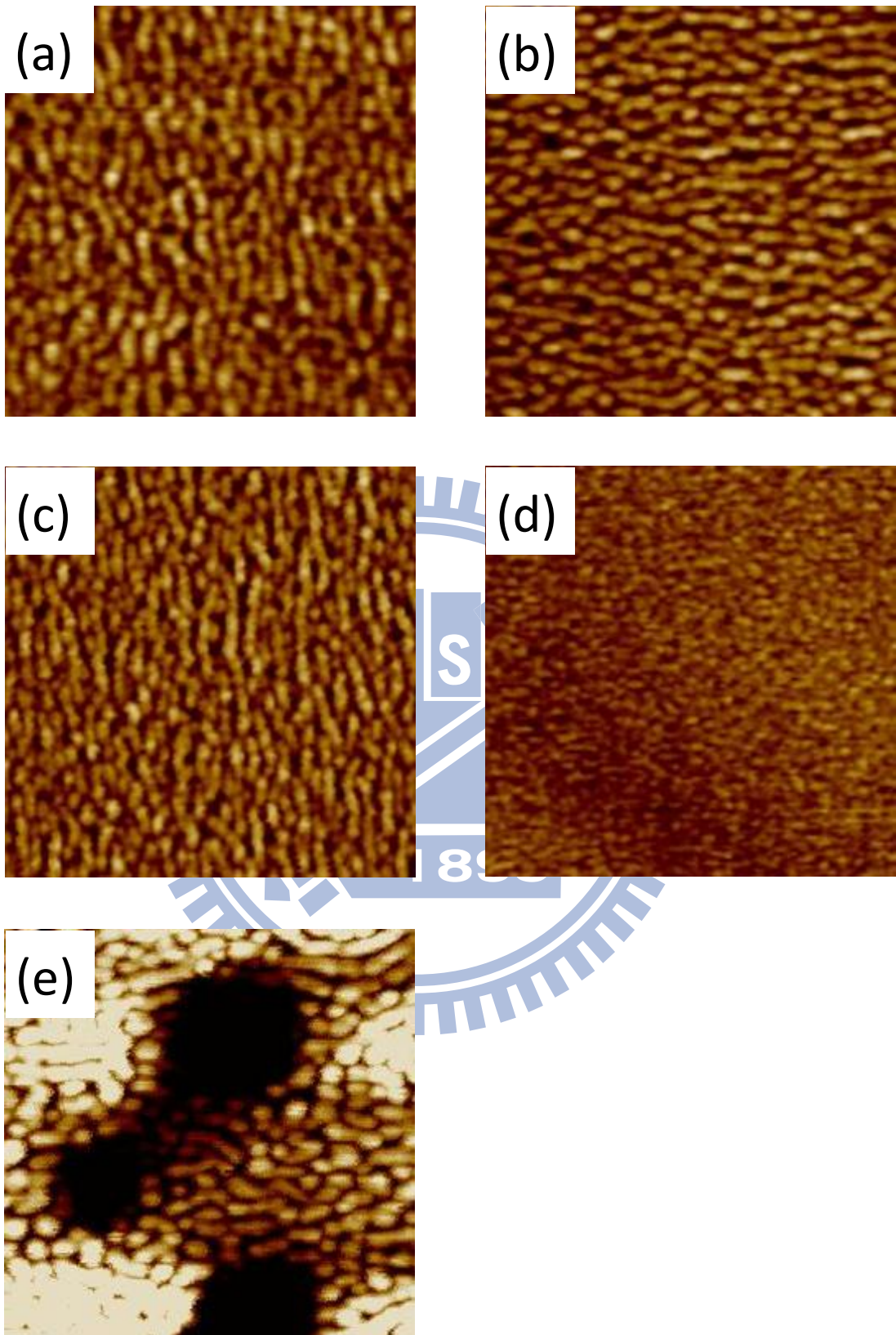
FIG. 5.2. AFM surface images of (a) sample A, (b) sample B, (c) sample C, (d) sample D, and (e) sample E with 1/4 μm square image area.

The embedded GaAs QDs were characterized by a transmission electron microscope (JEOL 2010F TEM) operated at 200 keV. The TEM specimens were prepared using cross-section and plan-view thinning in a Gatan 691 ion mill. The TEM samples were taken from sample A. The cross-sectional and plan-view images are presented in Fig. 5.3(a-b) and 1(c), respectively. The dark areas arising from strain contrast revealed small-sized QDs. From the images, the QDs were estimated to have an aspect ratio of 2.5:1 (width of 9 nm and height of 3.6 nm) and the areal density of $3x10^{11}$ cm^{-2}. The size distribution was shown in the inset of Fig. 5.3(c). The average base width of the dots was 6.7 nm, which is smaller than that of the conventional compressively-strained QDs [53, 54]. Because of the small dot size, the confined electron states were expected to be close to that of the wetting layer (WL).
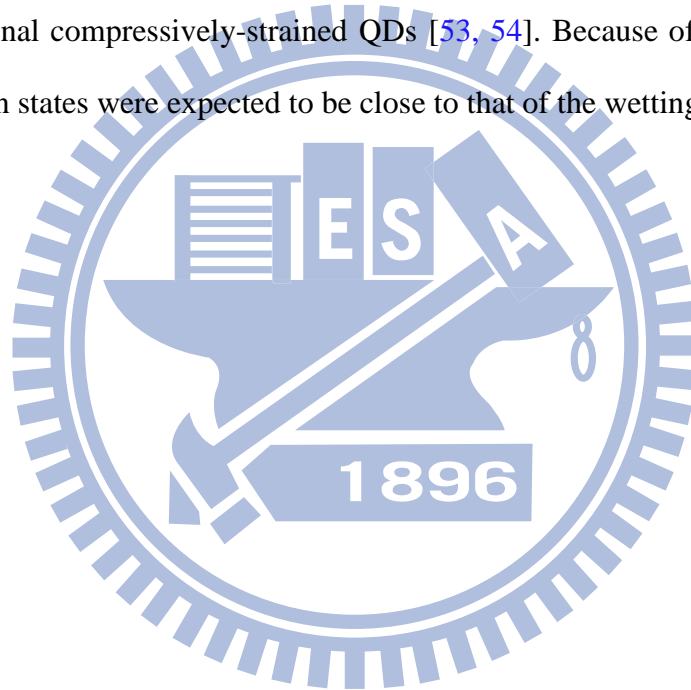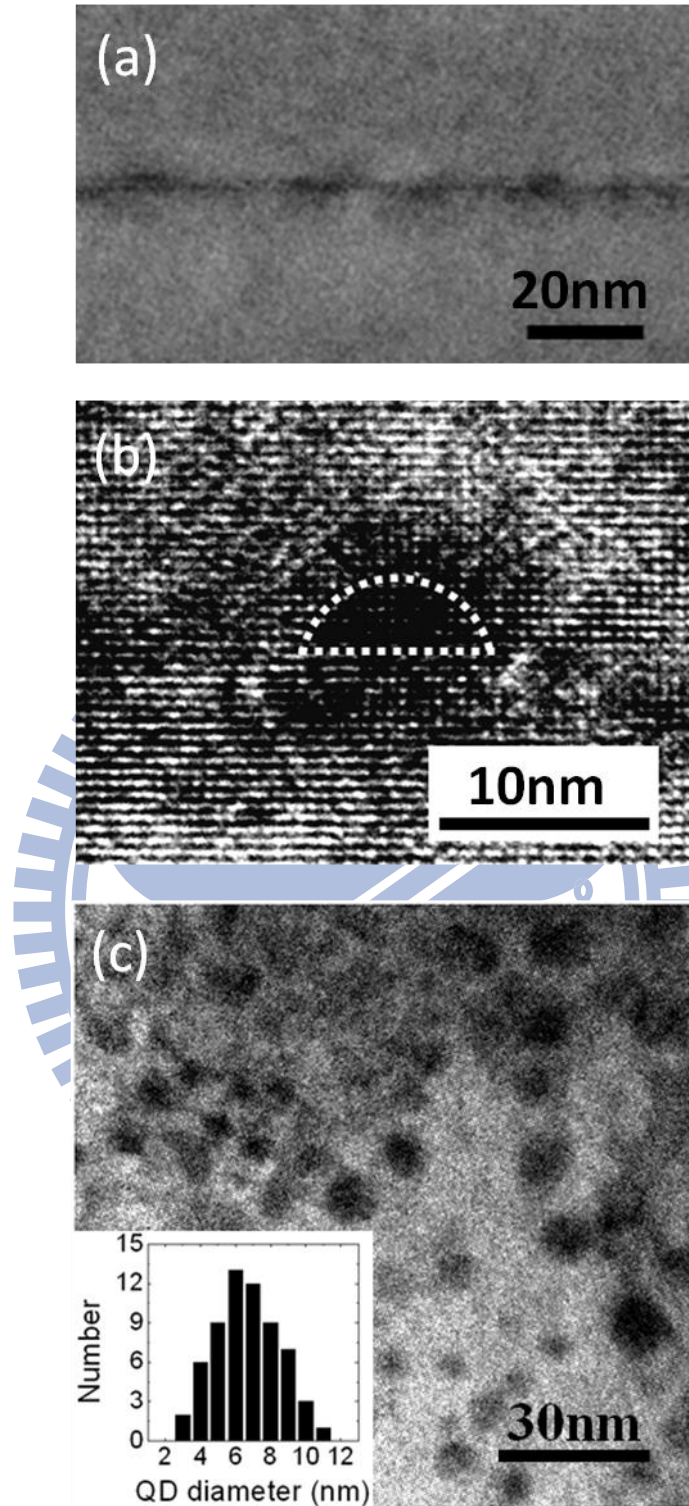
FIG. 5.3. Cross-section (a) TEM and (b) HRTEM images of GaAs QDs in GaSb matrix along the $[010]_{GaSb}$ zone axis. We estimated the average width of QDs as 6.7 nm from (c) the plan-view image taken along $[001]_{GaSb}$ axis. The inset shows the distribution of the QD diameter.

5.4 Conventional Photoluminescence and Excitation Power Dependence

Photoluminescence (PL) measurement was performed at 1.4 K in high magnetic fields up to 14 Tesla in a Faraday configuration. The excitation source was a 532 nm Nd:Yag laser coupled through an optical fiber with a focusing lens. The PL signal was collected with a fiber bundle, dispersed by a 500 mm monochromator, and detected by a wavelength-extended InGaAsSb detector. Further details are described in section 2.3-3 (design B).

Figure 5.4 shows the PL spectra of our samples along with that of the GaSb substrate taken as a reference. A broad emission centered at 0.73 eV is seen for all samples (even for the reference sample, the red dotted line). Since this emission energy is below the GaSb band gap of 0.812 eV, it is hence attributed to the impurities or defects within the GaSb substrate. Sample D and sample E shows only the GaSb substrate emission, which implies the poor optical properties of GaAs QDs in the two samples due to the inappropriate V/III BEP ratio.

The low energy emissions labeled as A1, B1, and C1 are from the central area of these samples and are attributed to the GaAs QDs. The lowest PL peak energy of 0.564 eV (~2.2 μm) is from the largest QDs of sample C1 as a result of the largest amount of deposited GaAs. The PL intensity of C1 is almost half that of A1 due to the more separated electrons and holes for larger type-II dots. Note that the full width at half maximum (FWHM) is 33 meV here, which is smaller than that in Ref. [51] of around 50 meV. The small FWHM indicates that a more uniform QD size distribution, especially in height, is achieved probably by the MEE method.

The dashed lines (labeled as A2 and C2) show the PL from the samples' edge, where the growth temperature is about 20 ℃ lower than that of the central area. The QDs formed in the edge are therefore expected to be smaller. These emission peaks have the asymmetric shape with a low energy band tail, which may be attributed to the QDs with less uniform size distribution due to lower growth temperature. However, in the next section, the magneto-PL measurement which probes the in-plane spatial extent of the carrier wave function reveals that

the electron wave function in these two samples spills out of the GaAs QDs to the WLs. The energy tail has also been found in other Sb-contained or N-contained quantum wells (QWs) and WLs [55-59], and is attributed to the localized states from alloy composition fluctuation, well thickness irregularity, and other crystal imperfections [55, 60].
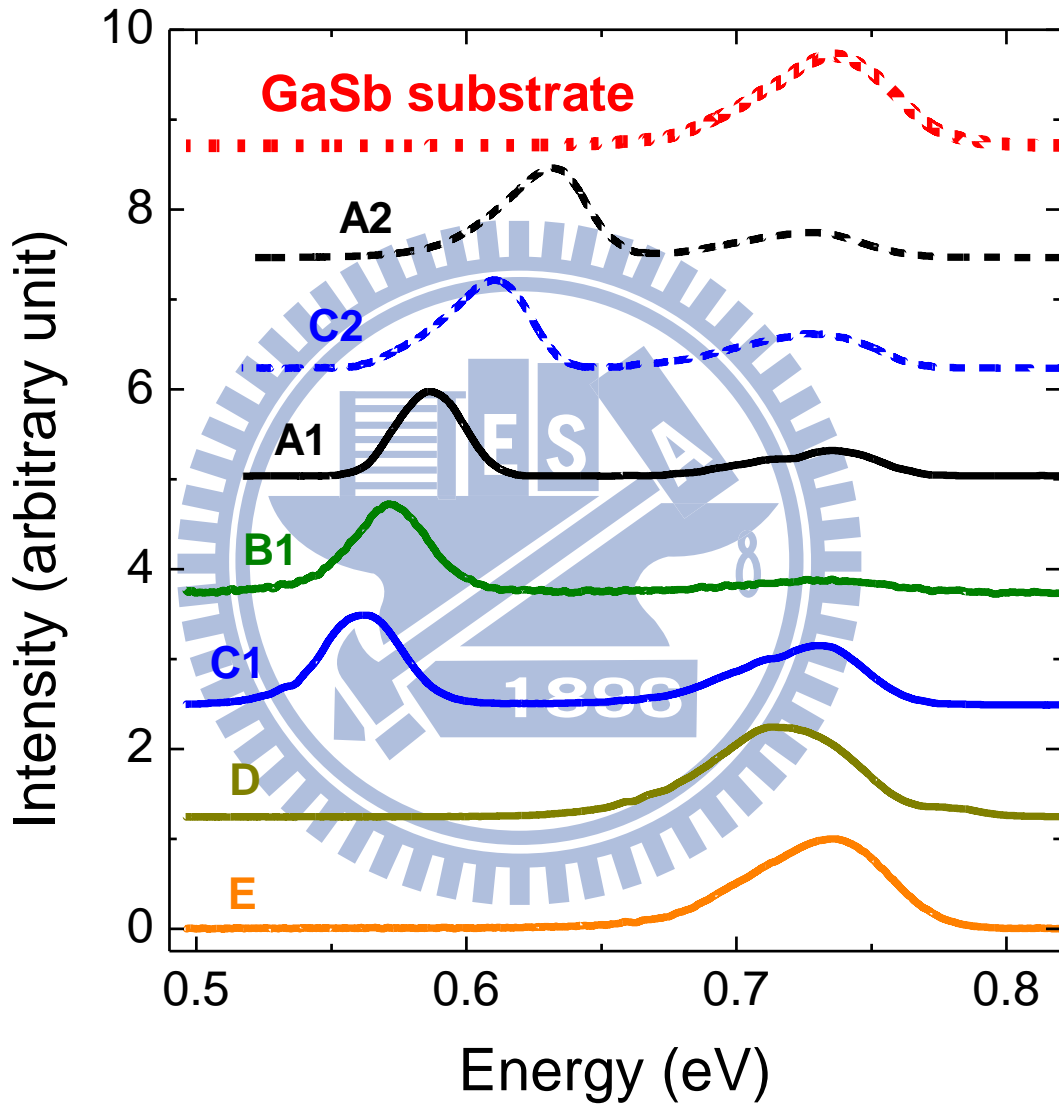
FIG. 5.4. PL spectra of the three samples and the GaSb substrate. The solid lines, A1, B1, and C1, are from the central area of these samples. The dashed lines, A2 and C2, are from the samples' edge.
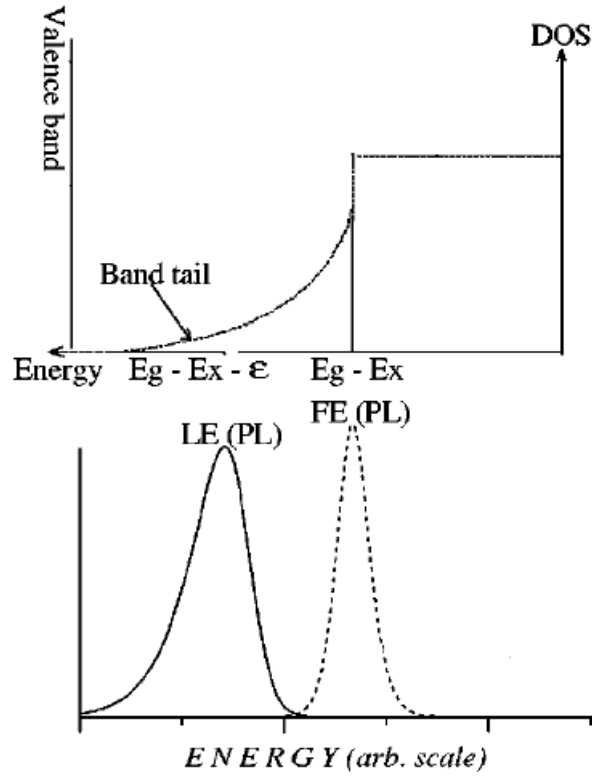
FIG. 5.5. Schematic figure showing free excitons emission ((FE)PL) occurring at Eg-Ex and the band-tail localized excitons emission ((LE)PL) at an energy Eg-Ex-ε. The excitonic density of states (DOS) is also presented [60].

As the excitation power increases, all the emission peaks exhibit energy blue shifts, except that from the GaSb substrate. A representative series of power-dependent PL spectra from sample A1 are illustrated in Fig. 5.6. The blue shift is in proportional to the 1/3 power of excitation power as seen in the inset, which is a clear signature of type-II heterostructure. The spatial separation between electrons and holes in the GaAs/GaSb heterostructures leads to the long carrier recombination time and hence the dramatically increased carrier density with the excitation power. The accumulated electrons confined inside the QDs or WLs fill the electron high energy states and induce a triangular potential well in the GaSb next to GaAs and hence raise the energies of holes. These so-called state filling and band bending effects give rise to the energy blue shifts [47, 61].
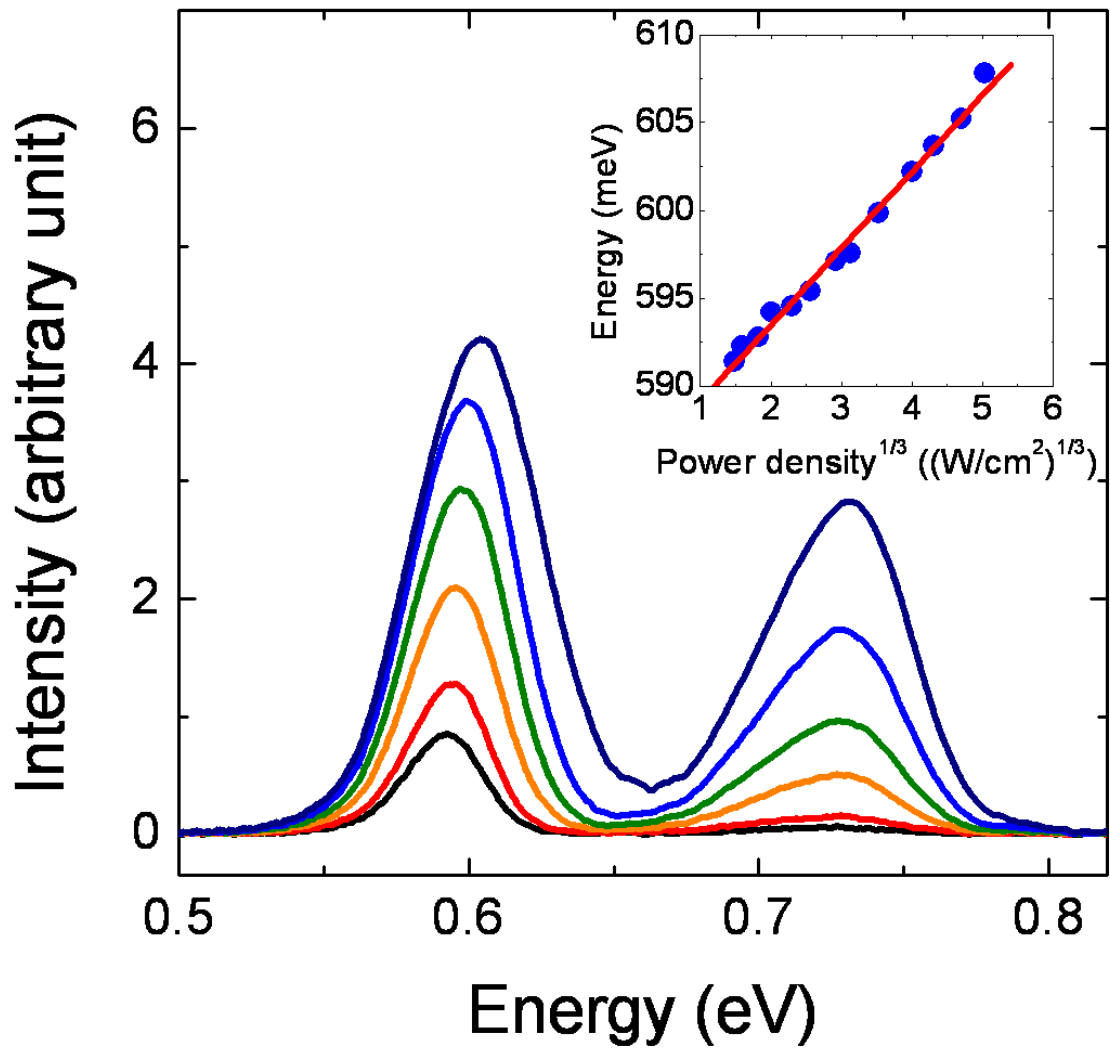
FIG. 5.6. Representative power-dependent PL spectra from A1. The excitation power density is varied from 4W/cm2 to 80W/cm2. The inset shows the emission peak energy of GaAs QDs plotted against the cubic root of the excitation power density.

5.5 Magneto-photoluminescence

The PL spectra of GaAs QDs have been measured as a function of the magnetic field in a Faraday configuration; those from A1 and C1 are shown in Fig. 5.7. The PL intensity is enhanced with the magnetic field (by about 40% at 14 Tesla) due to the additional confinement of carriers from the magnetic field. The blue shift of energy peak, the diamagnetic shift, has a quadratic dependence on the magnetic field. The diamagnetic shift can be well described by the following simple equation when the field is relatively low:

$$\Delta E = \beta B^2 = \frac{e^2 \langle \rho_e \rangle^2 B^2}{8m_e} + \frac{e^2 \langle \rho_h \rangle^2 B^2}{8m_h} \tag{5.1}$$

where β is the diamagnetic coefficient, ρ_e (ρ_h) is the radius of the electron (hole) wave function projected on the plane perpendicular to the magnetic field, m_e (m_h) is the electron (hole) effective mass. The diamagnetic coefficient of the larger QDs from C1 is 7.6 μeV/T². Interestingly, the smaller QDs from A1 show a considerably larger diamagnetic coefficient of 17.3 μeV/T², which is more than double that of the larger QDs. This result suggests that the carrier wave function of the smaller QDs is more extended than that of the larger QDs. This behavior is unexpected for regular sized QDs because the wave functions are generally restricted to a smaller area when the dots get smaller [62]. It should be mentioned that the excitation power is kept very low at 1 W/cm² for the magneto-PL study to reduce the state filling and band bending effects.
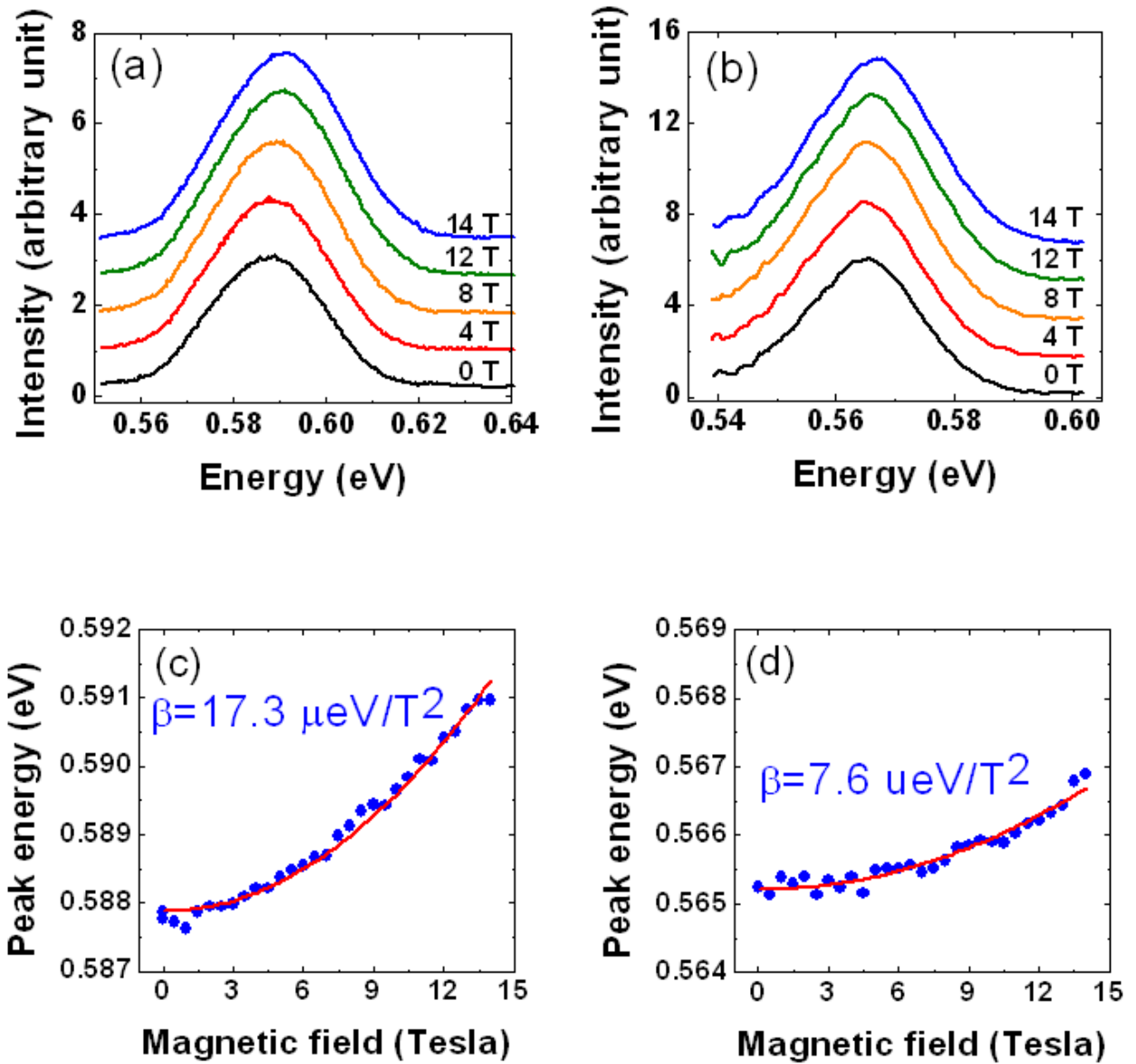
FIG. 5.7. The magneto-PL spectra from (a) A1 and (b) C1. The emission peak energy is fitted to the square of the magnetic field for (c) A1 and (d) C1.

We have performed the measurements on various locations of the three samples to study the dependence of the diamagnetic coefficient as a function of the emission energy. The result is plotted in Fig. 5.8. The solid symbols represent the emission peaks with symmetric shapes which are assigned as QD optical transitions. On the other hand, the open symbols represent the asymmetric emissions with low energy band tails. The diamagnetic coefficient first increases quickly with the emission energy for the QD emissions and then saturates around 21 $\mu eV/T^2$ for those asymmetric emissions. This saturated stable diamagnetic coefficient indicates that the in-plane spatial extent of the carrier wave function is almost independent of the confinement potential. We therefore convincingly attribute those asymmetric emissions as WL-related emissions. The diamagnetic shift of WL in a Faraday configuration depends on the electron-hole separation. For type-I QWs with infinite barriers, the electron-hole separation decreases as the well thickness is reduced due to the enhancement of their Coulomb interaction [63]. However, the spatially separated electron-hole pair of type-II structure causes the lateral separation less sensitive to the well thickness.

Now we turn to the QD emissions. We attribute the increase of the diamagnetic shift with emission energy to two specific properties of the GaAs/GaSb QDs: the tensily-strained system and the small QD dimension. Unlike the common compressively-strained system, where the partial strain-relaxation and the larger height (compared with WL) make the QD energy much lower than that of the WLs, the tensile-strain-relaxation within the GaAs/GaSb QDs substantially raises the band gap energy and compensates the effect of the larger height of the QD. The electron ground state of the QDs hence gets close to or even goes beyond that of the WL, which is fully strained, as the QDs get smaller. As a consequence, the electrons spread out of the QD to the WL, therefore causing an increased diamagnetic coefficient, which eventually saturates at that of the WL.
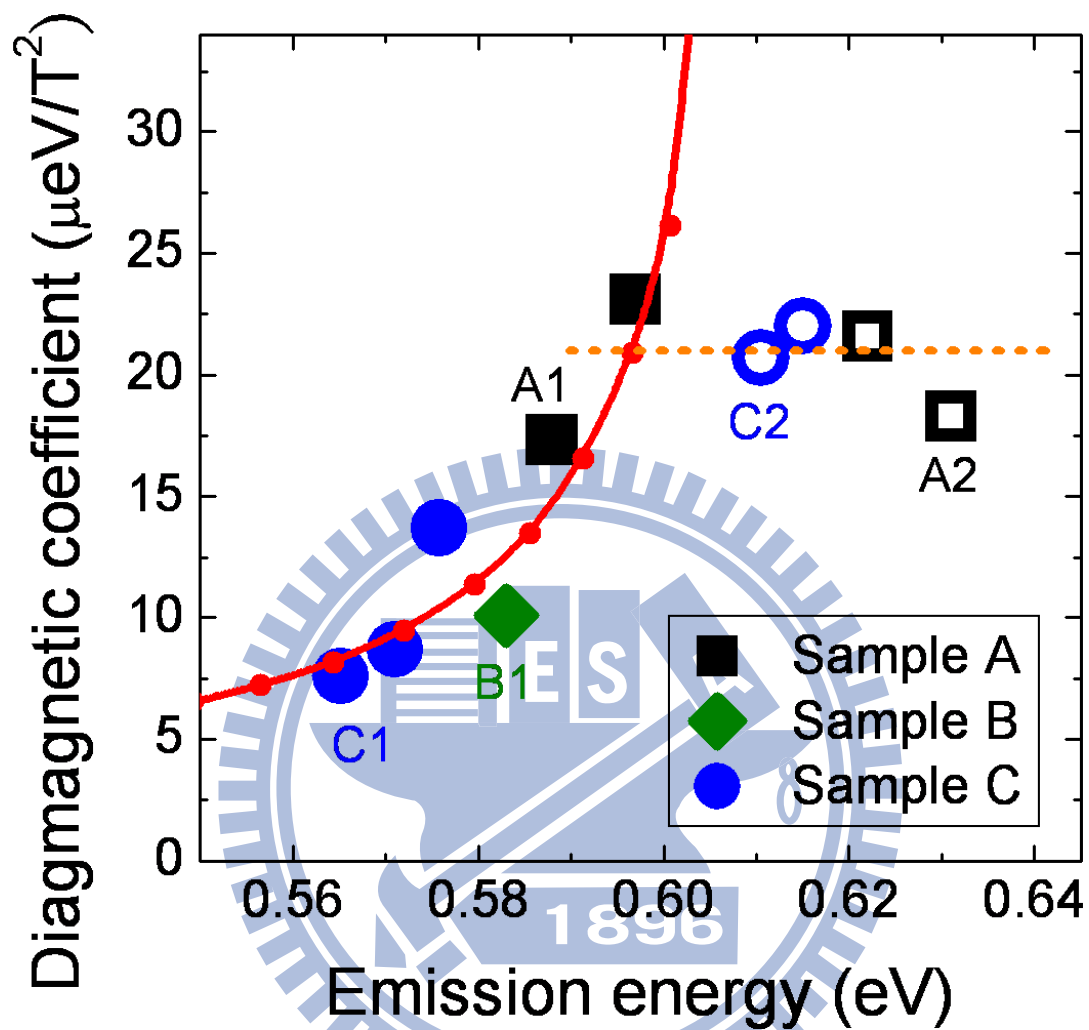
FIG. 5.8. The diamagnetic coefficient against the emission energy of sample A (black squares), sample B (green diamonds), and sample C (blue circles). The solid (open) symbols represent the emissions with symmetric (asymmetric) PL shapes. The calculation results are also plotted here as the red solid line.

5.6 Simulation

We have calculated the electron wave functions using one-band effective mass Hamiltonian. The diameter of the lens-shaped QDs with an aspect ratio of 2.5:1 is varied from 4 nm to 28 nm. A WL of 1 nm thickness is placed below the QD. The composition of the QD, the WL, and the matrix is taken as $GaAs_{0.8}Sb_{0.2}$, $GaAs_{0.45}Sb_{0.55}$, and $GaAs_{0.1}Sb_{0.9}$ to account for partial intermixing of As and Sb atoms during growth [50]. The parameters used in the calculation are taken from ref. [16], and the calculated conduction and valence band edges of the GaAsSb material pseudomorphically grown on GaSb substrate with and without strain effect are shown in Fig. 5.9. Obviously, the tensile strain considerably reduces the band gap and hence extends the emission wavelength.
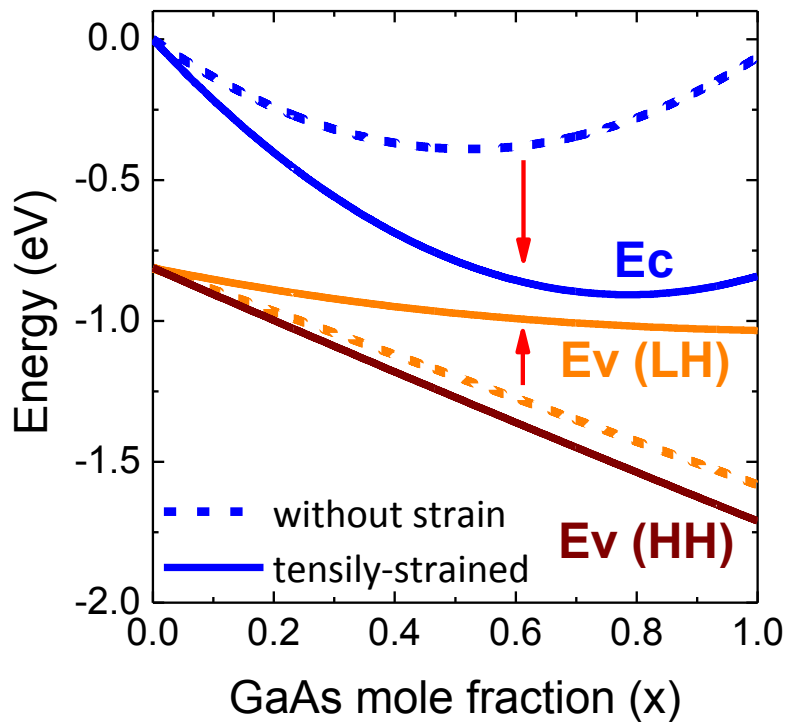
FIG. 5.9. Band edges of $GaAs_xSb_{(1-x)}$ material pseudomorphically grown on GaSb substrate.

Besides, the WL and the pseudomorphically grown matrix are taken to be fully-strained matching the lattice constant of GaSb [51], but the QD is assumed to be 25% strain relaxed. The band diagram of a QD and the adjacent WL under full strain (dotted line) and with the partially relaxed strain in the QD for light-hole state (solid line) and the heavy-hole state (dashed line) is illustrated in Fig. 5.10. Due to the small dot size and large conduction band offset (480 meV), the electrons are confined inside the dot at a high quantization energy. The effective mass is therefore taken as high as 0.08 m_0 owing to the conduction band nonparabolicity [64]. The diamagnetic response can be further calculated by superimposing a magnetic confining potential to the Hamiltonian and then fitted to $\Delta E = \beta B^2$ to find the electron-contributed diamagnetic coefficient.
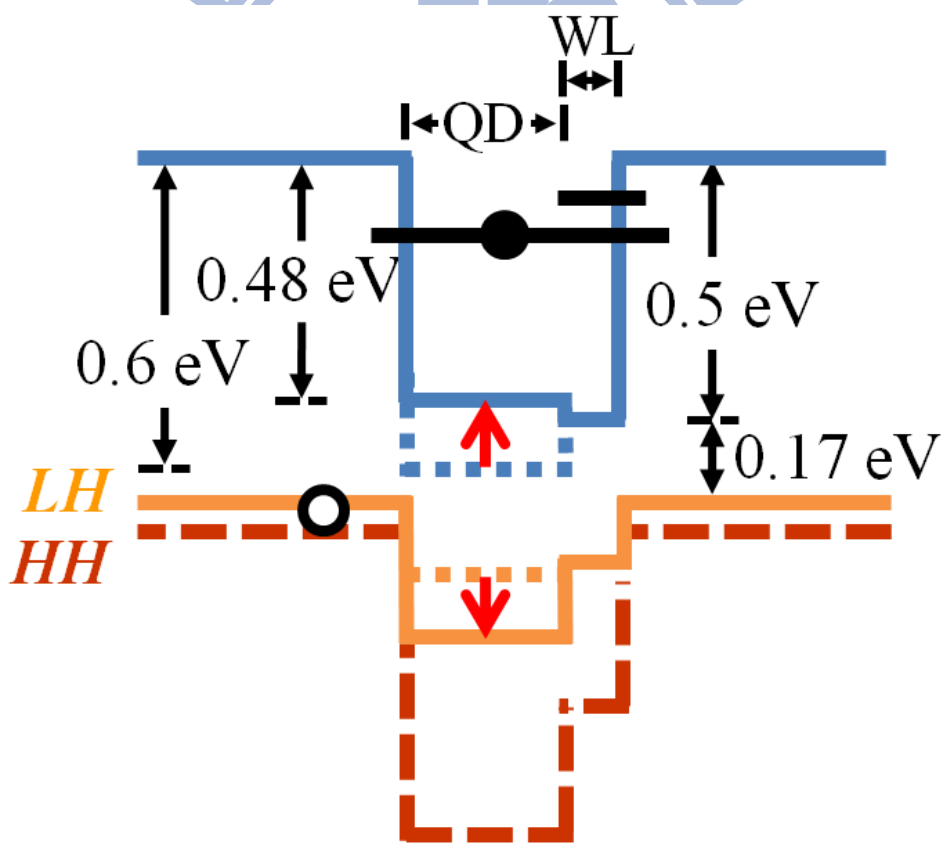
FIG. 5.10. The band diagram of a QD and the adjacent WL under full strain (dotted line) and with the 20% relaxed strain in the QD for the light-hole state (solid line) and for heavy-hole one (dashed line).

Holes are confined to the Ga(As)Sb region near the QD in this type-II system due to the Coulomb attraction to electrons. However, the complicated strain distribution near the QD (with compressive strain in the vicinity of the dot and tensile strain elsewhere) is expected to distort the potential profile for holes and mix the light hole and heavy hole states. To simplify the calculation, we assume that the hole wave function has the same radius as that of the electron wave function, and the hole effective mass is taken to be 0.23 m_0, which is the average of the heavy hole and light hole effective mass of GaSb. Consequently, the hole-contributed diamagnetic coefficient is about 1/3 of the electron-contributed one.

The calculated transition energy and the corresponding diamagnetic coefficient are plotted in Fig. 5.11(a) against the diameter of the QD. When the diameter of the QD is larger than 11.5 nm, the diamagnetic coefficient increases with the QD diameter as expected for regular sized QDs. However, as the QD diameter gets smaller than 11.5 nm, the wave function starts to spread into the WL, the transition energy is approaching to the WL emission energy, and the corresponding diamagnetic response is significantly enhanced. Since the GaAs QDs in GaSb matrix are usually very small [51] and all the dots used in this work are smaller than 11 nm, the rising trend of the diamagnetic coefficient is observed as the QDs get smaller. To compare with the experimental data, the calculated diamagnetic coefficient is plotted (for the small dots) as a function of the transition energy as the red solid lines in Fig. 5.8 and 5.11(b). It agrees very well with the experimental data until the rising diamagnetic coefficient exceeds that of the WL at 21 $\mu eV/T^2$, the orange dashed line. In this situation, the electron-hole Coulomb interaction starts to play an important role, and this simplified model becomes invalid. In Fig. 5.11(b), by defining the QD and WL region as the inset, we calculate the fraction of the electron localized in the QD and plot it as the green line. In the calculation, the electron wave function dramatically spreads out of the QD to the WL as the diamagnetic coefficient gets larger than 21 $\mu eV/T^2$, the experimental value of the WL.
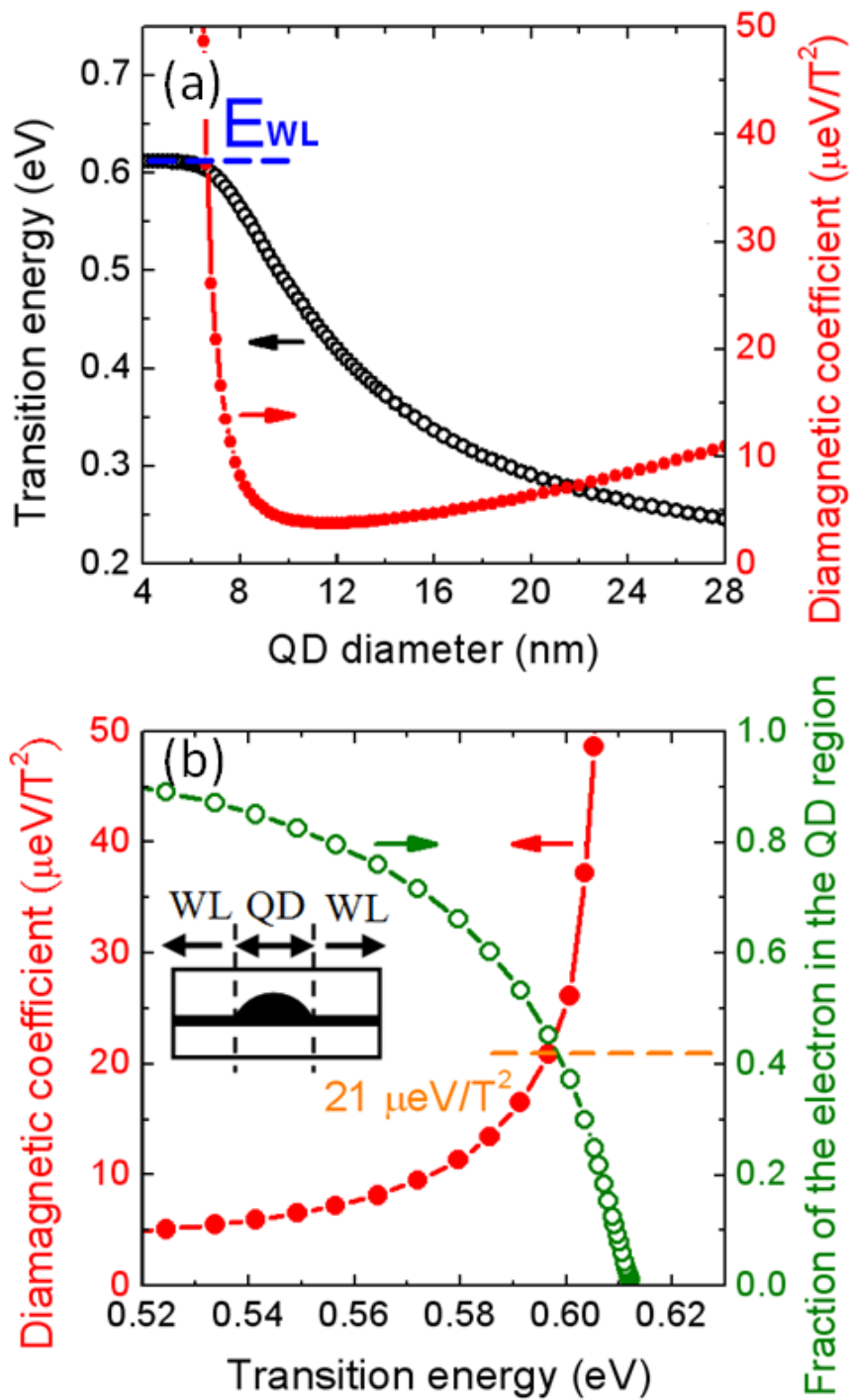
FIG. 5.11. (a) The calculated transition energy and the corresponding diamagnetic coefficient with the diameter of the QD. (b) The diamagnetic coefficient and the fraction of the electron localized in the QD region against the transition energy. The regions of QD and WL are defined as illustrated in the inset.

5.7 Conclusion

In summary, type-II tensily-strained GaAs QDs in GaSb with mid-IR emission up to 2.2 μm were grown by MBE and studied by magneto-PL for the first time. By comparing several samples with different GaAs deposition amount, the diamagnetic coefficient was found to rise quickly from 7.6 μeV/T^2 to a saturated value of around 21 μeV/T^2 with the emission energy. This unusual behavior is due to the spreading of the electron wave function from the QD to the WL as the dots get smaller. A theoretical calculation of the diamagnetic shift in this type-II QD system considering the strain effect is performed and the results agree with the experimental finding.
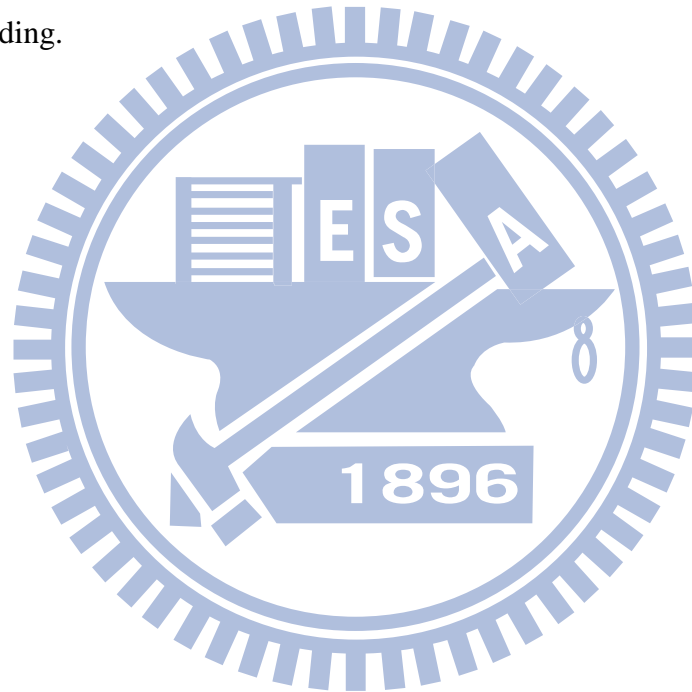
Chapter 6

Aharonov-Bohm Oscillation of GaSb/GaAs QDs with Vertical Confinement

In this chapter, we report the simulation results of the magnetic response of type-II GaSb/GaAs quantum dots with AlGaAs vertical confinement layers placed above and below the dot. The excitonic Aharonov-Bohm oscillation is clearly observed in the calculation. The period and the amplitude of the oscillation are found to have a strong dependence on the dimension of the dots. Smaller quantum dots with the diameter of 20 nm are found to be suitable to exhibit the optical Aharonov-Bohm effect due to the larger amplitude and the appropriate period of the oscillation. The impact of the dot size on the Aharonov-Bohm effect is studied for the first time.

6.1 Introduction

Aharonov-Bohm (AB) effect is found for the charged particles with ring-like wave function as a purely quantum-mechanical effect showing the important role of the vector potential. The ground-state energy oscillates with the magnetic flux $\emptyset_B = \pi r^2 B$ due to the quantum interference of the ring-like carrier wave function. However, due to the electric neutrality of an exciton, the optical AB effect is not expected to occur unless the electron and the hole are spatially separated in different trajectories as mentioned in chapter 3. Therefore, type-II quantum dot (QD) systems with the spatially separated electron-hole pairs are suitable to exhibit the optical AB oscillation. For type-II GaSb/GaAs (GaAs/GaSb) QDs, the holes (electrons) are localized inside the dot, and the electrons (holes) are weakly bound next to the dot due to the Coulomb attraction as mentioned in chapter 4 and chapter 5. Since the oscillation amplitude is inversely proportional to the effective mass of the carrier surrounding

the QD [65], GaSb/GaAs QDs are chosen to be the material system due to the smaller effective mass of electrons. However, due to the shape of the QDs, where the height is much smaller than the width, electrons are mostly confined in GaAs regions above and below the QDs, and the AB effect is hence eliminated as mentioned in chapter 4.

In this chapter, we model and calculate the GaSb/GaAs QDs sandwiched by two AlGaAs confinement layers above and below the dot. The electrons are found to be pushed to surround the dot and hence possess ring-like wave functions. The excitonic AB oscillation is clearly observed in the calculation. Besides, the smaller base width of the dot is found to leads to the larger amplitude and the longer period of the oscillation. In order to enhance the oscillation amplitude, smaller quantum dots with the diameter of 20 nm are found to be suitable for the exhibition of the AB effect.

6.2 Calculation Model

We built up a three-dimensional finite element model using Hartree approximation to calculate the magnetic response of the excitons confined in the GaSb QDs. A one-band effective mass Hamiltonian considering the Coulomb interaction between the electrons and holes was carried out in the presence of the magnetic field. The simulation was performed on two kinds of QD structures as illustrated in Fig 6.1. In structure A, GaSb QDs were embedded in 100 nm thick GaAs matrix. In structure B, GaSb QDs were sandwiched by two 50 nm thick $Al_{0.3}Ga_{0.7}As$ confinement layers. The $Al_{0.5}Ga_{0.5}As$ layers were used to confine the photo-excited electron-hole pairs in order to increase the optical efficiency of the PL. Since the carriers should be well confined by the $Al_{0.5}Ga_{0.5}As$ layers, the boundaries in the simulation were simply treated with Dirichlet boundary condition on the interfaces between $Al_{0.5}Ga_{0.5}As$ layers and GaAs ($Al_{0.3}Ga_{0.7}As$) layers.

The composition of the dot was assumed as $GaAs_{0.5}Sb_{0.5}$ to account for the partial intermixing of As and Sb atoms. The material parameters used in this calculation were taken

from Ref. [16]. The aspect ratio of the QD, i.e. the diameter to the height, was taken to be 5. The diameter of the dot was varied from 10 nm to 40 nm. The hole occupancy of the dot is assumed to be 1. The magnetic response was calculated by imposing the diamagnetic term $H_D = \frac{e^2 B^2}{8m} \hat{\rho}^2$ and the orbital Zeeman term $H_Z = -\frac{e\hbar B}{2m} \frac{i\partial}{\partial \varphi}$ into the Hamilton.
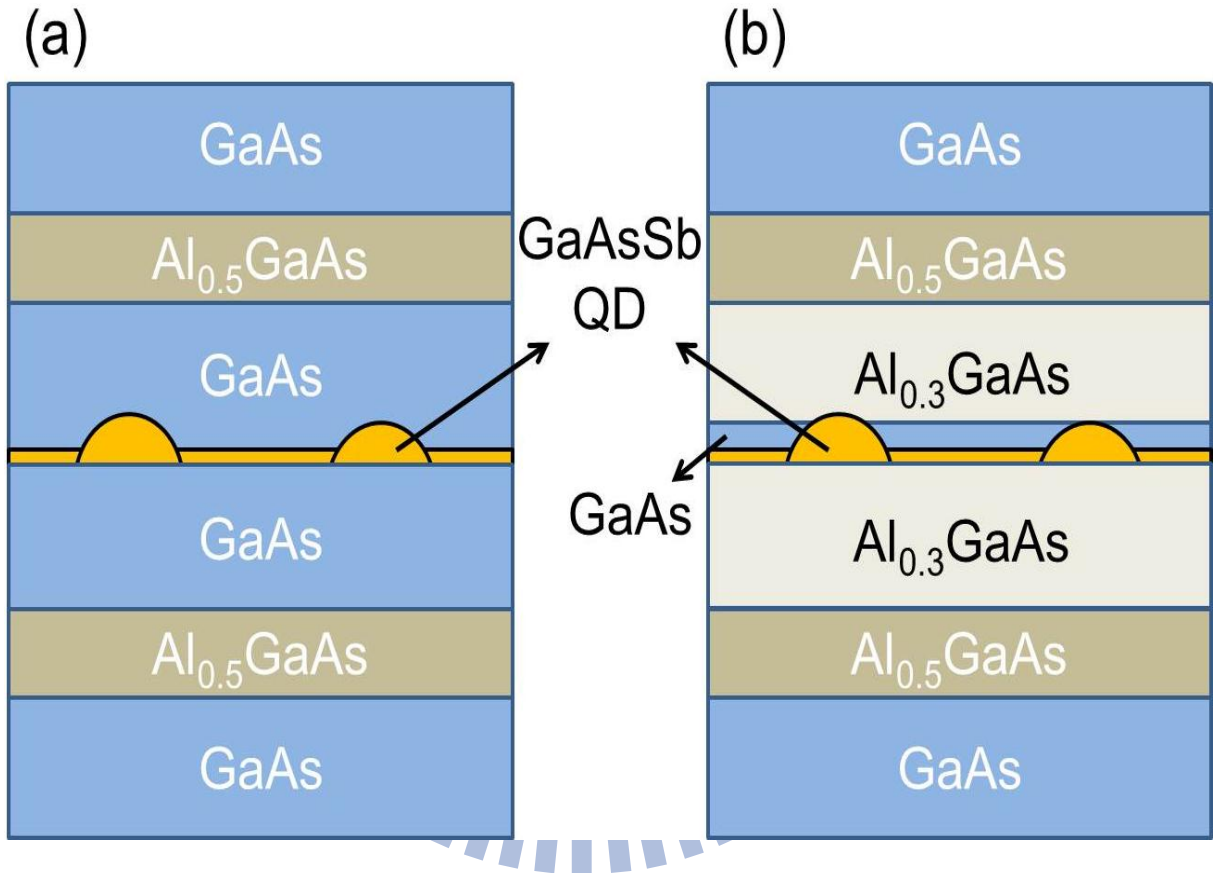
FIG. 6.1. (a) Structure A with GaAsSb QDs embedded in GaAs matrix. (b) Structure B with GaAsSb QDs sandwiched by two $Al_{0.3}Ga_{0.7}As$ confinement layers.

6.3 Additional Vertical Confinement

The calculation was first performed on structure A where the GaAsSb QDs are embedded in 100 nm thick GaAs matrix. The QD is modeled as a nano-scale disk with the diameter of 30 nm width and the height of 6 nm. The calculated ground-state electron wave function at a zero magnetic field is illustrated in Fig. 6.2(a). Electrons are found to be confined in GaAs regions mainly above and below the QD by Coulomb attraction. The calculated electron energy differences from the zero-field ground-state energy are plotted against the applied magnetic field in a Faraday configuration in Fig. 6.2(b). Since the electron wave function is not ring like, the ground-state energy shows no oscillation with the magnetic field. The ground-state and excited-state hole energies are plotted in Fig. 6.2(c). Since the hole is confined inside the dot, the electronic structure of the hole is the typical energy spectrum of the carrier confined in a QD as shown in section 1.3-2. It is found that the magnetic energy shift of electrons is much larger than that of holes. This is because the effective mass of electrons is about one-fifth that of holes and the horizontal electron wave function extent is much larger than that of hole.

FIG. 6.2. (a) The calculated ground-state electron wave function at a zero magnetic field in structure A with the GaAsSb QDs embedded in GaAs. (b) The electron energy differences from the zero-field ground-state energy against the applied magnetic field in a Faraday configuration. (c) The hole energy differences against the field.

In structure B, two $Al_{0.3}Ga_{0.7}As$ vertical confinement layers are inserted above and below the disk-shaped QDs. The electrons are expected to be pushed to surround the dot by the vertical confining potential. The confining potential arises from the conduction band discontinuity between GaAs and $Al_{0.3}Ga_{0.7}As$ and is about 240 meV. The dot height is 6 nm, and the base width is 30 nm. The thickness of the GaAs active layer is 4 nm where the electrons are expected to be confined. As depicted in Fig. 6.3(a) and Fig. 6.3(b), the electrons are localized inside the GaAs layer and possess ring-like wave functions.

The calculated electron energy differences from the zero-field ground-state energy are plotted against the applied magnetic field in a Faraday configuration in Fig. 6.4(a). The ground-state energy is found to oscillate with the magnetic field. At the field of ~0.8 T, the crossings between the state with angular momentum $l = 0$ and the the state with angular momentum $l = -1$ are clearly seen. The calculated ground-state exciton energy versus the magnetic field is in Fig. 6.4(b). The arrows represent the crossings which occur at 0.8 T, 2.4 T, 4.1 T, 5.9 T, and so on. The ratio of the fields is about $1 : 3 : 5 : 7$. This is because the energies of an ideal ring are $E_\ell = \frac{\hbar}{2m_e R^2}\left(\ell - \frac{\Phi}{\Phi_0}\right)^2$, and the crossings should occur at the magnetic flux $\Phi = 0.5\,\Phi_0$, $\Phi = 1.5\,\Phi_0$, $\Phi = 2.5\,\Phi_0$, $\Phi = 3.5\,\Phi_0$, and so on. Note that the calculated amplitude of the oscillation is around 150 µeV. Therefore, the accuracy of the measurement system should be ~15 µeV. In other words, the investigation of the AB oscillation has to be performed using single dot optical spectroscope where the line width of the PL is ~50 µeV. By fitting the PL peaks with Lorentzian functions, the optimum system resolution could be achieved to ~2.5 µeV [6].
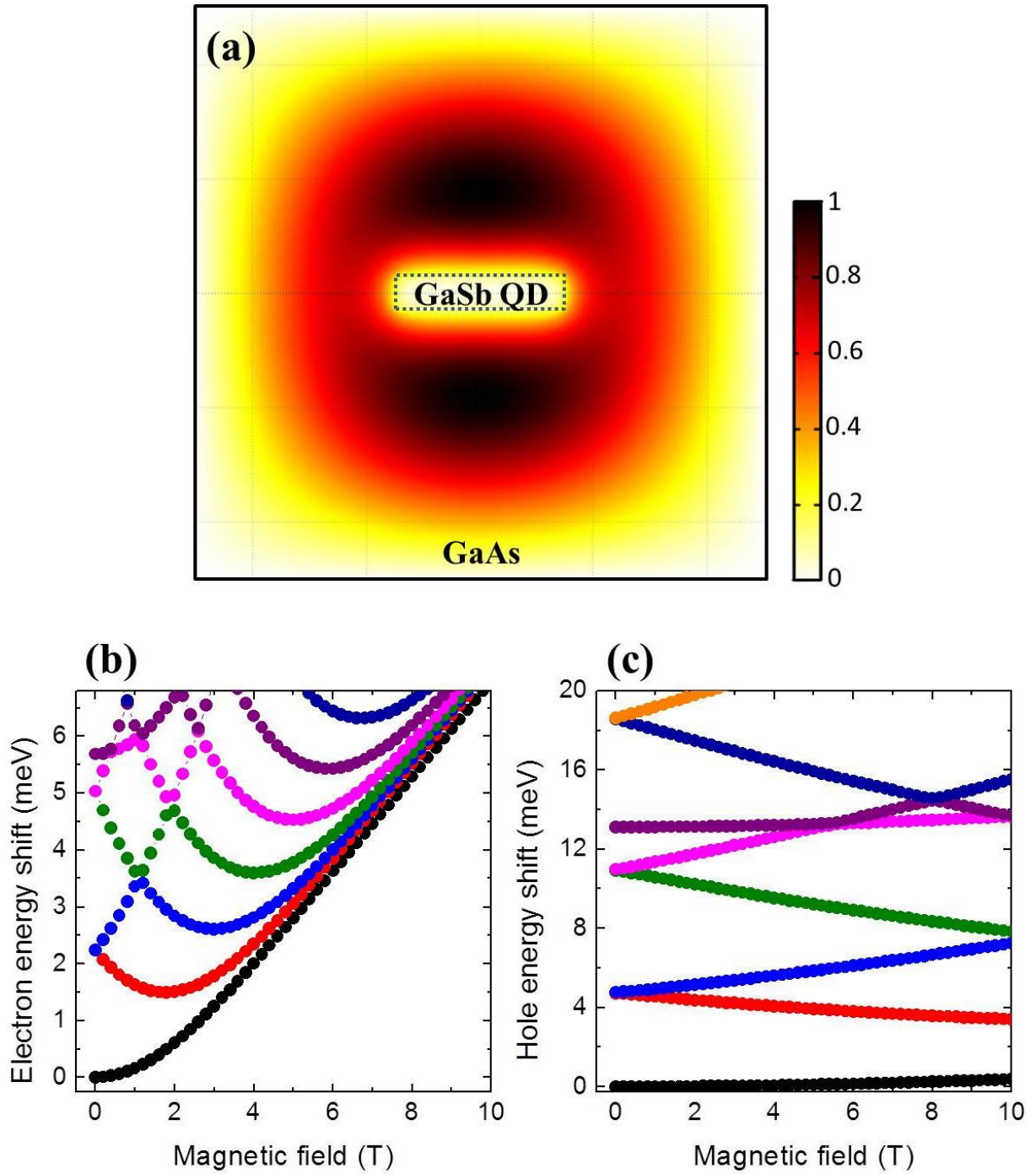
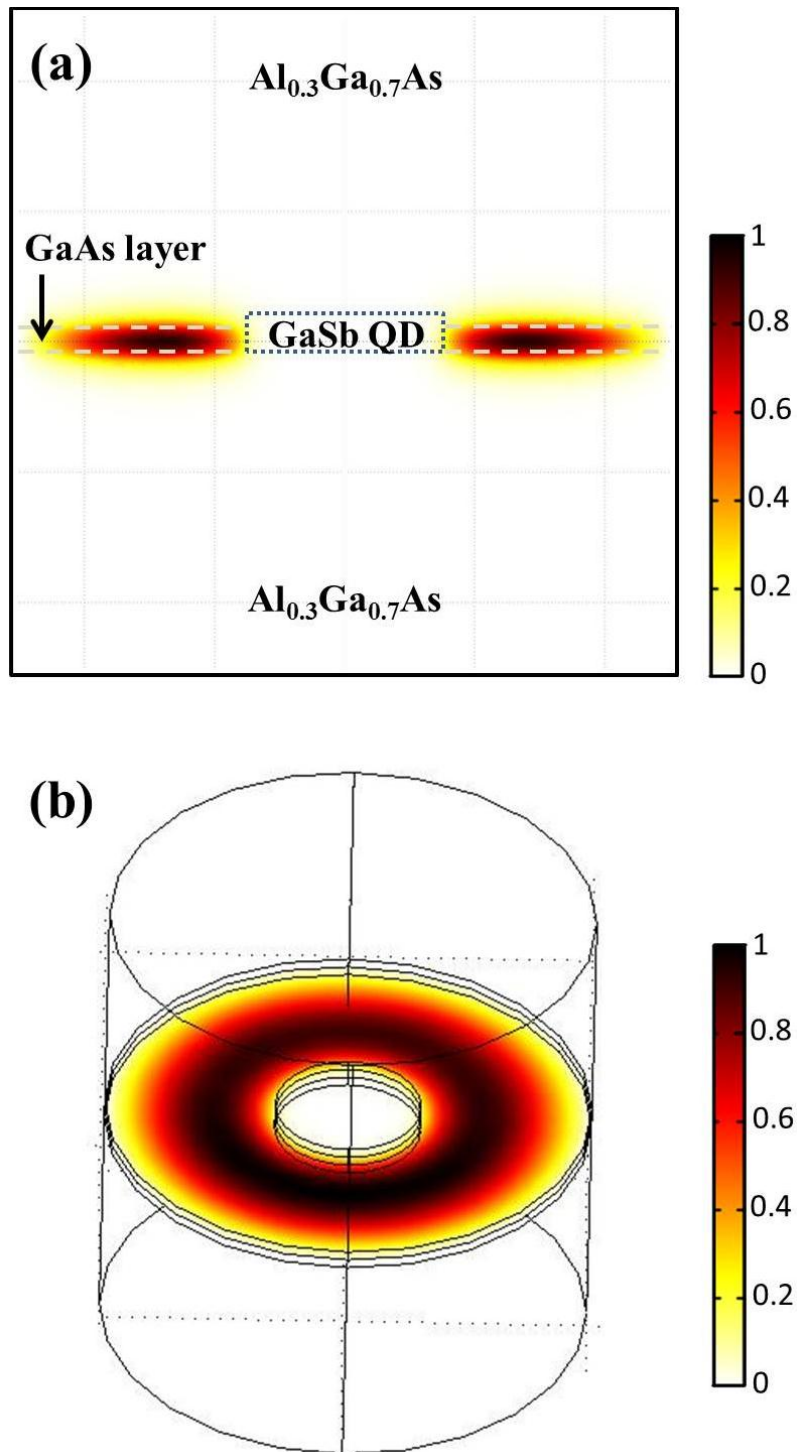FIG. 6.3. The calculated ground-state electron wave function at a zero magnetic field in structure B with the GaAsSb QDs with additional AlGaAs vertical confinement layers.
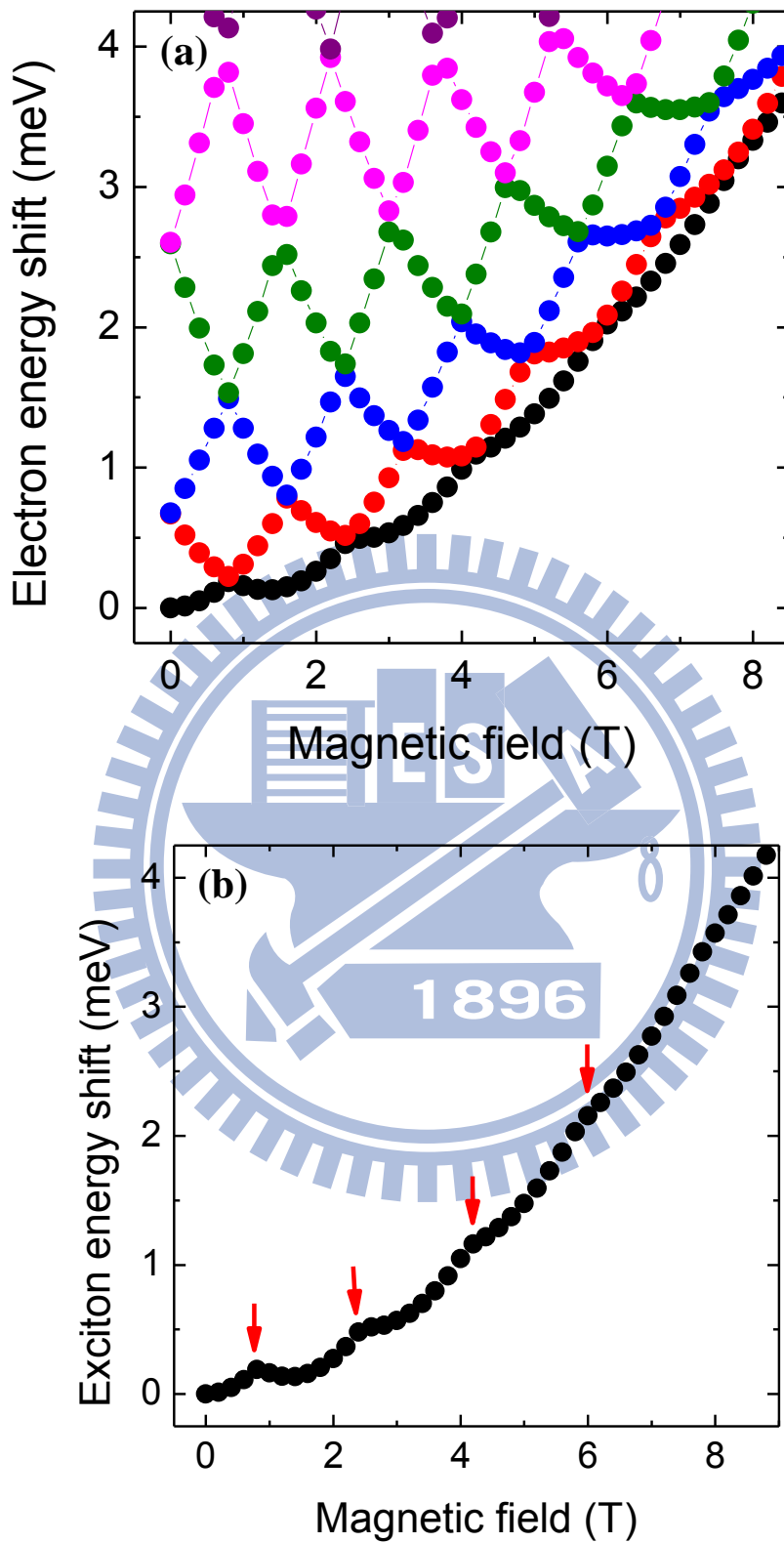
FIG. 6.4. (a) The calculated electron energy differences from the zero-field ground-state energy are plotted against the applied magnetic field in a Faraday configuration. (b) The calculated ground-state exciton energy shift versus the magnetic field.

6.4 The Impact of the Dot Dimension

Based on the calculation of the energies of an ideal ring $E_\ell = \frac{\hbar}{2m_e R^2}\left(\ell - \frac{\Phi}{\Phi_0}\right)^2 = \frac{\hbar}{2m_e R^2}\left(\ell - \frac{e\pi R^2 B}{h}\right)^2$, the amplitude of the AB oscillation is inversely proportional to the carrier effective mass and the area of the carrier wave function. As a result, the smaller effective mass and the smaller wave function extent R are able to generate the larger amplitude. For GaSb/GaAs QDs with vertical confinement, the electrons surround the dot due to Coulomb interaction and hence possess ring-like wave function. For smaller dots, the electron wave function extent is expected to be reduced, which enhances the oscillation amplitude. Moreover, the reduction of the wave function extent also leads to the decrease of the magnetic flux through the ring-shaped wave function. Therefore, the higher magnetic field is the necessity of the energy crossing for the electron wave function with smaller R.

In this section, the impact of the dimension of the QD on the excitonic AB oscillation is investigated. The diameter of the QD is varied from 10 nm to 40 nm. The ground-state exciton energy shifts of the different-sized QDs are plotted against in Fig. 6.5. All of the different-sized QDs clearly reveal energy oscillation of the ground states with the magnetic field. The arrows in the figure indicate the occurrence of the crossing of the energy states with different angular momentum. The largest QD with the diameter of 40 nm shows the shortest oscillation period of ~1.3 T. However, the amplitude of the oscillation is only ~100 meV. For the smallest QD with the diameter of 10 nm, the amplitude is about 350 meV, but the period of ~12 T is too long to observe more than one oscillation in our measurement system. As a result, the QD with the diameter of 20 nm is found to be suitable to exhibit the optical Aharonov-Bohm effect due to the larger amplitude of ~230 meV and the appropriate period of the oscillation of 3.8 T.
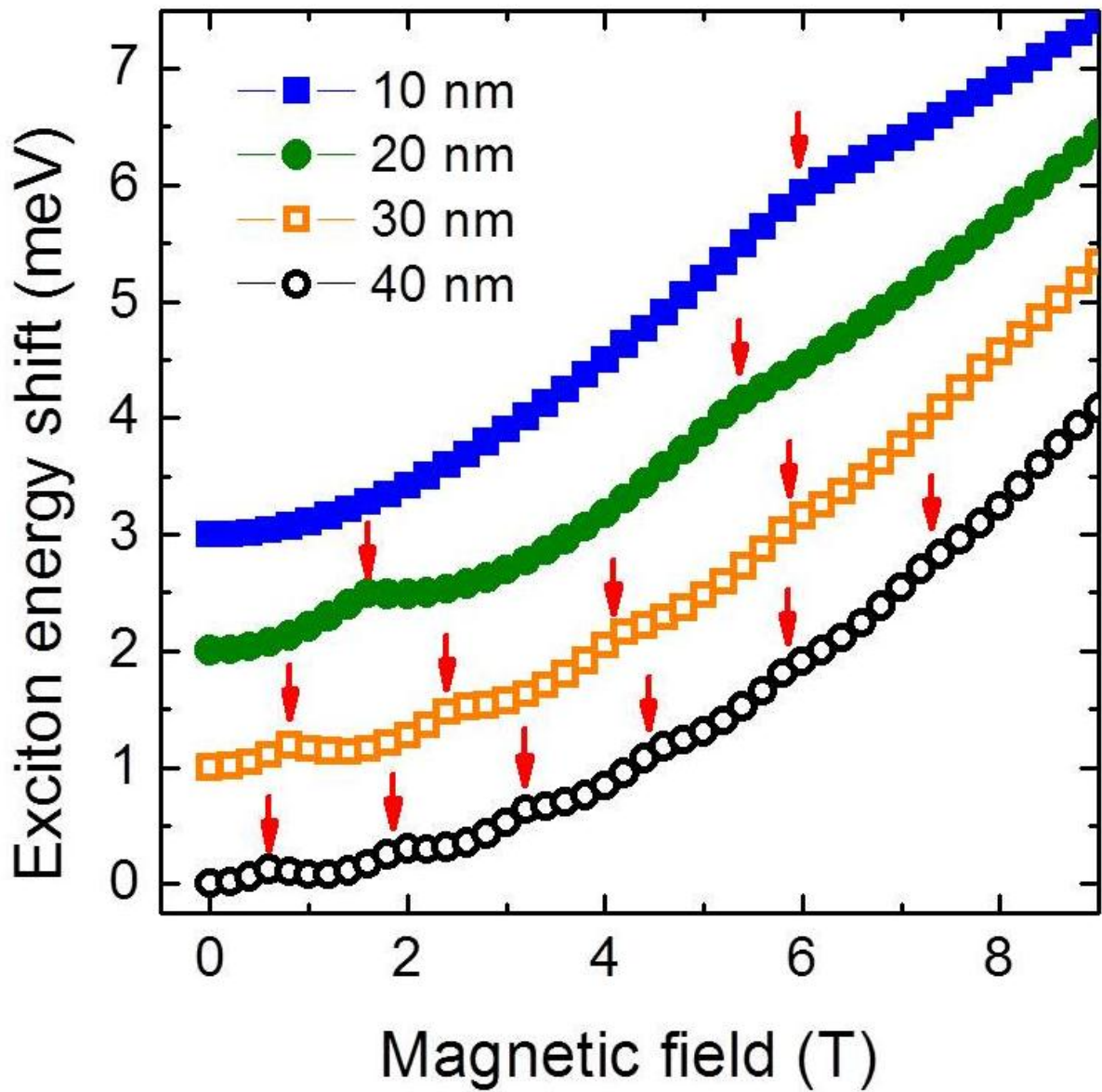
FIG. 6.5. The ground-state exciton energy shifts of the different-sized QDs with the hole occupancy of 1. The arrows indicate the occurrence of the crossing of the energy states with different angular momentum.

6.5 Conclusion

In this chapter, we model and calculate the GaSb/GaAs QDs sandwiched by two AlGaAs confinement layers above and below the dot. The electrons are found to be pushed to surround the dot and hence possess ring-like wave functions. The excitonic AB oscillation is clearly observed in the calculation. Besides, as the base width of the dot gets smaller, the radius of the ring-shaped electron wave function gets smaller. This leads to the larger amplitude and the longer period of the oscillation. In order to increase the oscillation amplitude, smaller quantum dots with the diameter of 20 nm are found to be suitable for the exhibition of the Aharonov-Bohm effect.
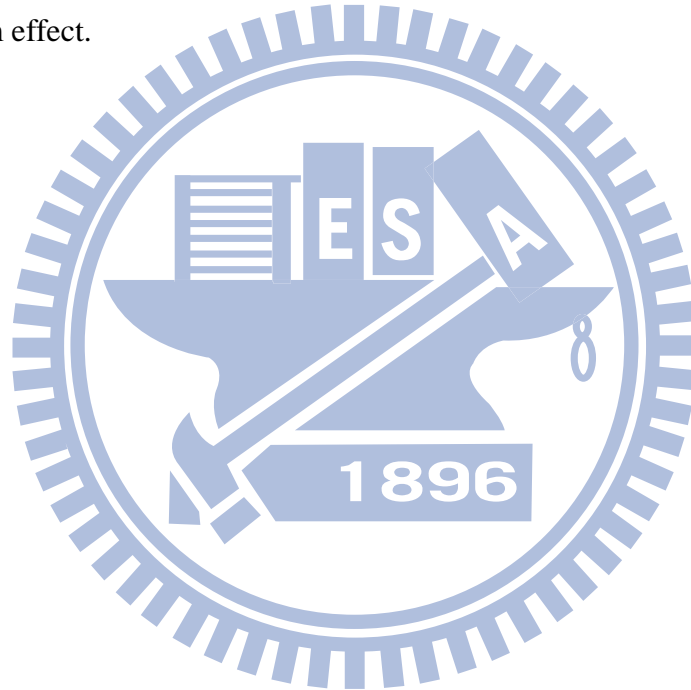
Chapter 7

Conclusions and Future Work

7.1 Conclusions of the Present Studies

The magneto-photoluminescence measurements were performed on type-I InAs/GaAs quantum rings, GaSb/GaAs type-II quantum dots, and GaAs/GaSb type-II quantum dots. These quantum structures were expected to possess ring-like carrier wave functions and exhibit optical Aharonov-Bohm effect. For each system, several unusual magneto-optical responses were observed. Theoretical calculations were carried out and agreed well with these experimental findings. These results provided further understanding of the quantum mechanics on these novel systems. However, we also discovered several unexpected effects destroying the ring-like wave function of them. Therefore, a new structure containing GaSb quantum dots with additional vertical confinement is designed for the exhibition of optical Aharonov-Bohm oscillation.

7.1.1 Geometric Anisotropy of InAs/GaAs Quantum Rings

The exciton confined in single InAs QRs shows a considerably smaller diamagnetic coefficient than the biexciton, indicating the less extended exciton wave functions in the ring. This is attributed to the inherent structural asymmetry of the QRs, which was clearly observed using atomic force spectroscope. The resulting lack of perfect rotational symmetry in the potential of embedded QRs causes the strongly localized excitons in potential valleys of the QRs. As a result, the inherent structural azimuthal asymmetry destroys the expected optical Aharonov-Bohm effect since the quantum interference of the wave function relies on the rotational symmetry of exciton wave functions confined in self-assembled QRs.

7.1.2 Anomalous magnetic red shift of GaSb/GaAs Quantum Dots

When a magnetic field is applied in a Voigt configuration, GaSb QDs exhibit an anomalous magnetic red shift in the PL peak together with a rapid increase of the PL intensity. Based on simulation results, holes are found to be localized inside the QD, and electrons are weakly confined in GaAs regions above and below the QD by Coulomb attraction. The magnetic field in the Voigt configuration is found to provide an additional vertical confinement and push the weakly-bound electrons to the localized holes. The resulting increase of the radiative e-h recombination rate gives rise to the observed anomalous magnetic red shift. Since the electron wave function is distributed above and below the QD, the electron wave function is not ring-like. This eliminates the probability of the observation of the Aharonov-Bohm oscillation.

7.1.3 Delocalization of Tensily-Strained GaAs/GaSb Quantum Dots

As the tensily-strained GaAs QDs get smaller, the diamagnetic coefficient was found to rise quickly from 7.6 μeV/T^2 to a saturated value of around 21 μeV/T^2. In this QD system, electrons are localized in GaAs QDs while holes are confined to the GaSb region next to GaAs by the Coulomb interaction. This unusual behavior is attributed to that the electrons gradually spill out of the quantum dot to the wetting layer as the dots get smaller. This delocalization effect is enhanced in this material system due to the tensile strain relaxation within the dots, which raises the conduction band edge over that in the wetting layer. The lack of the optical Aharonov-Bohm oscillation is attributed to the fact that hole wave function prefer to distributed in the GaSb region above and below the dots.

7.1.4 Aharonov-Bohm Oscillation of GaSb QDs with Vertical Confinement

The simulation results of the magnetic response of type-II GaSb/GaAs quantum dots with AlGaAs vertical confinement layers clearly reveal excitonic Aharonov-Bohm oscillation.

The period and the amplitude of the oscillation are found to have a strong dependence on the dimension of the dots. Smaller quantum dots with the diameter of 20 nm are found to be suitable to exhibit the optical Aharonov-Bohm effect.

7.2 Future Work

7.2.1 Growth of Low-density GaAsSb/GaAs QDs with Additional Vertical Confinement

To exhibit the optical Aharonov-Bohm oscillation, the single dot spectroscopy has to be performed on the GaAsSb QDs with additional vertical confining potential above and below the QDs due to the small amplitude of the oscillation. As a result, the dot density should be well controlled to be $< 1 \times 10^9$ cm^{-2}. However, the spatial separated e-h pairs in type-II structures leads to the low radiative recombination rate. The resulting weak PL emission causes the difficulty of the measurement. The emission wavelength of the GaAsSb/GaAs QDs is about 1200-1300 nm. This range is suitable for InGaAs photodiode array (with detection wavelength range from 750 nm to 1750 nm). However, the signal-to-noise ratio of InGaAs photodiode array is only about 1/10 of that of silicon CCD. In order to obtain excellent signal-to-noise ratio, the silicon CCD (with detection wavelength range from 400 nm to 1000 nm) is chosen to be the photo-detector. Therefore, several growth techniques have to be used to make the emission wavelength of GaAsSb QDs shorter than 1000 nm. For example, the increase of the Al content of the AlGaAs vertical confinement layers and the decrease of the thickness of the GaAs active layer can raise the quantized energy of electrons. The PL emission wavelength can be decreased to 1100 nm. Furthermore, thermal annealing on the QD sample causes the intermixing of Sb and As atoms, which leads to the decrease of the Sb content of the GaAsSb QDs. The resulting increase of the hole energy gives rise to the increased excitonic energy.

To obtain the GaSb QDs with low density, the deposition thickness of GaSb is controlled just over the critical thickness of the QD formation. The critical thickness is determined when

the RHEED pattern turns spotty as mentioned in section 2.1-2. Besides, when the QD layer is grown, the rotation of the sample holder is stopped to generate the gradient of deposition amount. Besides, the growth temperature is ~500 °C, the growth rate of the QD is 0.2 μm/hr, and the V/III beam equivalent pressure (BEP) ratio for QD is 3. The $Al_{0.3}Ga_{0.7}As$ vertical confinement layers are placed above and below the embedded QDs. The thickness of the active GaAs layer is 4 nm. The AFM images of the surface QDs in different positions are plotted in Fig. 7.1. The QDs located in position C have the low enough sheet density of ~7 $x10^8$ cm^{-2}. However, the dot diameter is ~90 nm due to the higher growth temperature in the sample's center. Although the real size of the embedded QDs is always smaller than the surface QDs, the dimension of the embedded QDs is still much larger than 20 nm which is suitable dimension for the observation of AB oscillation. As a result, lower growth temperature of 480 °C will be used in the future for the smaller dot size.

The PL spectra of the QDs in different positions are plotted in Fig. 7.2(a). The emission energy peaks of the QDs range from 1110 nm to 1180 nm. It is found that the QDs in position C have the shortest emission peak of 1110 nm. Since the size of the QDs in position C is the largest one, the short wavelength should be attributed to the higher As content arisen from the severer intermixing between the As and Sb atoms due to the higher growth temperature. However, all these emission peaks are longer than the wavelength limit of silicon CCD of 1000 nm.

In order to shorten the emission wavelength, rapid thermal annealing is treated on the QDs in position C. The annealing is performed for 30 s at 650 ℃, 700 ℃, and 750 ℃. The PL spectra of the as-grown QDs and the QDs after thermal annealing are depicted in Fig. 7.2(b). The emission wavelength of the QDs after annealing at 700 ℃ is shorten to 960 nm due to the atomic intermixing and the resulting higher As content of the dots. Note that the PL emission is significantly weakened for the QDs after annealing at 750 ℃. This represents that the QDs are melted into the GaAs and AlGaAs regions at 750 ℃.
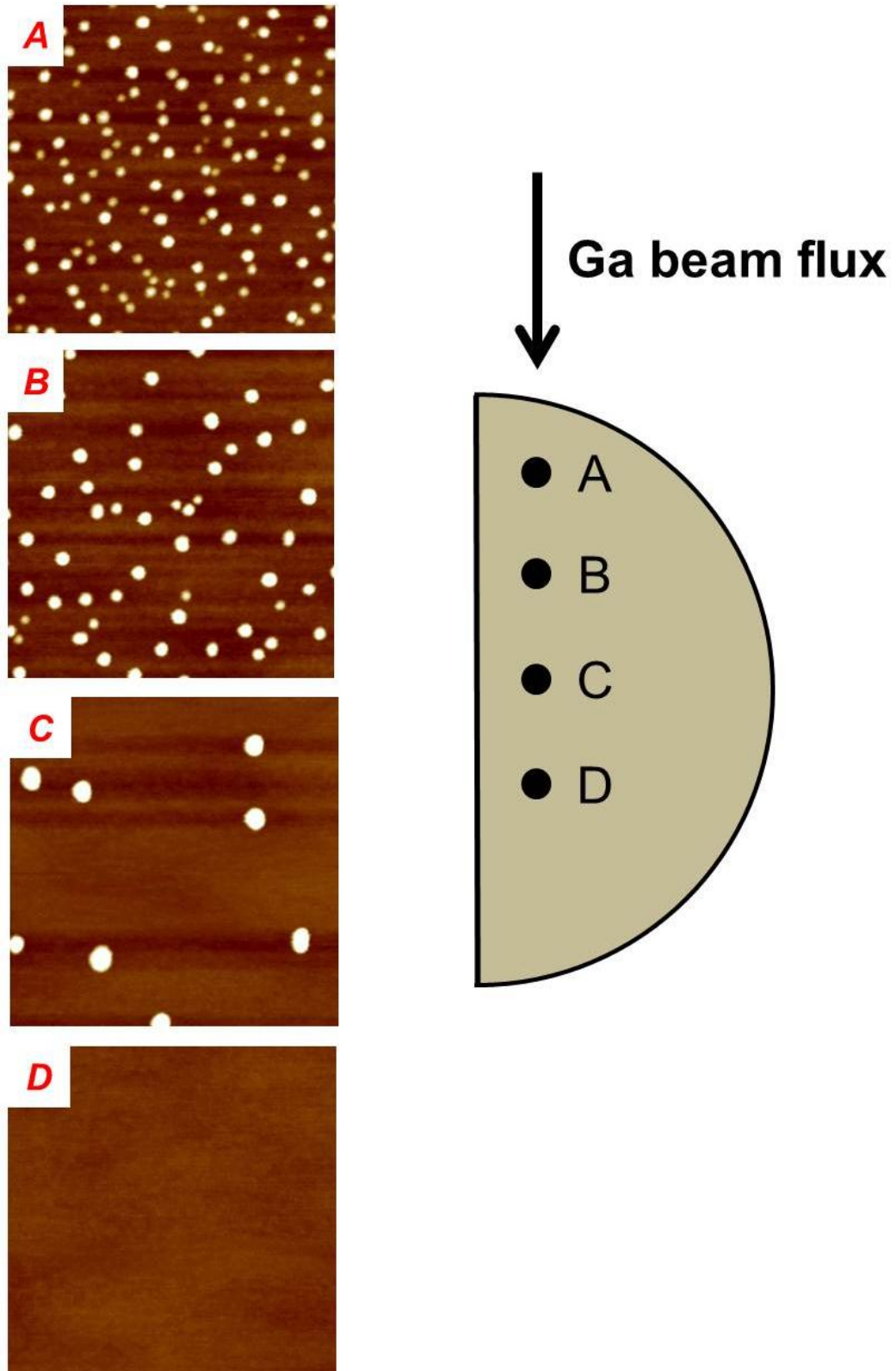
FIG. 7.1. The AFM images of the surface QDs in different positions. The area of each image is 1 μm^2. The diameters of the QDs are ~50 nm, 70 nm, and 90 nm for position A, B, and C, respectively.
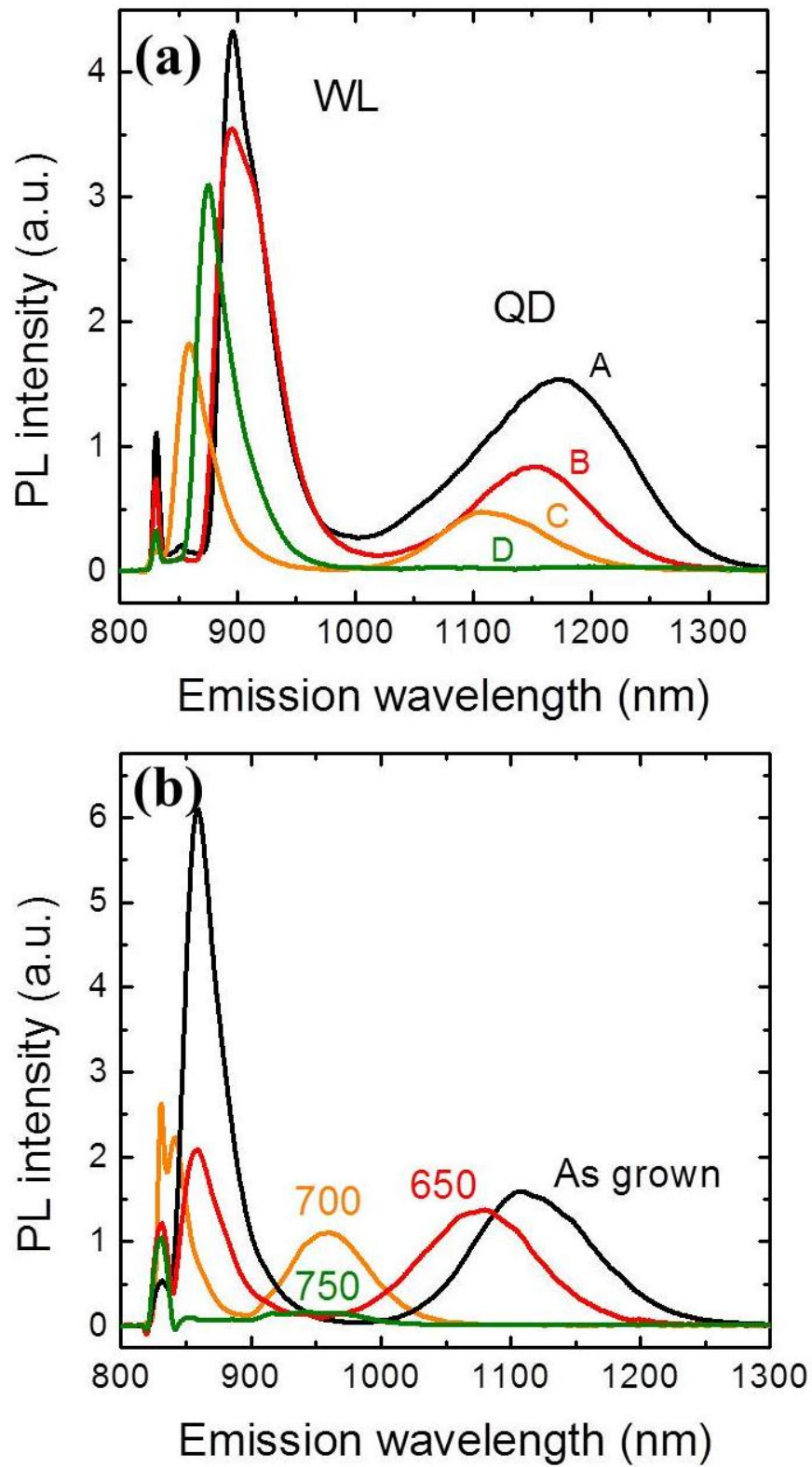
FIG. 7.2. (a) The PL spectra of the QDs in different positions. (b) The PL spectra of the as-grown QDs and the QDs after thermal annealing. The annealing temperature is 650 ℃, 700 ℃, and 750℃.

7.2.2 Single Dot Spectroscope Setup

In order to measure the PL emission from a single dot in the magnetic field applied up to 14 Tesla, a low-temperature high-magnetic-field single dot spectroscope setup is built up as illustrated in Fig. 7.3. The whole stage and the low-temperature objective are made of titanium to eliminate the thermal budget and the magnetic-field-induced vibration. The spot size was estimated to be < 1.5 μm. The sample mounted on the piezoelectric stage can be coarsely moved by ±2 mm and finely scaned by ±20 μm. The system is still under optimization.
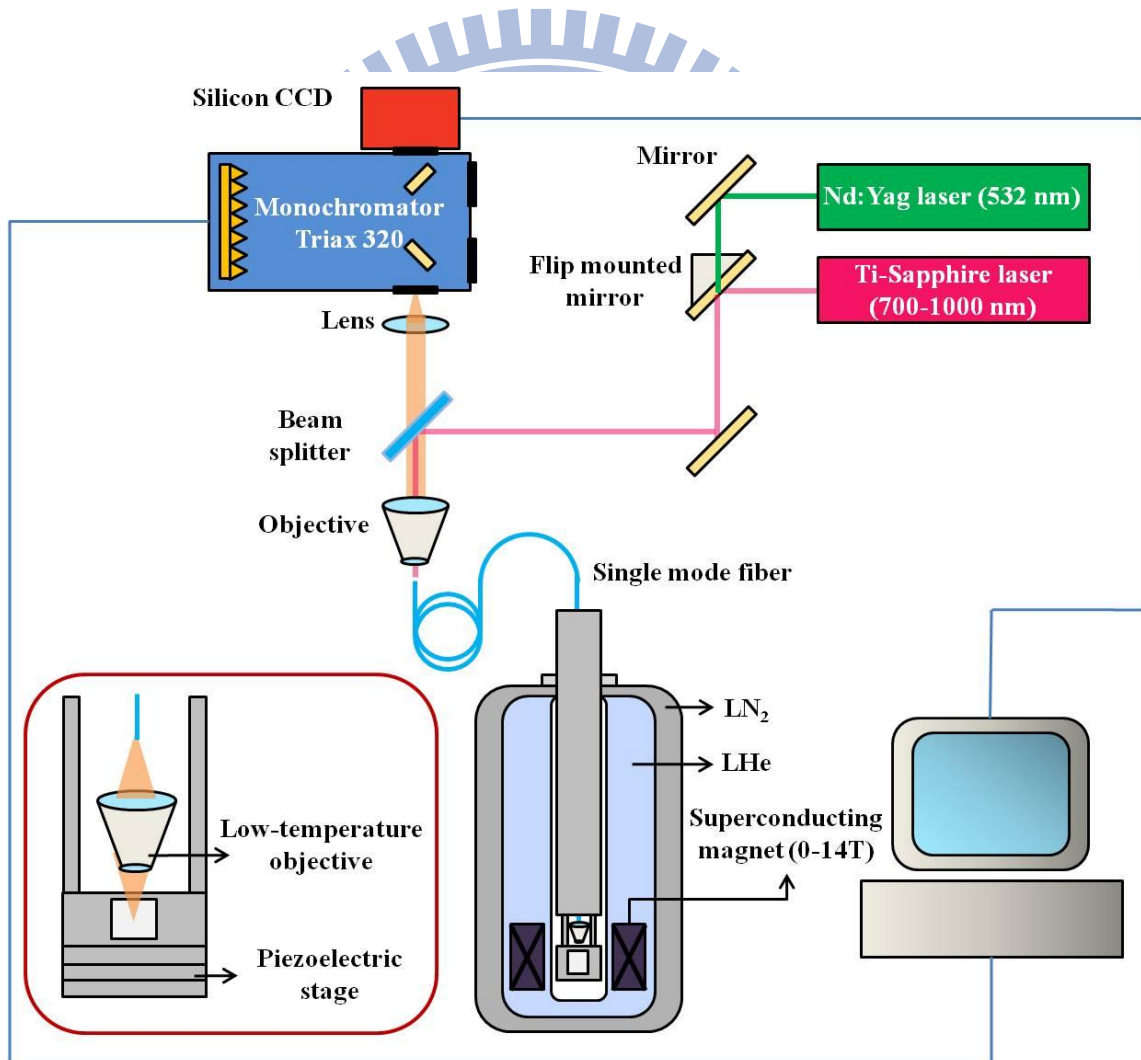
Fig. 7.3 The setup of the low-temperature high-magnetic-field single dot optical spectroscope.

Reference

[1] D. Dragoman, M. Dragoman, Advanced optoelectronic devices, Springer, New York (1999).

[2] L. D. Nguyen, L. E. Larson, and U. K. Mishra, Proc. IEEE, **80**, 494 (1992)

[3] P. Michler, A. Kiraz, C. Becher, W. V. Schoenfeld, P. M. Petroff, Lidong Zhang, E. Hu1, and A. Imamoglu, Science **290**, 2282 (2000)

[4] M. Pelton , C. Santori, J. Vucˇkovic´, B. Zhang, G. S. Solomon,J. Plant, and Y. Yamamoto, Phys. Rev. Lett. **89**, 233602 (2002)

[5] Xiaoqin Li, Yanwen Wu, Duncan Steel, D. Gammon, T. H. Stievater, D. S. Katzer, D. Park, C. Piermarocchi, L. J. Sham , Science **301**, 809 (2003).

[6] F. Ding, N. Akopian, B. Li, U. Perinetti, A. Govorov, F. M. Peeters, C. C. Bof Bufon, C. Deneke, Y. H. Chen, A. Rastelli, O. G. Schmidt, and V. Zwiller, Phys. Rev. B **82**, 075309 (2010)

[7] E. Ribeiro, A. O. Govorov, W. Carvalho, Jr, and G. Medeiros- Ribeiro, Phys. Rev. Lett. **92**, 126402 (2004).

[8] I. R. Sellers, V. R. Whiteside, I. L. Kuskovsky, A. O. Govorov, and B. D. McCombe, Phys. Rev. Lett. **100**, 136405 (2008).

[9] M. D. Teodoro, V. L. Campo, Jr., V. Lopez-Richard, E. Marega, Jr., G. E. Marques, Y. Galva˜o Gobato, F. Iikawa, M. J. S. P. Brasil, Z.Y. AbuWaar, V. G. Dorogan, Yu. I. Mazur, M. Benamara, and G. J. Salamo, Phys. Rev. Lett. **104**, 086401 (2010).

[10] K. Kash, A. Scherer, J. M. Worlock, et al., Appl. Phys. Lett., **49,** 1043 (1986).

[11] K. Kash, R. Bhat, D. D. Mahoney, P. S. D. Lin, A. Scherer, J. M. Worlock, B. P. Van der Gaag, M. Koza, and P. Grabbe, Appl. Phys. Lett. **55**, 681 (1989).

[12] W. Seifert, N. Carlsson, M. Miller, et al., Prog. Crystal Growth and Charact., **33,** 423 (1996)

[13] H. S. Ling, and C. P. Lee, J. Appl. Phys. **102**, 024314 (2007)

[14] B.C. Lee, O. Voskoboynikov, and C.P. Lee, physica E **24**, 87 (2004)

[15] M. D. Teodoro, V. L. Campo, Jr., V. Lopez-Richard, E. Marega, Jr., G. E. Marques, Y. Galva˜o Gobato, F. Iikawa, M. J. S. P. Brasil, Z.Y. AbuWaar, V. G. Dorogan, Yu. I. Mazur, M. Benamara, and G. J. Salamo, Phys. Rev. Lett. **104**, 086401 (2010).

[16] I. Vurgaftman, J. R. Meyer, and L. R. Ram-Mohan, J. Appl. Phys. **89**, 5815 (2001)

[17] C. E. Pryor, and M. E. Pistol, Phys. Rev. B **72**, 205311 (2005)

[18] M. Geller, C. Kapteyn, L. Mu¨ller-Kirsch, R. Heitz, and D. Bimberg, Appl. Phys. Lett. **82**, 2706 (2003).

[19] H. Gotoh, H. Ando, H. Kamada, A. Chavez-Pirson, and J. Temmyo, Appl. Phys. Lett. **72**, 1341 (1998).

[20] Shih-Yen Lin, Chi-Che Tseng, Wei-Hsun Lin, Shu-Cheng Mai, Shung-Yi Wu, Shu-Han Chen, and Jen-Inn Chyi1, Appl. Phys. Lett. **96**, 123503 (2010).

[21] K. L. Janssens, B. Partoens, and F. M. Peeters, Phys. Rev. B **66**, 075314 (2002)

[22] R. Rinaldi, P. V. Giugno, R. Cingolani, H. Lipsanen, M. Sopanen, J. Tulkki, and J. Ahopelto, Phys. Rev. Lett. **77**, 342 (1996)

[23] L. P. Le´vy, G. Dolan, J. Dunsmuir, and H. Bouchiat, Phys. Rev. Lett. **64**, 2074 (1990).

[24] V. Chandrasekhar, R. A. Webb, M. J. Brady, M.B. Ketchen, W. J. Gallagher, and A. Kleinsasser, Phys. Rev. Lett. **67**, 3578 (1991).

[25] D. Mailly, C. Chapelier, and A. Benoit, Phys. Rev. Lett. **70**, 2020 (1993).

[26] A. Fuhrer, S. Luscher, T. Ihn, T. Heinzel, K. Ensslin, W. Wegscheider, and M. Bichler, Nature (London) **413**, 822 (2001)

[27] A. Lorke, R. J. Luyken, A. O. Govorov, J. P. Kotthaus, J. M. García, and P. M. Petroff, Phys. Rev. Lett. **84**, 2223 (2000).

[28] M. Bayer, M. Korkusinski, P. Hawrylak, T. Gutbrod, M. Michel, and A. Forchel, Phys. Rev. Lett. **90**, 186801 (2003).

[29] N. A. J. M. Kleemans, I. M. A. Bominaar-Silkens, V. M. Fomin, V. N. Gladilin, D. Granados, A. G. Taboada, J. M. García, P. Offermans, U. Zeitler, P. C. M. Christianen, J. C. Maan, J. T. Devreese, and P. M. Koenraad, Phys. Rev. Lett. **99**, 146808 (2007).

[30] A. O. Govorov, S. E. Ulloa, K. Karrai, and R. J. Warburton, Phys. Rev. B. **66**, 081309(R) (2002).

[31] D. Granados and J. M. García, Appl. Phys. Lett. **82**, 2401 (2003).

[32] P. Offermans, P. M. Koenraad, J. H. Wolter D. Granados, J. M. García, V. M. Fomin, V. N. Gladilin, and J. T. Devreese, Appl. Phys. Lett. **87**, 131902 (2005).

[33] R. J. Young, R. M. Stevenson, A. J. Shields, P. Atkinson, K. Cooper, D. A. Ritchie, K. M. Groom, A. I. Tartakovskii, and M. S. Skolnick, Phys. Rev. B. **72**, 113305 (2005).

[34] M. F. Tsai, H. Lin, C. H. Lin, S. D. Lin, S. Y. Wang, M. C. Lo, S. J. Cheng, M. C. Lee, and W. H. Chang, Phys. Rev. Lett. **101**, 267402 (2008).

[35] M. Bayer, G. Ortner, O. Stern, A. Kuther, A. A. Gorbunov, A. Forchel, P. Hawrylak, S. Fafard, K. Hinzer, T. L. Reinecke, S. N. Walck, J. P. Reithmaier, F. Klopf, and F. Scha¨fer, Phys. Rev. B. **65**, 195315 (2002)

[36] D. J. P. Ellis, R. M. Stevenson, R. J. Young, A. J. Shields, P. Atkinson, and D. A. Ritchie, Appl. Phys. Lett. **90**, 011907 (2007)

[37] A. Kuther, M. Bayer, A. Forchel, A. Gorbunov, V. B. Timofeev, F. Schäfer, and J. P. Reithmaier, Phys. Rev. B. **58**, R7508 (1998).

[38] A. Babinski, S. Awirothananon, J. Lapointe, Z. Wasilewski, S. Raymond, and M. Potemski, Physica E **26**, 190 (2005).

[39] V. M. Fomin, V. N. Gladilin, S. N. Klimin, J. T. Devreese, N. A. J. M. Kleemans, and P. M. Koenraad, Phys. Rev. B. **76**, 235320 (2007).

[40] M. Hayne, J. Maes, S. Bersier, V. V. Moshchalkov, A. Schliwa, L. Mu¨ller-Kirsch, C. Kapteyn, R. Heitz, and D. Bimberg, Appl. Phys. Lett. **82**, 4355 (2003).

[41] M. Hayne, O. Razinkova, S. Bersier R. Heitz, L. Müller-Kirsch, M. Geller, D. Bimberg,

and V. V. Moshchalkov, Phys. Rev. B **70**, 081302(R) (2004)

[42] Bhavtosh Bansal, M. Hayne, M. Geller, D. Bimberg, and V. V. Moshchalkov, Phys. Rev. B **77**, 241304(R) (2008)

[43] Tomohiko Sato, Toshihiko Nakaoka, Makoto Kudo, Yasuhiko Arakawa, Physica E **32**, 152 (2006)

[44] M. Ahmad Kamarudin, M. Hayne1, R. J. Young, Q. D. Zhuang, T. Ben, and S. I. Molina, Phys. Rev. B **83**, 115311 (2011).

[45] Ming-Cheng Lo, Shyh-Jer Huang, Chien-Ping Lee, Sheng-Di Lin, and Shun-Tung Yen, Appl. Phys. Lett. **90**, 243102 (2007).

[46] L. Müller-Kirsch, R. Heitz, U. W. Pohl, D. Bimberg, I. Häusler, H. Kirmse, and W. Neumann, Appl. Phys. Lett. **79**, 1027 (2001).

[47] N. N. Ledentsov, J. Böhrer, M. Beer, F. Heinrichsdorff, M. Grundmann, D. Bimberg, S. V. Ivanov, B. Ya. Meltser, S. V. Shaposhnikov, I. N. Yassievich, N. N. Faleev, P. S. Kop'ev, and Zh. I. Alferov, Phys. Rev. B **52**, 14058 (1995).

[48] L. Müller-Kirsch, R. Heitz, A. Schliwa, D. Bimberg, H. Kirmse, and W. Neumann, Appl. Phys. Lett. **78**, 1418 (2001).

[49] O. Stier, M. Grundmann, and D. Bimberg, Phys. Rev. B **59**, 5688 (1999).

[50] R. Timm, H. Eisele, A. Lenz, S. K. Becker, J. Grabowski, T.-Y. Kim, L. Müller-Kirsch, K. Pötschke, U. W. Pohl, D. Bimberg, and M. Dähne, Appl. Phys. Lett. **85**, 5890 (2004).

[51] A. A. Toropov, O. G. Lyublinskaya, B. Ya. Meltser, V. A. Solov'ev, A. A. Sitnikova, M. O. Nestoklon, O. V. Rykhova, S. V. Ivanov, K. Thonke and R. Sauer,

Phys. Rev. B **70**, 205314 (2004)

[52] S. H. Huang, G. Balakrishnan, M. Mehta, L. R. Dawson, and D. L. Huffaker, P. Li, J. Appl. Phys. **102**, 044312 (2007)

[53] H. Saito, K. Nishi, and S. Sugou, Appl. Phys. Lett. **74**, 1224 (1999).

[54] F. Hatami, N. N. Ledentsov, M. Grundmann, J. Böhrer, F. Heinrichsdorff, M. Beer, D.

Bimberg, S. S. Ruvimov, P. Werner, U. Gösele, J. Heydenreich, U. Richter, S. V. Ivanov, B. Ya. Meltser, P. S. Kop'ev, and Zh. I. Alferov, Appl. Phys. Lett. **67**, 656 (1995).

[55] M. Dinu, J. E. Cunningham, F. Quochi, and J. Shah, J. Appl. Phys. **94**, 1506 (2003)

[56] M. C. Lo, S. J. Huang, C. P. Lee, S. D. Lin, and S. T. Yen, Appl. Phys. Lett. **90**, 243102 (2007).

[57] Y.-H. Cho, T. J. Schmidt, S. Bidnyk, G. H. Gainer, J. J. Song, S. Keller, U. K. Mishra, and S. P. DenBaars, Phys. Rev. B **61**, 7571 (2000).

[58] J. Bai, T. Wang, and S. Sakai, J. Appl. Phys. **88**, 4729 (2000).

[59] F. Ishikawa, Á. Guzmán, O. Brandt, A. Trampert, and K. H. Ploog, J. Appl. Phys. **104**, 113502 (2008).

[60] A. Aı̈t-Ouali, R. Y.-F. Yip, J. L. Brebner, and R. A. Masut, J. Appl. Phys. **83**, 3153 (1998).

[61] W. H. Chang, Y. A. Liao, W. T. Hsu, M. C. Lee, P. C. Chiu, and J. I. Chyi, Appl. Phys. Lett. **93**, 033107 (2008).

[62] M. Sugisaki, H. W. Ren, S. V. Nair, K. Nishi, and Y. Masumoto, Phys. Rev. B **66**, 235309 (2002).

[63] S. N. Walck and T. L. Reinecke, Phys. Rev. B **57**, 9088 (1998)

[64] D. F. Nelson, R. C. Miller, and A. A. Kleinman, Phys. Rev. B **35**, 7770 (1987)

[65] M. Grochol, F. Grosse, and R. Zimmermann, Phys. Rev. B **74**, 115416 (2006).

Vita

Name : Ta-Chun Lin (林大鈞)

Date of birth :　February 10, 1982

Place of birth : Taichung, Taiwan, ROC

Sex : Male

Education :

Nation Chiao Tung University　　　Ph. D.　　September, 2005－August, 2011

Department of Electronics Engineering & Institute of Electronics

Nation Chiao Tung University　　　M. S.　　September, 2004－June, 2005

Department of Electronics Engineering & Institute of Electronics

Nation Chiao Tung University　　　B. S.　　September, 2000－June, 2004

Department of Materials Science and Engineering

Title of Ph. D. Dissertation :

Magneto-optical Studies of Self-assembled Type-I Quantum Rings and Type-II Quantum Dots.

Publication List

[1] **T. C. Lin**, C. H. Lin, H. S. Ling, Y. J. Fu, W. H. Chang, S. D. Lin, and C. P. Lee, "Impacts of structural asymmetry on the magnetic response of excitons and biexcitons in single self-assembled In(Ga)As quantum rings" Phys. Rev. B **80**, 081304(R) (2009)

[2] **T. C. Lin**, Y. H. Wu, L. C. Li, Y. T. Sung, S. D. Lin, L. Chang, Y. W. Suen, C. P. Lee, "Electron Delocalization of Tensily-Strained GaAs Quantum Dots in GaSb matrix" J. Appl. Phys. **108**, 123503 (2010)

[3] **Ta-Chun Lin**, Liang-Chen Li, Sheng-Di Lin, Yuen-Wuu Suen, and Chien-Ping Lee, "Anomalous optical magnetic shift of self-assembled GaSb/GaAs quantum dots" accepted for the publication in J. Appl. Phys on Jun. 09, 2011.

[4] **T. C. Lin**, H. S. Ling, S. D. Lin, C. P. Lee, C. H. Lin, and W. H. Chang, "Magneto-optical study of single InAs/GaAs quantum rings" Trends in Nanotechnology 2009 International Conference, Barcelona, Spain (Sept. 07-11, 2009)

[5] **T. C. Lin**, S. D. Lin, and C. P. Lee, "Magneto-Optical Studies of GaAs Quantum Dots in GaSb" 16th international conference in molecular beam epitaxy 2010, Berlin, German (Aug. 22-27, 2010)

[6] **T. C. Lin**, L. C. Li, C. Cheng, Y. T. Sung, S. D. Lin, Y. W. Suen, and C. P. Lee, "Anomalous optical magnetic shift of self-assembled GaSb/GaAs quantum dots" 19th

international conference on Electronic Properties of Two-Dimensional Systems (EP2DS19), Tallahassee, Florida, USA (Jul. 25-29, 2011)

[7] T. L. Shao, S. W. Liang, **T. C. Lin**, and C. Chen, "Three-dimensional simulation on current-density distribution in flip-chip solder joints under electric current stressing" J. Appl. Phys. **98**, 044509 (2005)

[8] K. Y. Wang, W. P. Huang, **T. C. Lin**, C. P. Lee, Y. T. Sung, R. J. Nicholas, and H. H. Cheng, "Type-I/type-II exciton in strained Si/SiGe multi-QWs" Physica E **40**, 1430 (2008)

[9] W. H. Chang, C. H. Lin, Y. J. Fu, **T. C. Lin**, H. Lin, S. J. Cheng, S. D. Lin, and C. P. Lee, "Impacts of Coulomb Interactions on the Magnetic Responses of Excitonic Complexes in Single Semiconductor Nanostructures" Nanoscale Res. Lett. **5**, 680 (2010)

[10] L. M. Thu, W. T. Chiu, **Ta-Chun Lin**, and O. Voskoboynikov, "Effect of geometry on the excitonic diamagnetic shift of nano-rings" Phys. Status Solidi C **8**, No. 2, 375–377 (2011)